PERFORMANCE ANALYSIS OF WIND TURBINES WITH TIP VANES

NAFIZ AHMED KHAN

(*B.Sc. Engg., MIST*)

A THESIS SUBMITTED FOR THE DEGREE OF

MASTER OF SCIENCE IN MECHANICAL ENGINEERING

DEPARTMENT OF MECHANICAL ENGINEERING

MILITARY INSTITUTE OF SCIENCE AND TECHNOLOGY

2021

APPROVAL OF BOARD OF EXAMINERS

The thesis titled "**PERFORMANCE ANALYSIS OF WIND TURBINES WITH TIP VANES**" submitted by **Nafiz Ahmed Khan;** Roll No: **0418180003 (P);** Session: 2017-18 has been accepted as satisfactory in partial fulfillment of the requirement for the degree of Master of Science in Mechanical Engineering.

BOARD OF EXAMINERS

1. ………………………………………..   **Chairman**
   Professor Dr. Md Quamrul Islam   **(Supervisor)**
   Department of Mechanical Engineering
   MIST, Dhaka- 1216, Bangladesh

2. ………………………………………….   **Member**
   Brig Gen Md Humayun Kabir Bhuiyan   **(Ex- Officio)**
   Head, Department of Mechanical Engineering
   MIST, Dhaka- 1216, Bangladesh

3. …………………………………………   **Member**
   Professor Dr. M A Taher Ali   **(Internal)**
   Department of Aeronautical Engineering
   MIST, Dhaka- 1216, Bangladesh

4. …………………………………………   **Member**
   Assistant Professor Dr. Muammer Din Arif   **(Internal)**
   Department of Mechanical Engineering
   MIST, Dhaka- 1216, Bangladesh

5. …………………………………………   **Member**
   Professor Dr. Mohammad Ali   **(External)**
   Department of Mechanical Engineering
   BUET, Dhaka- 1000, Bangladesh

DECLARATION

I do hereby declare that this thesis is my original work and I have written it in its entirety.

I have duly acknowledged all the sources of information which have been used in the

thesis. This thesis has not also been submitted for any degree in any university previously.

……………………………

Nafiz Ahmed Khan

Department of Mechanical Engineering

Military Institute of Science and Technology (MIST)

July 2021

SUMMARY

Performance enhancement of horizontal axis wind turbine (HAWT) with circular arc blade section (CABS) has been investigated both experimentally and computationally using upstream and downstream tip-vanes (winglet) configurations. A computational study is performed for a three-blade rotor of 0.5m diameter in ANSYS Fluent to identify the optimum values for cant angle and twist angle. Findings from the numerical analysis are then utilized as inputs for the experimental study. The height of the winglet is selected as 6% of the rotor radius while cant angle and twist angle are 55° and 0°, respectively. Power and thrust coefficient are measured for both the upstream and downstream winglet orientations at different pitch angles (ϕ) and tip speed ratios (λ). Results show that thrust coefficient increases with the increase of tip speed ratio. There is an around 10.94% and 8.56% increment for upstream and downstream winglets, respectively, in terms of without winglets at design tip speed ratio (TSR=5) and zero pitch angle. Regarding power coefficient, the upstream winglet provides 9.79 % extra power in comparison with the reference model at design tip speed ratio and zero pitch angle. Improved performance is obtained with downstream winglet achieving almost 15% additional power at zero pitch angle. But with the increase of the pitch angles, power decreases as $\lambda^{0.1}$. The reason for extracting more wind energy by downstream winglets can be explained from the pressure coefficient values. Near the leading edge, r/R=95%, of the blade, the pressure difference between suction and pressure surface is 15 for the downstream winglets, and 6 is in the case of without winglets.

Keywords: Wind turbine rotor, CABS, Winglets, Power coefficient, Thrust coefficient

ACKNOWLEDGEMENTS

TABLE OF CONTENTS

LIST OF SYMBOLS

V_∞	Undisturbed wind velocity far from the upstream, m/s
V	Axial Wind velocity when it flows through the rotor, m/s
V_2	Axial Wind velocity far behind the rotor, m/s
A	Turbine disk area, m^2
ρ	Air density, kg/m^3
p+	Pressure immediately in front of the rotor (Pa)
V_∞	Undisturbed wind velocity far from the upstream, m/s
V	Axial Wind velocity when it flows through the rotor, m/s
V_∞	Undisturbed wind velocity far from the upstream, m/s
V	Axial Wind velocity when it flows through the rotor, m/s
V_2	Axial Wind velocity far behind the rotor, m/s
A	Turbine disk area, m^2
p+	Pressure immediately in front of the rotor (Pa)
p$^-$	Pressure immediately behind the rotor (Pa)
V_t	Wake tangential velocity (m/s)
u, v, w	Components of the velocity in the x, y, and z directions respectively
p	Pressure
τ_{ij}	Normal land shear stresses that affect the 3D fluid particles
S_{Mx}, S_{My}, S_{Mz}	Body forces per unit of mass in the x, y, and z directions respectively.
T	Temperature
ϕ_P	Pitch angle
P	Power generated in Watts
T	Torque generated per blade in N.m

Ω	Angular velocity of rotor in radians/seconds
ω	Angular velocity of wake in radians/seconds
R	Rotor radius in mm
r	Section radius in the turbine blade in mm
λ	Tip speed ratio
λ_r	Local tip speed ratio
B	Number of blades of the wind turbine.
G_k	Turbulence kinetic energy due to the mean velocity gradients
G_b	Generation of turbulence kinetic energy due to buoyancy
Y_M	Contribution of the fluctuating dilatation in compressible turbulence to the overall dissipation rate,
$C_2, C_{1\varepsilon}$	Constants
$\sigma_k, \sigma_\varepsilon$	Turbulent Prandtl numbers for k and ε respectively.
S_k, S_ε	User-defined source terms
C_{50}	Chord of the ideal blade at r/R = 0.5
C_{90}	Chord of the ideal blade at r/R = 0.9
β_{50}	Twist of the ideal blade at r/R = 0.5
β_{90}	Twist of the ideal blade at r/R = 0.9
ΔC_{pr}	Change in pressure coefficient between pressure and suction side

Abbreviations

HAWT	Horizontal Axis Wind Turbine
CABS	Circular Arc Blade Section
3D	Three Dimensional
CFD	Computational Fluid Dynamics

LIST OF FIGURES

LIST OF TABLES

CHAPTER 1

INTRODUCTION

1.1 General

With the increase of population growth and industrial evolution, uses of energy have enhanced. However most of the energy is induced from some conventional energy sources like coal, crude oil or natural gases. These fossil fuels emit an enormous amount of carbon dioxide (CO_2), increasing global warming. As a result, our atmosphere is contaminated with different poisonous particles. Also it is a matter of fact, that contaminated air is very injurious to health as well as a threat to humankind. Based on these issues, people are rethinking and moving their concern to the use of renewable energy resources like wind, solar, hydro energies.

Wind forces can be an excellent medium for extracting energy and converting it to electricity due to its availability. There has been a noticeable development in extracting energy from the wind by using wind turbines. Nowadays, people are using both horizontal axis and vertical axis wind turbines for the generation of electricity from wind. Considerable study and research have already been done on the increment of efficiency of Horizontal and Vertical axis wind turbines. The primary focus of this present study is a horizontal axis wind turbine (HAWT) and how the performance of this HAWT can be enhanced. For the conventional HAWT blade profile NACA (National Advisory Committee for Aeronautics), airfoils are customarily used. However, due to the complexity of fabrication, simplified type wind turbine blades are chosen. Despite being the more straightforward type of wind turbines, they provide adequate power generation at low tip speed ratio (less than 6). A HAWT with a circular arc blade section (CABS) has been chosen for analyzing the performance of wind turbines. Additionally, tip-vanes (winglets)

are also added to both upstream and downstream sides to evaluate the performance of the turbine blades, as they tend to decrease the formation of vortices at the blade tip.

1.2 Wind Turbine Components

Nowadays, Horizontal Axis Wind Turbine (HAWT), which is one of the types of wind turbines, is the most common to use for harnessing energy due to its axis of rotation is always kept parallel to the ground. The primary components of a HAWT as shown in Fig. (1.1) below, includes:

- ❏ The rotor: blades and hub
- ❏ Drive train: including shafts, gearbox, brake system and generator
- ❏ Nacelle: housing and yaw system
- ❏ Tower and foundation
- ❏ Electrical and control system
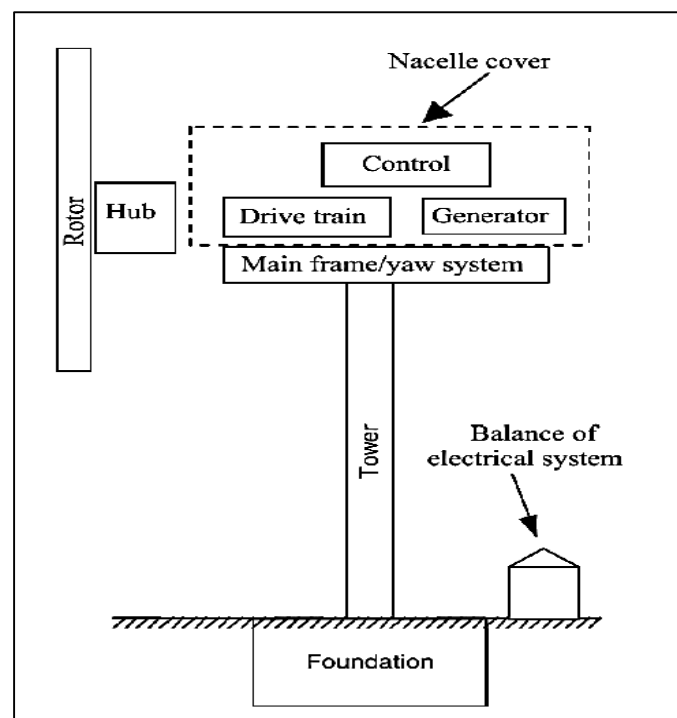
Fig. 1.1 Primary Components of a HAWT [1]

1.3 Objectives of the Thesis

Many research activities are going on how wind turbines can be used to extract more wind energy. Though conventional NACA airfoils are used in those wind machines, there is still less attention on the application of CABS (Circular arc blade section). From the literature review, it is perceived that CABS provides an acceptable amount of power generation concerning NACA airfoils in the low-speed region. For this purpose, the CABS profile used in this present thesis work instead of NACA airfoils.

Much research has already been done on the increment of efficiency of Horizontal and Vertical axis wind machines. But adding tip vanes at the tip of wind turbines to overcome the downwash effect is still a less focused zone. For this motive, a theoretical and experimental investigation of the influence of elliptical tip-vanes on the HAWT are considered for the present study, which includes the following:

a) To design and develop a small scale wind turbine and experimental set up for continuous assessment of wind turbine.

b) To observe the performance (Power coefficient and Thrust coefficient) of horizontal axis wind turbine with a circular arc blade profile.

c) To design tip-vanes (winglets) for a particular CANT angle, the radius of curvature and tip-vane height and analyze the performance of incorporating tip-vanes at the HAWT blades by overcoming the tip-loses effect.

d) To compare the experimental results of the wind turbine having a circular arc blade section with and without the tip-vanes.

e) To take into consideration the effect of the position of tip-vanes by incorporating the tip-vanes at upstream and downstream sides.

f) To perform the design analysis of HAWT with and without the tip-vanes for the proper use of wind turbines are having a lower wind speed area.

1.4 Scope of the Thesis

The scope of this thesis is to analyze the performance of wind turbines by adding winglets at the tip. Before the analysis, a wind turbine model has designed as well as winglets. Moreover, winglets are attached both in the upstream and downstream sides of the blades to predict their effectiveness.

1.5 Structure of the Thesis

A brief discussion has done for investigating the performance of Horizontal axis wind Turbines having circular arc blade section with and without the tip-vanes is provided in this section:

In **Chapter One,** the prominence of this research work and how renewable energy becomes one of the prominent resources for harnessing clean energy is discussed. Some general ideas of the present study, including the objectives of the thesis, are also mentioned.

In **Chapter Two,** the literature review and background of wind power are described. The development of wind power from the ancient period to the modern age is mentioned. The publications correlated with this present study, and references are also included.

In **Chapter Three,** the conventional theories, like momentum theory and the blade element theory, together with cascade theory, are described. The theories that are correlated with this present work are taken into consideration. The effect of tip losses on the wind turbine blade profiles is also mentioned.

In **Chapter Four,** a detailed computational methodology and grid-cell independency test have been discussed.

In **Chapter Five,** a detailed illustration of the methodology and experimental procedure of the study is addressed. The design and fabrication of turbine blades, tip-vanes

with different parameters, turbine rotor, selection of tip speed ratio, number of blades, steps for the calculation of blade configuration, calculations of blade chord, blade twist angle and choice of blade and tip-vanes materials have been presented.

In **Chapter Six,** the description of experimental setup and experimental procedures have been discussed.

In **Chapter Seven,** the relative contributions to the field of study are given. The performance prediction of HAWT with and without tip-vanes is discussed. The effect of tip losses and the reduction of tip vortices are analyzed. Furthermore, the impact of incorporating the tip-vanes in upstream and downstream positions is also mentioned.

In **Chapter Eight,** the conclusion of the present study, findings, its limitations, along with the recommendation for future work, have been included.

CHAPTER 2

LITERATURE REVIEW

2.1 General

Constructively using renewable energy sources has become one of the significant challenges in the 21st century. Wind energy is the most common and useful form of renewable energy. Moreover, it isn't affected by weather or climate like solar energy. According to the Global Wind Energy Council, new installations capacity of wind turbines both for onshore and offshore is 60.4GW annually until 2023[2]. Since the early days, people have been using wind power to sail the ships and navigate them from one place to another. Afterward, wind energy used to run the wind pumps and windmills for specific periods of the year. Then those had been replaced by the electrical motor and steam engines.

Over time, people are facing an energy crisis along with environmental degradation problems. For that reason people are now thinking about clean energy. Numerous research is going on to harness the power at a low cost and environment-friendly way. Keeping that in mind, wind machines developed to extract clean energy from the wind. The wind has also been utilized in windmills for grinding grain or for pumping water. Researchers have followed the working process of windmills and then turned out the wind turbines. Wind turbines are also named 'wind machines' because of converting the kinetic energy of the wind to mechanical energy for utilizing electrical power. Depending on the capacity, wind turbines can be divided into two divisions, like small capacity and large capacity wind turbines. Large capacity turbines require large amounts of torque, and thus an additional generator is used as a motor to start, accelerate the motor. But in the case of small capacity turbines, wind hitting on the blade produces a torque that is used for power generation. The small capacity wind is commercially made for its affordability, reliability, and reasonable

maintenance cost. So, the small capacity Horizontal Axis Wind Turbine is the primary focus zone of this present study.

2.2 History of Wind Power

From ancient times, the use of wind power has gone through peaks and troughs; nevertheless, the potential use of wind energy has never been neglected. People are applying their knowledge and technology for transforming the wind kinetic energy into mechanical power. But it is not very easy to predict the actual time when the first wind machine was used. According to the historical record, wind propelled the boats along the Nile River as early as 5,000 B.C. and pumped water in between 500 & 900 B.C. However, only the vertical axis wind machines found at the borders of Persian-Afghan at 200 BC and the horizontal-axis wind machines ground at the Netherlands and the Mediterranean following much later (1300-1875 AD) [4]-[6]. In this aspect, from the ancient period to the end of the 19th century may be recognized as the "Ancient Development Period." Whereas, from the end of the 19th century to the present may be named as "Modern Development Period."

2.3 Review of Existing Prediction Model

Over the past decades, rigorous research activities on wind turbine machines have performed to harness more significant amounts of wind energy. People are developing their mathematical modeling, computational simulation, and experimental work on different wind turbine models to enhance their efficiencies. With that, conventional methods and theories are also used to predict the different characteristics. A brief description of the existing literature review, along with their prediction models, is given below:

Propeller and wind turbine work almost in the same principle because wind turbines extract air power from the environment and convert it to mechanical power. In contrast,

propellers create rate of momentum change into the air. That is why with some minor modification of the wind machines, conventional theories of airfoils can be applied to wind machines. The conventional approaches are Momentum Theory, and another is Blade Element theory.

Before the theoretical analysis or the experimental investigation, researchers worked on the available theories to determine how the forces act on the rotor of the wind turbine. A Control Volume Approach designed by Rankine [7] contained an Actuator Disk for the marine propellers. Then it was also modified for wind machines in the analysis. Induced velocity through the actuator disk is assumed to be constant. Along with that, the surface of the disk is considered as a body of revolution. Blade Element theory or the Strip theory used frequently for analyzing the performance of Horizontal axis wind turbines [8]. In this theory, it is considered that "the forces acting on the blade element are solely due to the lift and drag characteristics of the sectional profile of the element [9]".

There are some limitations in the application of the momentum theory due to the reverse flow regions in the downstream in the rotor. The fluid flow patterns at the different positions of blades are shown in the fig 2.1[10]

a) The Propeller state

b) The Windmill state

c) The Turbulent wake state

d) The Vortex ring

A stall occurs at a critical angle of attack when predicting the performance of a HAWT at low tip speed ratios. Walker [11] developed a method for the shape of blades for extracting maximum power. The author made the blades with varying the chord length and twist angle radially at different sections until the power coefficient gained maximum. This happened at the maximum lift to drag ratio of the elemental blade.
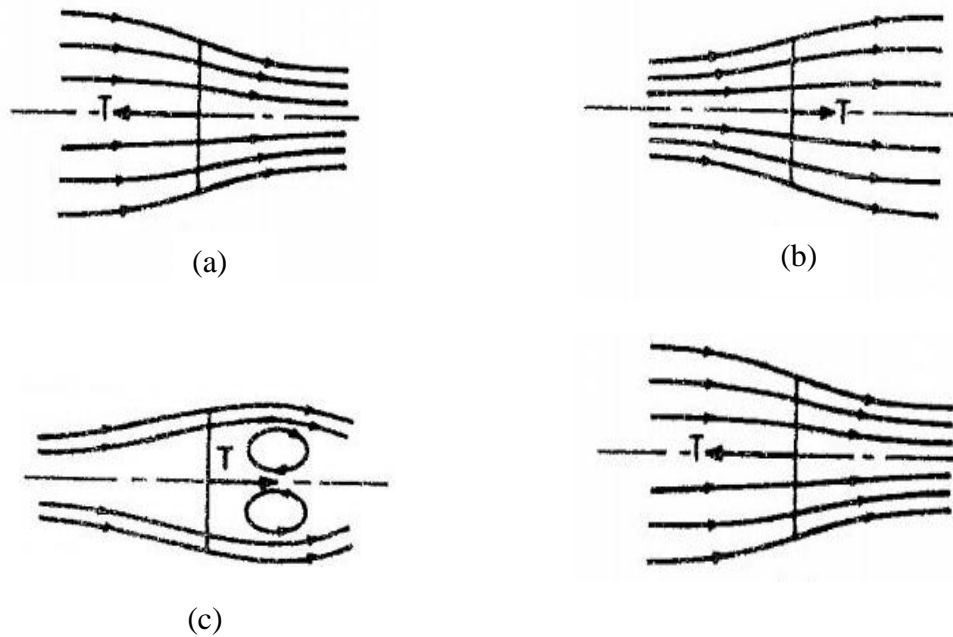
Fig. 2.1 Working states of a rotor: a) The Propeller state b) The Windmill state c) The Turbulent wake state d) The Vortex ring [10]

Hirsch et al. [12] had developed a method for calculating the overall performance and design parameters of a HAWT. Blade dimensions i.e., root chord, tip chord, blade length, thickness, and performance measured based on conventional theories. In their paper, Islam et al. [13] developed a method for predicting the performance criterion of a HAWT by applying the cascade theory. An empirical relation used to find out the induced velocity through the rotor.

Pandey et al. [14] carried out some experimental tests in wind turbines on circular arc steel plates. The camberness ratio varied from 0 to 14% to measure their lift and drag coefficients. The experimental analysis conducted at Reynolds number 2.23×10^5 and the angle of attack varied from -20∘ to 90∘. They concluded that the maximum lift to drag ratio obtained 25 with 8% camber ratio over the angle of attack varying from -20^0 to 90^0. Considering that fact, they concluded that an 8% cambered blade would be the most suitable alternative in low capacity wind energy machines.

Bruining et al. [15] did some experiments to predict the effects of rotation on lift and drag coefficients of a rotor blade. Before that, authors did some tests on the same blade in a wind tunnel. Then concluded the effect of rotation with the stationary rotor blade. Based on the performance characteristics, authors calculated the flow separation point more reliably. In their paper, Islam et al. [16] mentioned that some of the areas or regions in Bangladesh has satisfactory wind speed for pumping and generating electricity.

Fixed pitch wind turbine blades provide maximum efficiency only in a short range of wind speed. Serra and Schoor [17] investigated the variable pitch system. Authors concluded that there is a possibility for working in a wide range of wind speed fluctuations to gain an increased power output with a variable pitch system. Authors represented a comparative assessment of the performance parameters between a fixed type and variable type pitch system.

A.Z.A. Saifullah et al. [18] in their paper appraise the possibility of potential wind energy in Bangladesh as a sustainable energy source. Author analyzed the speed of six coastal zones i.e., Patenga, Cox's Bazar, Teknaf, Char Fassion, Kuakata, and Kutubdia. The author investigated a wind firm with an array of 5104 HAWT having rotor diameter 75m and a hub height of 100m in a wind speed of 7m/s. Authors mentioned by utilizing the wind energy sources properly, and there is a possibility of compensating 11.25% of total power demand by 2020.

During the performance analysis of HAWT, major concerning factors are unsteady aerodynamics, atmospheric turbulence, interference, and wake effects. Leclerc et al. [19] recommended a way to predict the performance of an array of wind turbines. He applied incompressible Navier-stokes equations with a turbulence model. The conventional blade element theory used for determining the force distribution to the rotor model. Finite Element Method with control volume was used for solving the mathematical model. Two

models used for the investigation i.e., isolated wind turbines and another was one behind another. They found a performance degradation in the case of two turbines.

Mesquita et al. [20] reviewed the conventional strip theory to predict the performance and applications of HAWT. In his modeling, author made some assumptions that blades were nothing but some independent stream tubes in which span-wise flow was negligible. The effects of cascades weren't taken into consideration and applied some correction factors to compensate for the losses made by tip-loss and turbulence wake-effects. Author compared his model with the experimental results available in the literature. He found that fast-moving turbines i.e., tip speed ratio greater than 2, provide similar results like the proposed model.

Most. Hosney Ara Begum [21] proposed a circular arc section instead of a conventional airfoil section in case of a low tip speed ratio. Author made a wind turbine rotor model using a circular arc blade profile and did some experimental and theoretical calculations to predict the performance parameters over a conventional NACA 4418 blade airfoil. Author found that the starting torque distribution with a circular arc section was more prominent than that NACA 4418 blade section. Author also concluded that the power coefficient at lower tip speed ratio (less than 6) was prominently enhanced compared to those NACA 4418 blade sections.

Tip loss effects are significant criteria for predicting wind turbines performance while using the conventional blade element theory. Prandtl tip loss function which is generally used for calculating the tip loss effect. Wen Zhong Shen et al. [22] proposed a new tip loss correction model to predict the inconsistency concerning the available models. The proposed model could be used to find better predictions in the tip region.

Maughner [23] designed some winglet configurations for the high-performance sailplanes for enhancing the effectiveness of the sailplanes. Author mentioned that factors

like planform shape, winglet length, winglet height, cant angles, twist angles, toe angles should be considered while investigating the performance criteria of the wind machines. Each parameter had an essential phenomenon in improving winglet performance as well as wind turbines. Author also mentioned that the planform shape would be employed to control the span-wise flow to reduce the induced drag. Jeppe Johansen and Niels N. Sørensen [24] pursued some numerical investigation on the wind turbine blades with winglet configurations using computational fluid dynamics. Author investigated five winglets with camber airfoil and varying in twist angles. Author found that incorporating winglets at the tip of the blades, increased the force distribution on the outer portion around 14%. That, in turn, enhanced the power generation of around 0.6% to 1.4% for wind speed higher than 6%. Furthermore, author concluded that thrust increased by about 1 % to 1.6%.

Wang Jian-Wen et al. [25] accomplished some numerical simulation on a wind turbine with a tip vane to observe the effects and pressure distribution over the blade surface. While doing this, he selected an airfoil section of FX74C16140 along with a 1.16m diameter of a wind turbine. The blade length, tip chord length, and tip vane dimensions were 0.5m, 0.1m, and (8.8cmX8cm). Using the ANSYS Fluent as the solver, author found that "the pressure difference between the suction and pressure surface of the blade increases the force which helps the blade to absorb more wind energy." Thus, the wind turbine power output is enhanced.

Blade element momentum (BEM) is one of the primary methods for designing the wind turbine rotor model, which involves the combination of momentum and blade element theories. Turbine blades are divided into different segments, and a set of equations are then applied to balance the axial and angular momentum of each element. Manwell et al. [26] mentioned in their book that this theory fails to predict wind velocity in the wake region because of the turbulence near the blade surface and recirculation zone.

12

To address the tip losses in wind turbines has been a great challenge by using the BEM methods. Thus, many researchers give several correction factors to improve the BEM method's inconsistency, namely Prandtl's tip loss correction. Wen Zhong Sen et al. [27] gave some correction factors based on Prandtl's tip loss function and then analyzed to check the performance. A comparison between the experimental and numerical simulation showed a better result in the prediction of performance parameters in the tip region. Drew Gertz et al. [28] investigated two different types of winglet incorporating at the tip of a 3.3m diameter wind turbine. Author kept the Cant angle the same but varied the twist and toe angles. Winglet sweep and twist angles are accounted for the load distribution. Meanwhile, the toe angle influences the aerodynamic effect on the winglet. Further, the cant angle affects the upwards and downwards flow direction along the wing. The experimental analysis conducted and a comparison made between with and without winglets ranging the tip speed ratio from 0 to 12. An increase of around 2% to 8% of the power coefficient was found for both the models. They also mentioned that the accuracy of predicted results was found at tip speed ratios greater than 6.5.

Winglet, as an extension of a blade, reduces the tip vortices, which has a similar cross-sectional area as the root of the blade. The vortices are generated due to the downwash effect at the blade. Incorporating the winglet at the tip helps to extract more wind energy and provides a considerable influence in fluid flow. The effectiveness of the wind turbine increases by adding wingtips, and this is done by shifting the vortices away from the rotor region. Thus, the effects of the downwash dwindled and also the induced drag [29].

Saravanan et al. [30] studied four different winglet configurations, fabricated with Glass Fibre Reinforced Plastic materials, to investigate the performance for a rotor model with and without load conditions. The maximum power coefficient for a particular winglet configuration was about 0.43. Author mentioned that, at a low wind speed region, wind

13

turbines with winglets work most accurately. Author concluded that with a small curvature radius along with an optimum winglet height, blades capture a more significant amount of wind energy compared to without winglets.

Monier Elfarra et al. [31] investigated the aerodynamic characteristics of horizontal-axis wind turbines by using CFD and four different winglet configurations. Author utilized and optimized the twist and cant angles to observe the effects on the wind turbine's performance. Author found that performance enhanced by 9% while using a winglet with a 1.5% extension of blade length and faced in the suction side having 45° and 2° cant and twist angles, respectively. Hafidz Ariffudin et al. [32] used CFD to analyze the performance of HAWT with numerous tip devices comprising swept tip, sword tip, upwind winglet, and downwind winglet. Authors found those tip extensions (swept tip, sword tip) performance was better than those winglet configurations (upwind winglet, downwind winglet). At lower tip speed ratio (below 4), swept tip increased power coefficient of almost 9.1% as opposed to the base wind turbine.

Ostovan and Uzol [33] studied two interfacing similar horizontal axis model wind turbines to examine the effects of one another. Both winglets and tip-extensions incorporated separately on the wind turbine and compared with the base model. Winglets had a remarkable increment in the power coefficient as well as the thrust coefficient. But while the second turbine was located at the downstream position in line with the upwind turbine having winglets produced less quantity of power for the downward direction turbine.

Zhu et al. [34] focused on the directions of winglet attachment, including suction side, pressure side, and both sides of the primary blade to investigate their effects in wind turbines. Authors showed that the power generation enhanced for fusion winglets with increasing the tip speed ratio to raise a peak of the power of about 3.91%. Farhan et al. [35]

focused on the two particular airfoils (PSU 94-097 and S809) and the winglet planform to investigate the wind turbine performance. By doing the computational analysis, author concluded that an improvement in performance occurred when a rectangular winglet of 15cm and S809 airfoil was used along with 45 cant angle.

Yaşar Ostovan et al. [36] studied the effects of winglet at the vicinity of the wake flow tip region and the characteristics of the tip vortex of a three-bladed HAWT at a distance of 0.94m diameter downstream by using practical image velocimetry. Vortex core size, Vortex convection, core expansion, and the resultant induced drag on the rotor were investigated. Authors found that vorticity and turbulent kinetic energy substantially decreased across the wake boundary, which moved radially outwards. The quantity of turbulent kinetic energy and vorticity lessened over 50%. Finally, around 15% of induced drag was reduced due to the addition of winglets.

Frederik Zahle et al. [37] worked on the existing wind turbine blade and redesigned a new blade tip to enhance the energy harnessing processes. Author modified the twist, chord, and blade length extension to give a new winglet. They adopted CFD methods to make a surrogate model, which tip section modified numerically to various geometric and load-based limitations. Authors concluded that about 2.6% of power augmentation was due to the winglet addition, whereas an increase of only 0.76% for the straight blade extension. Furthermore, winglets didn't increase the bending moment in the direction of the flap at a 90% radius. Hernan et al. [38] presented various tip devices to observe the induced drag generated at the tip of the blade by using computational analysis. Author studied different types of tip vanes like winglets, split types, and tip-tanks to improve the aerodynamic characteristics. Author found that around 4.6% of enhancement in power generation was there when used winglets compared to 3.5% for split types. Furthermore, not an admirable improvement was there for tip-tank configuration.

Ansari et al. [39] studied for evaluating wind speed and pitch angle variation to investigate how the tip vanes enhanced wind turbines' efficiency. For this analysis, authors chose two different tip plates and used finite volume codes for simulation. Authors found that tip plates showed substantial improvement in power output while working at maximum pitch angle with a particular range of wind speeds as both the trailing edge vortices and span-wise flow were at their minimum level. As wing extensions, namely winglets, which can undermine the vortex's effects at the tips of the blades, Khalafallah et al. [40] studied on straight blades as well as sweep blade winglets to enhance the performance of HAWTs'. Authors considered both the upward and downward facing of winglets of the blades with other parameters like cant and twist angles. Using ANSYS Fluent, authors found an augmentation of power coefficient of about 4.39% at design TSR while incorporating the tip extensions. This improvement happened when the swept blade with winglets direction was in the upstream position.

Khaled et al. [41] considered two winglet parameters, namely winglet height, and cant angle to present the effectiveness in HAWT performance. Authors used CFD methods and artificial neural networks and varied the winglet height ranging from 1% to 7% of the turbine rotor and cant angle ranging from 15 to 90. Authors concluded an admirable increment of about 8.787% in both power and thrust coefficient was there because of the winglets. The best configuration was, having a cant angle of 48.30 and a winglet length of around 6.30%. Motsamai et al. [42] studied how a wind turbine provides better performance keeping its size at an optimum level. Author focused on configurations, namely, winglet at the blade tip and trailing edge flap and combined of the two. Author considered a straight blade of NREL turbine and used ANSYS Fluent for investigation. Wind turbine blade having a winglet provides the maximum aerodynamic torque of about 9% compared to the baseline blade. In contrast, it reduces the flapwise bending moment by about 12%.

Meanwhile, combined winglet and trailing edge flap alleviated the effects of torque and flapwise bending loads by 7.6% and 11%, respectively.

Zhang et al. [43] studied Vertical axis wind turbines (VAWTs) as they are very potential in harnessing wind energy. Authors focused on the aerodynamic effects of those blades due to tip vortex and considered the orthogonal experimental design (OED) method to measure the different performance parameters. The results showed that the twist angle in the winglet provides the best possible output power. An increase of about 31% in power coefficient was there due to the incorporation of winglets at TSR of 2.19 compared to without winglet models. As winglets work as a means for diminishing the tip vortices as well as induced drag, Mourad et al. [44] focused on these effects. Authors considered the winglet height and toe angle as the performance criteria and took a three-bladed rotor with SD8000 airfoil as the prototype model. Authors kept toe angle constant at zero and chose four types of winglet height. A height of 0.8%R showed the best performance and enhanced power of about 2.4% at TSR 7. By using an optimum winglet height and toe angle, the power coefficient can be raised almost 6% compared to without winglets.

Since Bangladesh is a developing nation, it needs a lot of electricity to keep pace with its ongoing development and meet the electricity needs of the people. After generating electricity through renewable sources like hydropower, solar energy, etc., the government has paid particular attention to power generation from another renewable source, wind. The Government of Bangladesh has established a target of generating 1360 MW of electricity from wind power by 2030 and a total of 1153 MW of electricity generation from wind energy sources by 2021[45]. The overall electricity generation scenario till now from different green energy sources, including wind energy, is described in Fig. 2.2. Also, the prospects for different projects taken by Bangladesh Power Development Board (BPDB) is depicted in Table 2.1.
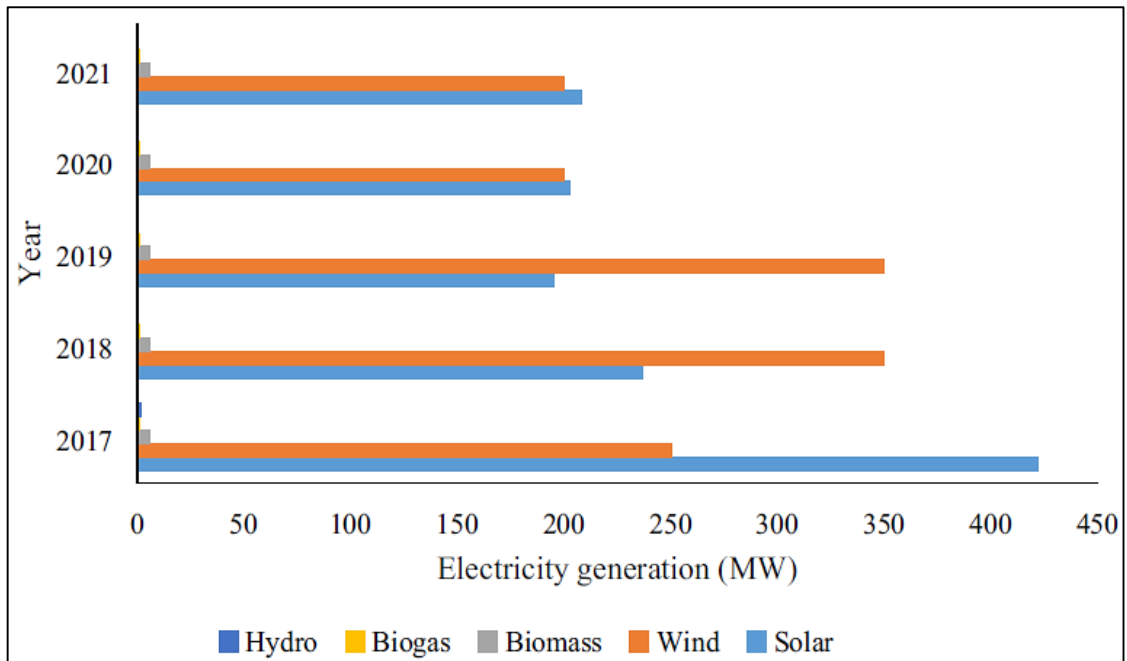
Fig. 2.2 Electricity production scenario by different renewable energy resources in Bangladesh [46]

Table 2.1. BPDB wind energy projects in Bangladesh [47].

Location	Capacity
Muhuri Dam of Sonagazi in Feni	900 kW
Kutubdia	1000 kW
Muhuri Dam Area of Feni, Mognamaghat of Cox's bazar	15 MW
Parky Beach of Anwara in Chittagong	15 MW
Kepupara of Borguna and Kuakata of Patuakhali	15 MW
Muhuri Dam Area of Feni	15 MW

CHAPTER 3

AERODYNAMICS OF HAWT

3.1 General

The essential function of a wind turbine is to extract the kinetic energy from the available flow of air. For the performance analysis of horizontal axis wind turbines, many designers applied different conventional theories. Among them, the strip theory is the most renowned one for predicting performance. This theory is also known as the modified blade element theory as it is the combination of axis momentum theory and blade element theory. The vortex theory can also be used for investigating the performance analysis of wind turbines. But the computational time is too much and can't even predict the flow separation [48]. Thus, in this present study, only the classical or strip theory has been used to analyze wind turbines' performance.

3.2 Axial Momentum Theory (Actuator Disk Theory)

Axial momentum theory is the simplest method for predicting the aerodynamic characteristics of wind turbines. Using the above process, it is possible to measure the aerodynamic forces acting in the rotor, as they are responsible for the fluid motion, leading to power output.

When wind turbines are operating in the steady-state condition is a free-moving wind stream with constant velocity, the velocity per unit volume dramatically decreases as is moving towards the turbine blades, passes through it, and starts to move away from it. Being a certain distance from the turbine blades, it will acquire the kinetic energy again, and velocity increases until it reaches to free stream velocity. Let us assume the control volume as shown in Fig. 3.1.

$$T = A\,(p^+ - p^-) \tag{3.4}$$
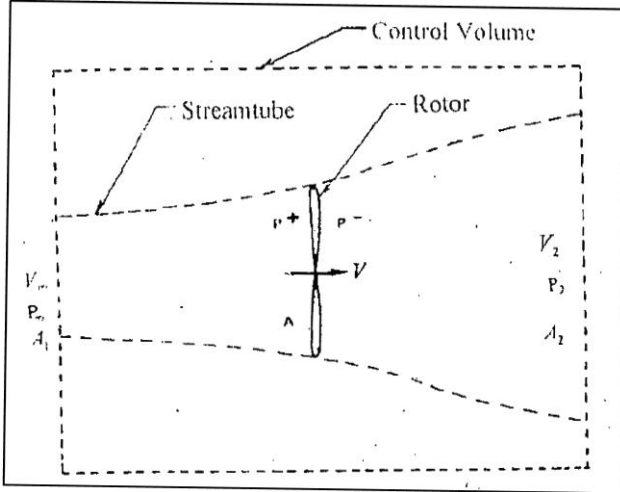
Fig. 3.1 Control volume of a wind turbine [49]   **Fig. 3.2** The variation in C_P and C_T with axial induction factor [50]
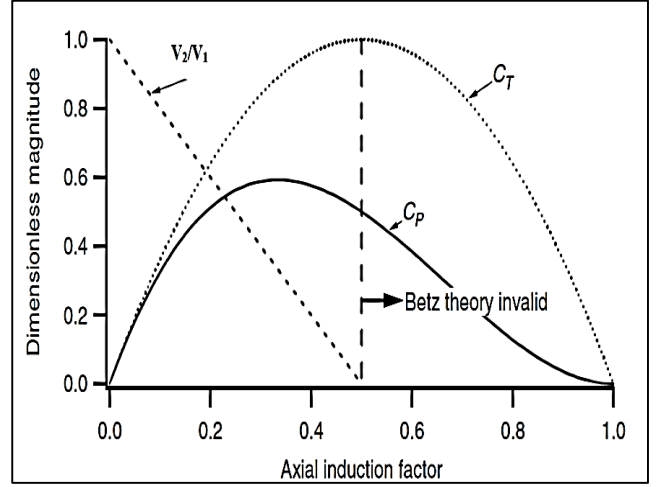
Introducing Bernoulli's equation,

For upstream of the rotor, $P_\infty + \frac{1}{2}\rho V_\infty^2 = P^+ + \frac{1}{2}\rho V^2$ \hfill (3.5)

For downstream of the rotor, $P_\infty + \frac{1}{2}\rho V_2^2 = P^- + \frac{1}{2}\rho V^2$ \hfill (3.6)

One finds by subtracting equation (3.6) from equation (3.5),

$$p^+ - p^- = \frac{1}{2}\rho(V_\infty^2 - V_2^2) \tag{3.7}$$

From equations (3.4) and (3.7), the expressions for the thrust can be written as,

$$T = \frac{1}{2}\rho A(V_\infty^2 - V_2^2) \tag{3.8}$$

Equating the expressions of thrust from equations (3.8) and (3.3),

$$\frac{1}{2}\rho A(V_\infty^2 - V_2^2) = \rho A V(V_\infty - V_2)$$

By simplification,

$$V = \frac{V_\infty + V_2}{2} \tag{3.9}$$

20

The rotor velocity V is often defined in terms of an axial induction factor "a" as,

$$V = V_\infty (1 - a) \tag{3.10}$$

Now from equations (3.9) and (3.10), the wake velocity V_2 can be expressed as,

$$V_2 = V_\infty (1 - 2a) \tag{3.11}$$

From the momentum theory, the change in kinetic energy of the mass flowing through the rotor area is the power absorbed by the rotor and is given by,

$$P = m\Delta KE = \frac{1}{2}\rho AV(V_\infty^2 - V_2^2) \tag{3.12}$$

Introducing equation (3.10) and (3.11) in equation (3.12), the expressions for power becomes,

$$P = 2\rho AV_\infty^3 a(1 - a) \tag{3.13}$$

This is a cubical equation of velocity and the maximum power occurs when first derivative of P with respect to "a" becomes zero,

$$i.e. \frac{dp}{da} = 0$$

From equation (3.13), one obtains the derivative,

$$\frac{dp}{da} = 2\rho AV_\infty^2 (1 - 4a + 3a^2) = 0$$

Solving for "a" gives, a $= \frac{1}{3}$, this is the value of optimum interference factor. Inserting (3.13), the expressions for maximum power becomes,

$$P_{max} = \frac{16}{27}(\frac{1}{2}\rho AV_\infty^3) \tag{3.14}$$

Here the factor 16/27 is called the "Betz-coefficient" [51], and it represents the maximum fraction of power, which an ideal rotor can extract from the flow. This fraction 16/27 is related to the power of an undisturbed flow, which arrives at area A, whereas in

reality, the mass flow rate through A is not $\rho\, AV\infty$ but is equal to $\rho\, AV$. So the maximum efficiency, η_{max} for the maximum power output can be expressed as,

$$\eta_{max} = \frac{P_{max}}{\frac{1}{2}\rho AVV_\infty^2} = \frac{16}{27} * \frac{3}{2} = \frac{8}{9} \qquad\qquad 3.15)$$

The theory described above is called the axial momentum theory for a non-rotating wake, as it does not consider the additional effects of wake rotation. The incoming stream is not rotational, and interaction of the stream with the rotating windmill causes the wake to rotate in the opposite direction. As the wake contains both the kinetic energy together with the translational kinetic energy, then it is expected to have lower power extraction than in the case of the wake having only transitional kinetic energy.

Figure 3.2 illustrates, both the coefficient of power of an ideal turbine in dimensionless magnitude and axial induction factor. The graph represents that the maximum efficiency of ideal turbine can be achieved almost of 59% when the axial induction factor is less than 0.4.

3.2.2 Effect of Wake Rotation

The linear momentum theory neglect the rotation of flow at the wake of the turbine, while in practical flow, there are constant rotational flow leaves form the turbine and moves downward direction. Then an equal and opposite torque applies to the turbine by moving air and on moving air by the turbine. Thus, air starts to rotate in the reverse direction of the turbine. Because of the presence of rotational energy in the wake, less energy is extracted by the turbine and thus losses in kinetic energy production.

For the consideration of the effect of wake rotation, the assumptions are:

a) At the upstream of the rotor the flow is entirely axial

b) At the downstream of the flow it rotates with an angular velocity w but remains irrotationa1.

c) The angular velocity of the downstream flow ω is assumed to be small compared to the angular velocity Ω of the wind turbine itself

These assumptions maintain that the pressure is equal in both the wake region and in the free stream, which is an approximation of axial momentum theory. The torque Q's product acting on the rotor and the angular velocity Ω of the rotor gives the power. To get maximum power, it is essential to have a high angular velocity and low torque because high torque will cause massive wake rotational energy. The angular (or tangential) interference factor a' relates the angular velocity ω of the wake and the angular velocity Ω of the rotor in the following way,

$$\text{a}' = \frac{Angular\ Velocity\ of\ the\ wake}{Twice\ the\ angular\ velocity\ of\ the\ rotor} = \frac{\omega}{2\Omega} \tag{3.16}$$
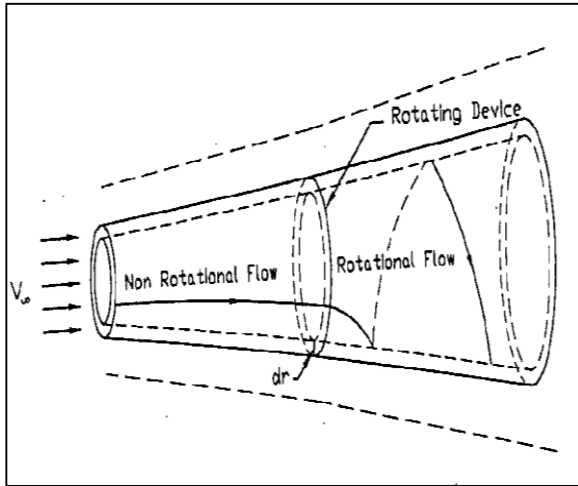
Fig. 3.3 Stream tube model showing the rotation of the wake [49]
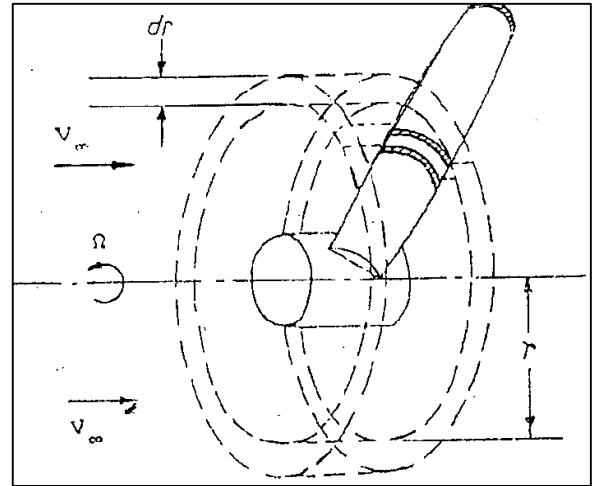
Fig. 3.4 Blade element annular ring [49]

The annular ring through which a blade element will pass is shown Fig. 3.4.The axial thrust force dT can be expressed as the product of elemental 'mass flew rate dm and the change of velocity.

$$dT = dm(V_\infty - V_2) = \rho dAV(V_\infty - V_2) \tag{3.17}$$

Substituting the values of V and V_2 from equations (3.10) and (3.11) into equation (3.17) and expressing the area of the annular ring dA as,

23

$$dA = 2\pi r dr \tag{3.18}$$

The thrust can be written as Lysen et al. [52],

$$dT = 2\pi r \rho V_\infty (1-a)[V_\infty - V_\infty (1-2a)]dr = 4\pi \rho r V_\infty^2 a(1-a)dr \tag{3.19}$$

On the other hand, using the Bernoulli's equation, the thrust force can also be determines from the pressure difference over the blades. Bernoulli's equation yields, as the relative angular velocity changes from Ω to ($\Omega + \omega$) where ω is the wake rotational velocity

$$p^+ - p^- = \frac{1}{2}\rho(\Omega + \omega)^2 r^2 - \frac{1}{2}\rho \Omega^2 r^2 = \rho(\Omega + \frac{1}{2}\omega)\omega r^2$$

Replacing ω by $2\Omega a'$ as obtained from the equation (3.16),

$$dT = 4a'(1-a')\frac{1}{2}\rho \Omega^2 r' 2\pi r dr \tag{3.20}$$

From equations (3.19) and (3.20) one finds,

$$\frac{a(1-a)}{a'(1+a')} = \frac{\Omega^2 r^2}{V_\infty^2} = \lambda_r^2 \tag{3.21}$$

Where, "λ_r" is the local tip speed ratio and is expressed as,

$$\lambda_r = \frac{\Omega r}{V_\infty} \tag{3.22}$$

Let us now derive an expression for the torque Q acting on the rotor for which the change in angular momentum flux through the annular ring is considered. The elemental torque is given by,

$$dQ = dm V_t r = \rho \omega r V r dA$$

The expression for the torque acting on the annular ring is obtained from equations (3.10), (3.16), and (3.18) as,

$$dQ = 4\pi r^3 \rho V_\infty (1-a)a' \Omega dr \tag{3.23}$$

The power generated through the annular ring is equal to,

$$dp = \Omega dQ$$

Which is integrated to obtain,

$$P = \int_0^R \Omega dQ \qquad (3.24)$$

The tip speed ratio is defined as,

$$\lambda_r = \frac{\Omega R}{V_\infty} \qquad (3.25)$$

Substituting the value of dQ from equation (3.23) into equation (3.24), the expression for total power becomes,

$$P = \int_0^R 4\pi r^3 \rho V_\infty (1-a)a'\Omega^2 dr = \frac{1}{2}\rho A V_\infty^3 \frac{8}{\lambda^2} \int_0^\lambda a'(1-a)\lambda_r^3 d\lambda_r \qquad (3.26)$$

In the above expression, "A" is the turbine rotor swept area which is given by, $A = \pi R^2$

Power coefficient is defined as,

$$C_P = \frac{P}{\frac{1}{2}\rho A V_\infty^3}$$

Inserting the value of power P from equation (3.26), the expression of power coefficient can be written as,

$$C_P = \frac{8}{\lambda^2} \int_0^\lambda a'(1-a)\lambda_r^3 d\lambda_r \qquad (3.27)$$

From equation (3.21) the tangential interference factor "a'" In terms of axial interference factor "a" becomes,

$$a' = -\frac{1}{2} + \frac{1}{2}\sqrt{[1 + \frac{4}{\lambda_r^2}a(1-a)]} \qquad (3.28)$$

Inserting value of "a'" from equation (3.28) into equation (3.27) and taking derivative of Cp equal to zero for maximum power coefficient, the expression of λ_r in terms of "a" becomes,

$$\lambda_r = \frac{(1-a)(4a-1)^2}{1-3a} \qquad (3.29)$$

From equations (3.21) and (3.29), the relation between $"a"$ and $"a'''"$ can be obtained as,

$$a' = \frac{1 - 3a}{4a - 1} \tag{3.30}$$

3.3 Blade Element Theory (BET)

The Blade Element Theory is used to predict the aerodynamic forces acting on a blade through lift and drag forces generated at span wise of the blade sections shown in Fig. 3.5. Here, the entire blade is fragmented into several sections in the span wise direction. Each part of the blade is independent of the other and operates aerodynamically as a 2D airfoil. The aerodynamic forces are calculated on each airfoil at every section of the blade. The sum of all forces at each section is then accumulated to calculate the forces and moments that have been exerted on the turbine blade.

Assumptions:

a) Along each blade, there is no interference between the adjacent blade elements.

b) The forces acting on the blade element are determined from only the lift and drag characteristics of the element's sectional profile.

c) The pressure in the far wake is equal to that of the free stream.
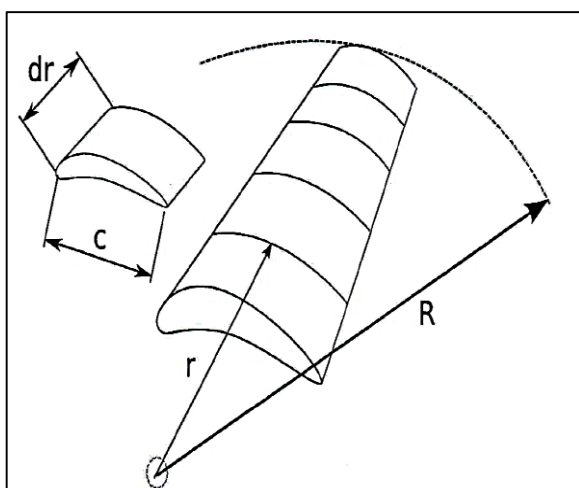
Fig. 3.5 Wind turbine blade divided into a series number of sections.   **Fig. 3.6** Velocity diagram of a blade element.
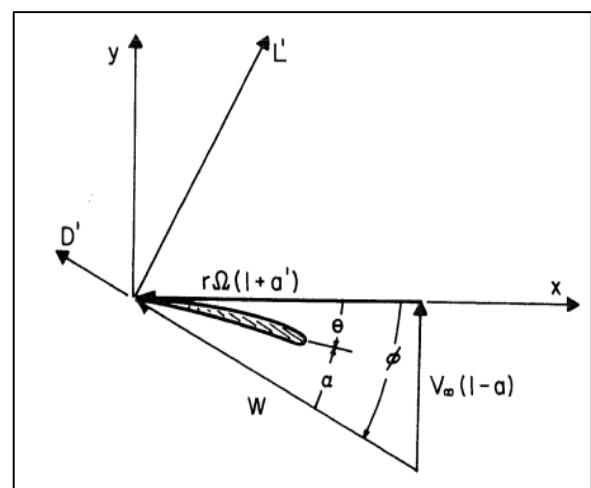
The aerodynamic force components acting on the blade element are shown in Fig. 3.6; where, x-y coordinate system is used. Among the forces the lift force component dL acts perpendicular to the resulting velocity vector W and the drag force component dD acts in the same direction of the resulting velocity vector. The sectional lift and drag forces may be defined as,

$$dL = C_L \frac{1}{2} \rho W^2 C dr \tag{3.31}$$

$$dD = C_D \frac{1}{2} \rho W^2 C dr \tag{3.32}$$

From the geometry of the figure the thrust and torque experienced by the blade element are given by the following expressions,

$$dT = dL \cos \phi + dD \sin \phi \tag{3.33}$$

$$dQ = (dL \sin \phi - dD \cos \phi) r \tag{3.34}$$

Assuming that "B" is the number of blades of the rotor, the expressions for the thrust and torque can be written as,

$$dT = BC \frac{1}{2} \rho W^2 (C_L \cos \phi + C_D \sin \phi) dr$$

$$dT = BC \frac{1}{2} \rho W^2 C_L \cos \phi (1 + \frac{C_D}{C_L} \tan \phi) dr \tag{3.35}$$

$$dQ = BC \frac{1}{2} \rho W^2 (C_L \sin \phi - C_D \cos \phi) dr$$

$$dQ = BC \frac{1}{2} \rho W^2 C_L \sin \phi (1 - \frac{C_D}{C_L} \frac{1}{\tan \phi}) r dr \tag{3.36}$$

From Fig. 3.6, the relative velocity can be expressed as,

$$W = \frac{(1-a)V_\infty}{\sin \phi} = \frac{(1+a')\Omega r}{\cos \phi} \tag{3.37}$$

From the geometry of fig. 3.6, the following trigonometric relations can be obtained,

$$\tan \phi = \frac{(1-a)V_\infty}{(1+a')\Omega r} = \frac{1-a}{1+a'} \frac{1}{\lambda_r} \tag{3.38}$$

Also. $\beta = \emptyset - \alpha$ (3.39)

On the other hand, the local solidity ratio σ_r can be expressed as,

$$\sigma_r = \frac{BC}{2\pi r}$$ (3.40)

Finally, the equations of blade element theory from equations (3.35) and (3.36) in terms of local solidity ratio σ_r, becomes,

$$dT = (1-a)^2 \frac{\sigma_r C_L \cos\phi}{\sin^2\phi}(1+\frac{C_D}{C_L}\tan\phi)\frac{1}{2}\rho V_\infty^2 2\pi r dr$$ (3.41)

$$dQ = (1+d)^2 \frac{\sigma_r C_L \sin\phi}{\cos^2\phi}(1-\frac{C_D}{C_L}\frac{1}{\tan\phi})\frac{1}{2}\rho\Omega^3 r^3 2\pi r dr$$ (3.42)

3.4 Strip Theory

The performance of a wind turbine can be determined by developing a couple of relationships from the axial momentum theory and blade element theory. To do this, the thrust obtained from the momentum theory [equation (3.19)] is equated to the thrust derived from the blade element theory for an annular element at radius r [equation (3.41)]

$$dT_{momentum} = dT_{bladeelement}$$

Which gives,

$$\frac{a}{1-a} = \frac{\sigma_r C_L \cos\phi}{4\sin^2\phi}(1+\frac{C_D}{C_L}\tan\phi)$$ (3.43)

This is an important relation which relates axial interference factor "a" with the local solidity ratio σ_r, together with the lift coefficient C_L and the drag coefficient C_D. On the other hand, equating the expression of angular momentum obtained from the momentum theory [equation (3.23)] with the expression of the same obtained from the blade element theory [equation (3.42)] and substituting equation (3.38), one finds,

$$dQ_{momentum} = dQ_{bladeelement}$$

$$\frac{a}{1+a'} = \frac{\sigma_r C_L}{4\cos\phi}(1-\frac{C_D}{C_L}\frac{1}{\tan\phi})$$ (3.44)

Equation (3.44) determines the angular interference factor, which contains the lift coefficient and the local solidity ratio.

The drag coefficient C_D should be omitted in the calculations of axial interference factor "a" and the tangential interference factor "a" because the retarded air due to drag is confined to thin helical sheets in the wake and have little effect on the induced flow as described by Wilson and Lissaman [53]. Thus inserting the drag coefficient $C_D=0$, the expressions of the interference factors can be obtained as,

$$\frac{a}{1-a} = \frac{\sigma_r C_L \cos\phi}{4\sin^2\phi} \tag{3.45}$$

$$\frac{a'}{1+a'} = \frac{\sigma_r C_L}{4\cos\phi} \tag{3.46}$$

Inserting equation (3.45) into equation (3.41), the relation of the elemental thrust can be determined as,

$$dT = 4a(1-a)(1+\frac{C_D}{C_L}\tan\phi)\frac{1}{2}\rho V_\infty^2 2\pi r dr \tag{3.47}$$

Also inserting equations (3.46) and (3.38) into equation (3.42), the expression of the elemental torque can be written as,

$$dQ = 4a'(1-a)(1-\frac{C_D}{C_L}\frac{1}{\tan\phi})\frac{1}{2}\rho V_\infty \Omega 2\pi r^3 dr \tag{3.48}$$

The elemental power can be expressed as,

$$dp = dQ\Omega$$

Now substituting the expression of dQ from equation (3.48) in the above equation, one obtains,

$$dP = 4a'(1-a)(1-\frac{C_D}{C_L}\frac{1}{\tan\phi})\frac{1}{2}\rho V_\infty \Omega^2 2\pi r^3 dr \tag{3.49}$$

Introducing the local tip speed ratio $\lambda_r = \frac{\Omega r}{V_\infty}$, from equation (3.25), the expressions of the total thrust, total torque and total power can be obtained integrating equations (3.47), (3.48)

and (3.49) respectively over total tip speed ratio ranging from 0 to λ and the expressions are,

$$Q = \frac{1}{2}\rho A V_\infty^2 R \frac{8}{\lambda^3} \int_0^\lambda a'(1-a)(1-\frac{C_D}{C_L}\frac{1}{\tan\phi})\lambda_r^3 d\lambda_r \tag{3.50}$$

$$T = \frac{1}{2}\rho A V_\infty^2 \frac{8}{\lambda^2} \int_0^\lambda a(1-a)(1+\frac{C_D}{C_L}\tan\phi)\lambda_r d\lambda_r \tag{3.51}$$

$$P = \frac{1}{2}\rho A V_\infty^3 \frac{8}{\lambda^2} \int_0^\lambda a'(1-a)(1-\frac{C_D}{C_L}\frac{1}{\tan\phi})\lambda_r^3 d\lambda_r \tag{3.52}$$

From definition, the coefficients of thrust C_T, the coefficient of torque C_Q and the coefficient of power Cp are as,

$$C_T = \frac{T}{\frac{1}{2}\rho A V_\infty^2} \tag{3.53}$$

$$C_Q = \frac{Q}{\frac{1}{2}\rho A V_\infty^2 R} \tag{3.54}$$

$$C_P = \frac{P}{\frac{1}{2}\rho A V_\infty^3} \tag{3.55}$$

Substituting the values of T, Q and P from equations (3.50), (3.51) and (3.52) in equations (3.53), (3.54) and (3.55) respectively and simplifying, the expressions of the thrust coefficient, torque coefficient and power coefficient can be written as,

$$C_T = \frac{8}{\lambda^2} \int_0^\lambda a(1-a)(1+\frac{C_D}{C_L}\tan\phi)\lambda_r d\lambda_r \tag{3.56}$$

$$C_Q = \frac{8}{\lambda^3} \int_0^\lambda a'(1-a)(1-\frac{C_D}{C_L}\frac{1}{\tan\phi})\lambda_r^3 d\lambda_r \tag{3.57}$$

$$C_P = \frac{8}{\lambda^2} \int_0^\lambda a'(1-a)(1-\frac{C_D}{C_L}\frac{1}{\tan\phi})\lambda_r^3 d\lambda_r \tag{3.58}$$

Equations (3.56), (3.57) and (3.58) can be written in the following forms replacing the local tip speed ratio with equation (3.25) and considering $\psi = \dfrac{r}{R}$

30

$$C_T = 8 \int_0^1 a(1-a)(1 + \frac{C_D}{C_L} \tan \phi) \psi d\psi \tag{3.59}$$

$$C_Q = 8\lambda \int_0^1 a'(1-a)(1 - \frac{C_D}{C_L} \frac{1}{\tan \phi}) \psi^3 d\psi \tag{3.60}$$

$$C_P = 8\lambda^2 \int_0^1 a'(1-a)(1 - \frac{C_D}{C_L} \frac{1}{\tan \phi}) \psi^3 d\psi \tag{3.61}$$

3.5 Tip and Hub Losses

In the preceding sections of this chapter described till now, it is assumed that the rotor has possessed an infinite number of blades with an infinitely small chord. But in reality, the number of blades is finite, and also the chord is finite. According to the theory discussed so far, wind imparts a rotation to the rotor, thus dissipating some of its kinetic energy or velocity and creating a pressure difference between two sides of the blade. At the tip and hub, however, this pressure difference leads to down-wash effects. The flow becomes three-dimensional and tries to equalize the pressure difference, as shown in Fig. 3.7. This phenomenon is more prominent as one approach to the tip. It results in a reduction of torque on the rotor and thus a reduction of the power output. As mentioned by Wilson and Walker, several alternate models exist to take this loss into account [54]. One of these approaches, suggested by Prandtl tip loss correction factors. The idea in Prandtl's method is to replace the system of vortices at the tip with a series of parallel planes for which the flow is more easily calculated.

However, it should be remembered that this approximation was developed for a lightly loaded propeller under optimum conditions, which may differ somewhat from that of a wind turbine. The correction factor suggested by Prandtl is
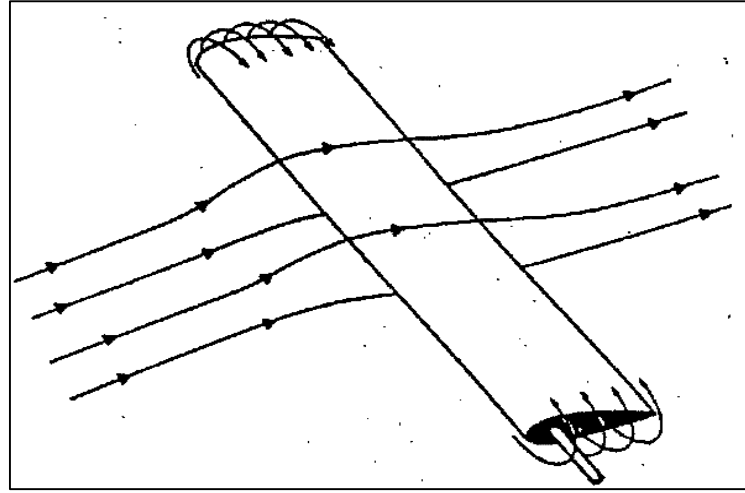
Fig 3.7 Tip and hub losses flow diagram [49].

The correction factor suggested by Prandtl is,

$$F_{tip} = \frac{2}{\pi} arc(\cos e^{-f})$$

Where, f' =Prandtl exponent and is given by

$$f = \frac{B}{2} \frac{R-r}{R\sin\phi}$$

It may also be applied for the hub region and f' is then defined as,

$$f' = \frac{B}{2} \frac{r-r_{hub}}{2r_{hub}\sin\phi}$$

Hence, a correction factor F for total losses is applied as, F=F_{tip}*F_{hub}   (3.62)

     The loss factor F may be introduced in numerous ways for the rotor performance calculation. In the method adopted by Wilson and Lissaman [53], the interference factor "a" and the tangential interference factor " a'" are multiplied by F, and the axial and tangential velocities in the rotor plane as experienced by the blades are modified. It is further assumed that these corrections only involve the momentum equations. Thus the thrust and torque from the momentum theory become,

$$dT = 4\pi\rho r V_\infty^2 aF(1-aF)dr$$

(3.63)

32

$$dQ = 4\pi\rho r^3 V_\infty a' F(1 - aF)\Omega dr \tag{3.64}$$

The results of the blade element theory remain unchanged. Thus the expressions of thrust and toque respectively become,

$$dT = (1 - a)^2 \frac{\sigma C_L \cos\phi}{\sin^2 \phi}(1 + \frac{C_D}{C_L}\tan\phi)\frac{1}{2}\rho V_\infty^2 2\pi r dr \tag{3.41}$$

$$dQ = (1 + a')^2 \frac{\sigma C_L \sin\phi}{\cos^2 \phi}(1 - \frac{C_D}{C_L}\frac{1}{\tan\phi})\frac{1}{2}\rho \Omega^3 r^3 2\pi r dr \tag{3.42}$$

Equation (3.42) can also be written as [from eq. (3.36), (3.37) and (3.40)],

$$dQ = (1 - a)^2 \frac{\sigma C_L}{\sin\phi}(1 - \frac{C_D}{C_L}\frac{1}{\tan\phi})\frac{1}{2}\rho V_\infty^2 r^3 2\pi r^2 dr \tag{3.65}$$

Balancing equation (3.32) and (3.41) one finds,

$$aF(1 - aF) = \frac{\sigma C_L \cos\phi (1 - a)^2}{4\sin^2 \phi}(1 + \frac{C_D}{C_L}\tan\phi) \tag{3.66}$$

Considering equations (3.64) and (3.65),

$$a'F(1 - aF) = (1 - a')^2 \frac{\sigma C_L}{4\sin\phi}(1 - \frac{C_D}{C_L}\frac{1}{\tan\phi})$$

3.6 Expressions for Maximum Power

The expressions for axial interference factor "a", angular or tangential interference factor "a" and the relation between "a" and "a" as obtained from equations (3.45), (3.46) and (3.30) are,

$$\frac{a}{1 - a} = \frac{\sigma_r C_L \cos\phi}{4\sin^2 \phi}$$

$$\frac{a'}{1 + a'} = \frac{\sigma_r C_L}{4\cos\phi}$$

$$a' = \frac{1 - 3a}{4a - 1}$$

Now eliminating a and a' from the above three equations one obtains,

$$\sigma_r C_L = 4(1 - \cos \phi) \tag{3.67}$$

Inserting the value of local solidity ratio from equation (3.40), the above expression becomes,

$$C = \frac{8\pi r}{BC_L}(1 - \cos \phi) \tag{3.68}$$

From equations (3.22) and (3.38),

$$\lambda_r = \frac{\Omega r}{V_\infty}$$

$$\tan \phi = \frac{(1-a)V_\infty}{(1+a')\Omega r} = \frac{1-a}{1+a'}\frac{1}{\lambda_r}$$

Now replacing the value of (1- a) from (3.43) and (1+ a') from (3.44), one obtains:

$$\tan \phi = \frac{4a\sin^2 \phi}{\sigma_r C_L \cos \phi}\frac{\sigma_r C_L}{4a\cos \phi}\frac{1}{\lambda_r}$$

Inserting the value of $\sigma_r C_L$, eliminating a and a' the expression of λ_r, becomes after simplification,

$$\lambda_r = \frac{\sin \phi(2\cos \phi - 1)}{(1 - -\cos \phi)(2\cos \phi + 1)} \tag{3.69}$$

The expression of Φ can be obtained from the above equation as,

$$\phi = \frac{2}{3}\tan^{-1}\frac{1}{\lambda_r} \tag{3.70}$$

From Fig 3.6, the equation of blade twist angle β can be written as,

$$\beta = \phi - \alpha$$

The above expressions are very important for the calculation of blade configuration.

CHAPTER 4

GOVERNING EQUATIONS AND COMPUTATIONAL ANALYSIS

4.1 Introduction

A computational study has been conducted to simulate the three-dimensional wind turbine model with and without winglets before the experimental analysis. All the design parameters of the winglets are finalized depending on the computational results obtained. The steady, viscous, three-dimensional governing equations (continuity and momentum) are described in this chapter and solved by the two-equation turbulence model Realizable k- ε turbulence. ANSYS Fluent 16 software is used to simulate the stated problem.

4.2 Governing Equations

The primary three governing equations are conservation of mass, conservation of momentum, and conservation of energy. Additionally, there are auxiliary equations due to the velocity fluctuation over the entire domain. The differential equations for laminar flows are expressed as [35]:

$$\frac{\partial \rho}{\partial t} + \frac{\partial}{\partial x}(\rho u) + \frac{\partial}{\partial y}(\rho v) + \frac{\partial}{\partial z}(\rho w) = 0 \tag{4.1}$$

$$\rho \frac{Du}{Dt} = \frac{\partial(-p+\tau_{xx})}{\partial x} + \frac{\partial \tau_{yx}}{\partial y} + \frac{\partial \tau_{zx}}{\partial z} + S_{Mx} \tag{4.2}$$

$$\rho \frac{Dv}{Dt} = \frac{\partial \tau_{xy}}{\partial x} + \frac{\partial(-p+\tau_{yy})}{\partial y} + \frac{\partial \tau_{zy}}{\partial z} + S_{My} \tag{4.3}$$

$$\rho \frac{Dw}{Dt} = \frac{\partial \tau_{xz}}{\partial x} + \frac{\partial \tau_{yz}}{\partial y} + \frac{\partial(-p+\tau_{zz})}{\partial z} + S_{Mz} \tag{4.4}$$

$$\rho \frac{D\tilde{u}}{Dt} = K(\frac{\partial^2 T}{\partial x^2} + \frac{\partial^2 T}{\partial y^2} + \frac{\partial^2 T}{\partial z^2}) - p(\frac{\partial u}{\partial x} + \frac{\partial v}{\partial y} + \frac{\partial z}{\partial z}) \tag{4.5}$$

Based on Reynolds's decomposition, the additional fluctuation quantities, i.e., turbulent stresses in the Reynolds Averaged Navier Stokes (RANS) equations, can be written as:

$$\frac{\partial \rho}{\partial t} + \frac{\partial}{\partial x_i}(\rho u_i) = 0 \tag{4.6}$$

$$\frac{\partial}{\partial t}(\rho u_i) + \frac{\partial}{\partial x_j}(\rho u_i u_j) = -\frac{\partial p}{\partial x_i} + \frac{\partial}{\partial x_j}[\mu(\frac{\partial u_i}{\partial x_j} + \frac{\partial u_j}{\partial x_i} - \frac{2}{3}\delta_{ij}\frac{\partial u_i}{\partial x_j})] + \frac{\partial}{\partial x_j}(-\rho \overline{u_i' u_j'}) \tag{4.7}$$

4.3 Turbulence Modeling

Turbulent flow involves eddies and fluctuating velocity field. The primary governing equations can be time-averaged to avoid fluctuating quantities, leading to a modified set of equations. However, these equations contain some unknown equations which are needed to solve. Thus, the Navier-stokes equations can be transmuted in such a modified form by using Reynolds's averaging.

4.4 Selection of Turbulence Modeling

The available turbulence models in this version of ANSYS Fluent are:

a) Spalart -Allmaras model
b) K-ε models (standard, renormalization-group (RNG), realizable)
c) K-ω models (standard, sheer-stress transport (SST))
d) Reynolds Stress models (RSM)
e) Large-eddy simulation (LES) model

The selection of the appropriate turbulence model substantially affects the solution of the specific problems. Numerous studies have been done to predict the aerodynamics of wind turbine models. It is observed that the two equations Realizable k- ε turbulence model predicted the rates of both planner and round jets more accurately. Moreover, it has a superior performance for flows involving rotation, separation, recirculation, and boundary layers with strong adverse pressure gradient [35]. Based on the advantages, the Realizable k- ε turbulence model is chosen for all the computational simulations for the turbine model with and without winglets, where k is the turbulent kinetic energy and ε is the dissipation rate. The two transport equations of Realizable k- ε turbulence model can be defined as:

$$\frac{\partial}{\partial t}(\rho k) + \frac{\partial}{\partial x_j}(\rho k u_j) = \frac{\partial}{\partial x_j}[(\mu + \frac{\mu_t}{\sigma_k})\frac{\partial k}{\partial x_j}] + G_k + G_b - \rho\varepsilon - Y_M + S_k \qquad (4.8)$$

$$\frac{\partial}{\partial t}(\rho\varepsilon) + \frac{\partial}{\partial x_j}(\rho\varepsilon u_j) = \frac{\partial}{\partial x_j}[(\mu + \frac{\mu_t}{\sigma_\varepsilon})\frac{\partial \varepsilon}{\partial x_j}] + \rho C_1 S\varepsilon - \rho C_2 \frac{\varepsilon^2}{k + \sqrt{v\varepsilon}} + C_{1\varepsilon}\frac{\varepsilon}{k}C_{3\varepsilon}G_b + S_\varepsilon \quad (4.9)$$

Where,

$$C_1 = \max[0.43, \frac{\eta}{\eta+5}], \qquad \eta = S\frac{k}{\varepsilon} \qquad S = \sqrt{2S_{ij}S_{ij}}$$

4.5 Computational Set-up

Computational simulations are performed using the ANSYS Fluent 16 software assuming a steady, incompressible and isothermal flow.

4.5.1 Wind turbine rotor

The chosen horizontal axis wind turbine model is designed using the Blade Element Momentum Theory, as discussed in chapter 3. The wind turbine radius is 250 mm, hub radius 30 mm, the number of blades three. The design wind speed is 8 m/s, as the maximum amount of wind power can be extracted by adding winglets at the blades only if the wind speed is greater than 6 m/s [24].

4.5.2 Computational domain and boundary conditions

A computational domain is required for 3D CFD analysis. The CFD analysis is done to determine the torque generated due to the flow driving around the wind turbine blade with and without winglets. The calculated torque is used to find out the power output with the following equation:

$$P = T\omega B \qquad (4.10)$$

A simplified three-dimensional domain with the three blades rotor model is considered for simulations. The computational domain required for the analysis is shown in Fig. 4.1 with the necessary boundary conditions. The boundary conditions are very crucial for accurate simulation results. A velocity inlet boundary condition is applied at the

inlet section of the domain, which is situated at the 5R upstream (equal to 1.25 m ahead of the blade origin). A pressure outlet boundary condition is implemented at the outlet section of the domain, situated at the 10R downstream (equal to 2.5 m). Moving wall motion is applied to the turbine blades keeping the rotation of motion at the center. The blade and hub surfaces are considered as walls with no-slip boundary conditions. The following boundary conditions are used in the model shown in Table 4.1.
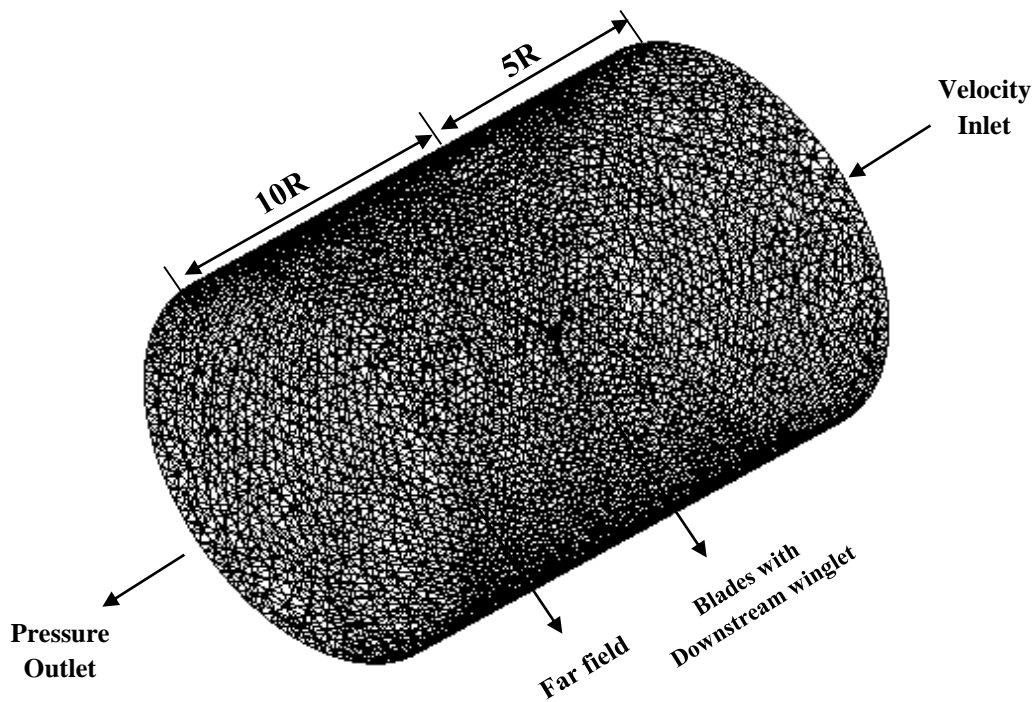
Fig. 4.1 Meshing domain with boundary conditions

Table. 4.1 Boundary conditions

Boundary	Conditions
Inlet, Far-Field	Velocity inlet (Velocity Magnitude 8 m/s) Turbulent Intensity = 5% Turbulent Viscosity Ratio =10
Outlet	Pressure Outlet
Blades	Wall Wall Motion- 'Moving Wall' Frame Motion – 'Rotational (Clockwise)' Speed- 'Angular Velocity (rad/s)'

4.5.2 Wind turbine blades with winglets

Many wind turbine sites have numerous restrictions, such as rotor diameter limitations, available wind speed, etc. Now, to overcome these restrictions and maximize the turbine performance (power coefficient), winglets are added at the wind turbines' tip. The incorporation of winglets at the blades will increase the power production without increasing the projected area of the turbine rotor. This is done by moving the blade tip's vortex away from the rotor blade plane, thus reducing the downwash effect, leading to the induced drag's decrement.

Two configurations, i.e., upstream winglets and downstream winglets with the same thickness, are designed and simulated before the models' fabrication. The analysis is done depending on the increment of power and thrust coefficients compared to the base model without winglets.

Winglet parameters like radius of curvature, height, twist angle, toe angle, CANT angle are required while designing the winglets. These parameters are selected (Table 4.2) based on some literature study. cant angle and twist angle is selected based on some computational study which will be discussed in the later section.

Table. 4.2 Design parameters of the winglets

Direction	Planform	Root Chord Ratio ($\dfrac{C_{Bla\,det\,ip}}{C_{Winglet\,roo}}$)	Tip Chord (mm)	Cant (°)	Height (%R)	Twist (°)	Sweep (°)	Toe (°)	Blade Profile
Upstream	Rectangular with taper	1	3.4	55	6	0	2	0	CABS
Downstream	Rectangular with taper	1	3.4	55	6	0	2	0	CABS

4.5.3 Mesh generation

The solution of the CFD profoundly depends on mesh creation. The meshes involved in computational simulations are commonly divided into two categories: structured and unstructured meshes. As unstructured meshes provide better conformity to complex geometries and less computational memory required than structured meshes [55], unstructured meshes are adopted for this particular analysis. The whole domain is discretized into several elements or grid cells and unstructured mesh is generated having approximately tetrahedron grids of 4, 30,545 and 85,442 nodes. The minimum cell size is 7.5×10^{-3} m. Figure 4.2 shows the mesh generated for the wind turbine blade. To solve the partial differential equations near the viscous sub-layer, the first grid cell's distance from the centroid to the blade or winglet wall is adjusted with y+ less than 2.The normal distance between the first layer call nodal point to the nearest wall is about 6.96 x 10^{-5} m.

<table>
<tr><td>(a)</td><td>(b)</td></tr>
</table>
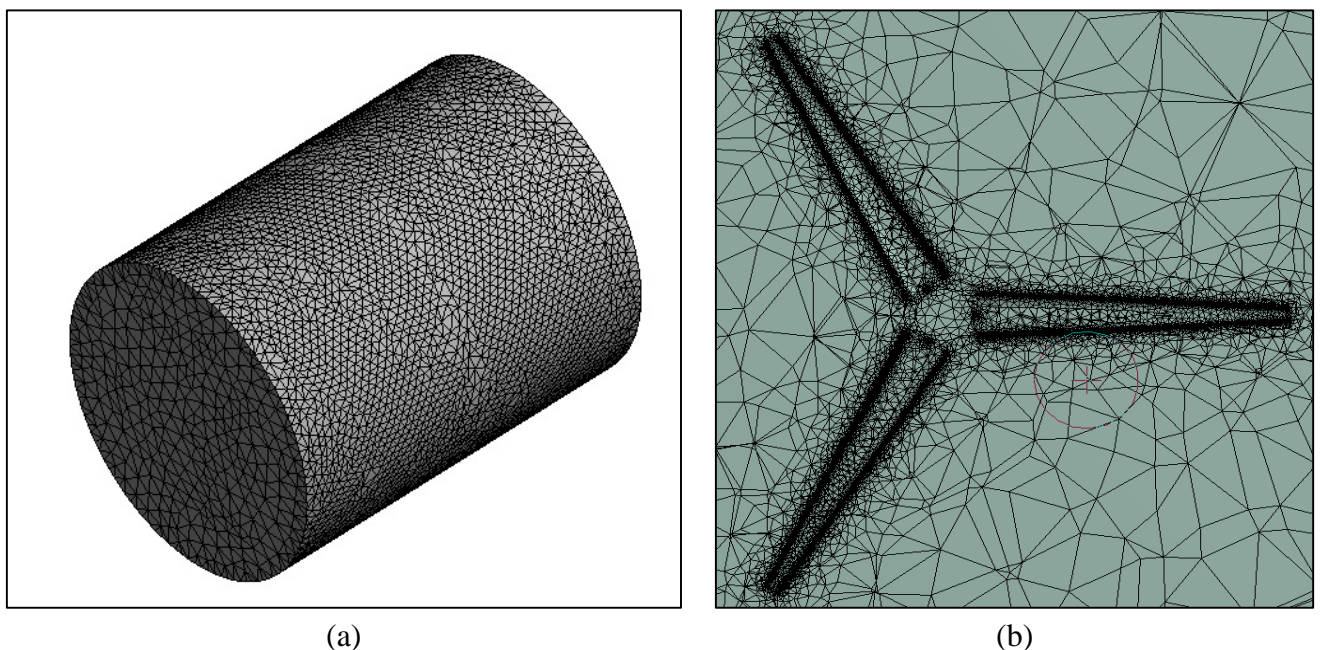
Fig. 4.2 a) Meshing view b) Close view of meshing around the blades

4.6 Mesh Sensitivity Test

A Grid-independency test is performed to validate the computational results for all the simulation of wind turbine blades. The power coefficient is selected as the factor of

judgment of the mesh validation test. To ensure the solution's independence, a computational analysis is done for a wide range of grid cells (i.e., from 1, 00,000 to 6, 00,000) at TIP=5 and $\phi=0^o$. Figure 4.3 describes the results of the power coefficient vs. mesh size. The figure shows that the power coefficient values decrease from the initial point (Grid cell no. 100,000) up to 4 30,000 cells and then asymptotically constant after that point.

4.7 Effects of CANT and Twist angle in Winglets

CANT angle and twist angle are one of the crucial criteria for evaluating the wind turbine effectiveness. Before the experimental study, computational analysis is done with four different cant and twist angles to observe which configuration provided the best performance. Figure 4.4 shows that cant angle=55^0 and Twist angle =0^0 indicated by thick solid line has the most significant effect on this particular CABS blades profile. These parameters are used for both the downstream and upstream winglets.
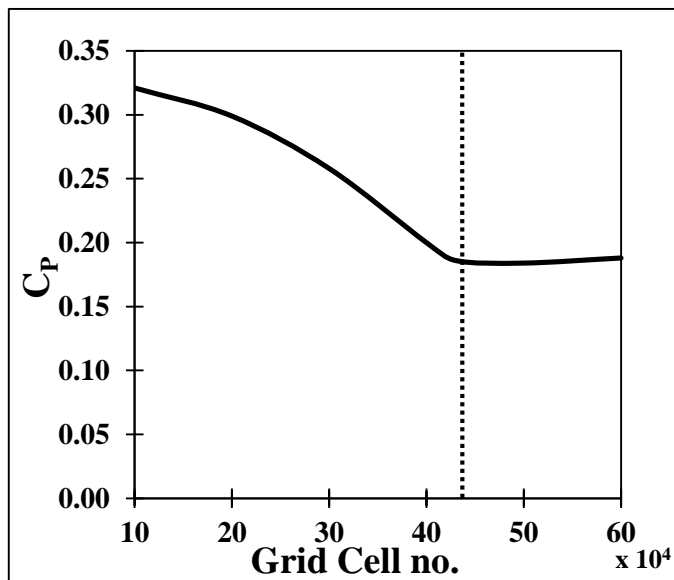
Fig. 4.3 Wind turbine model grid-independency test
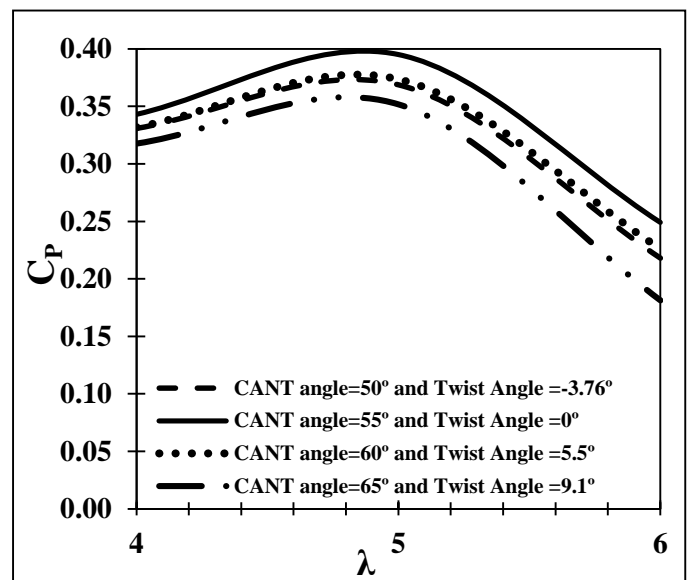
Fig. 4.4 Comparison of cant and twist Angles on power co-efficient having CABS profile

CHAPTER 5

DESIGN OF WIND TURBINE AND BLADE WINGLETS

5.1 General

A wind turbine for a particular region, maximum velocity is less than 10 m/s. To extract a reasonable amount of power, the wind velocity must be sufficiently high, preferably more than 6.0 m/s. As the wind power changes with the cube of wind velocity, and hence the wind velocity plays a paramount role in the production of power.

Constructing a wind turbine blade with NACA airfoil is slightly complicated. Thus, the design has been taken into consideration with a simple type of circular arc blade section (CABS) and small power production at the available wind speed. At lower tip speed ratio (TSR), the power coefficient of turbine having CABS was higher than that of having NACA 4418 profile [21] as shown in Fig. 5.1. However, at higher tip speed ratio range NACA 4418 profile had higher power coefficient.
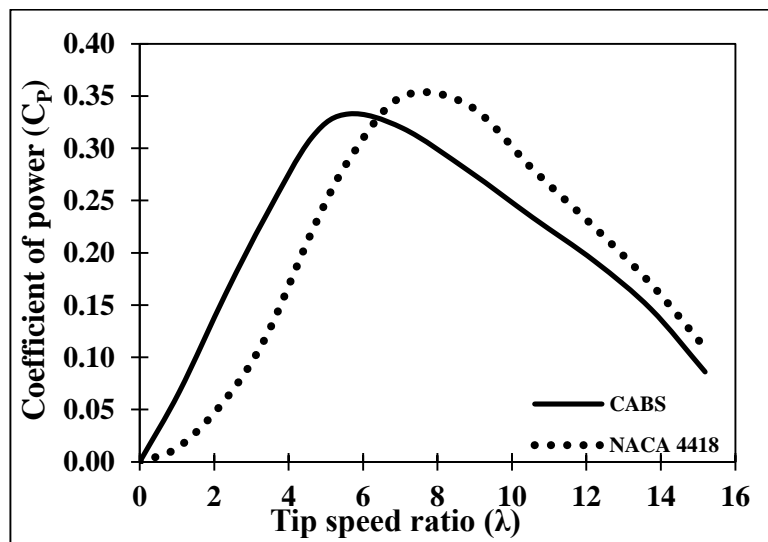
Fig. 5.1 Comparison of power coefficient for three blades (without winglets)

Furthermore, winglets will be attached at the tip of the blade to compensate for power loss due to the vortices in that region. This will help to extract more energy in lower wind flow. The tip-vanes are designed and then fabricated depending on some of the existing literature.

The procedures for designing the horizontal axis wind turbine are comprised of two steps:

a) The initial parameters are required to be chosen, for example, the number of blades B, the radius of the rotor R (will be calculated from the required power and available wind velocity of the location), type of blade section and design tip speed ratio λ_d

b) The following process is to calculate the blade twist angle β and the chord C at several positions along the blade. The conventional design uses the maximum lift to drag ratio for measuring the aerodynamic efficiency of the blades. Still, due to avoiding the stalling range, the lift coefficient corresponds to 90% of the maximum lift coefficient that will be used. Adding that, there is a close relationship between the numbers of blade and design tip speed ratio, which will also counter by a simple empirical equation.

5.2 Selection of Design Parameters

Regarding the selection of the different design parameters, namely, the number of blades, design tip speed ratio, and twist angle, are need to be evaluated. The initial problem is to choose the appropriate number of blades of the wind turbine. As the number of blades increases, the power generation increases, but it does not have a linear effect. In multi-bladed wind turbine machines, the rotor speed and efficiency decrease considerably, while the cost of power production rises. Considering this situation, it might be mentioned that a finite number of blades instead of an ideal infinite blade number causes an extra reduction in power, particularly at a low tip speed ratio. This is caused by the losses around the tip of the blade. To design a rotor for a particular tip speed ratio, one can choose between many blades with a small chord width or lower number of blades with a large chord width keeping the solidity the same. It is then clear that for a given tip speed ratio, a rotor with lower blades will have more substantial tip losses and vice versa.

The tip speed ratio contributes to increasing the power output and efficiency of a wind turbine. There is a correlation between the selection of the design tip speed ratio and

the number of blades. If the value of the design tip speed ratio is low, a higher number of blades should be considered. Because, for a higher number of blades, the power coefficient's peak is shifted towards the lower tip speed ratio side as the solidity of the turbine increases. On the other hand, for the higher value of the design tip speed ratio, a lower number of blades should be chosen. When the blades of the wind turbine become lower, the solidity of the turbine becomes low, if identical blades are used; as a result, peak power moves towards the higher tip speed side.

.   The design tip speed ratio also depends on which type of turbine is being used. If used for slow running equipment such as a piston pump, which requires a high starting torque, then the rotor's design tip speed ratio will be low. If the turbine is used for the fast running equipment for instance, an electric generator or a centrifugal pump, a high design tip speed will be necessary. The table mentioned below (table 5.1) should be considered as the guidelines for the design tip speed ratio and the corresponding number of blades as per Lysen [52]. In this current study, selecting the design tip speed ratio for the HAWT with circular arc blade section, an empirical relation is presented as function of number of blades (B) as mentioned below:

$$\lambda_d = 12 - (8B)^{\frac{1}{2}} \qquad \text{for } 1<B<15 \qquad (5.1)$$

The calculated value should be made a round number before using it. Fig. 5.2 illustrates how the design tip speed ratio changed with the number of blades and proposed by the Lysen [52] for comparison. The figure described that with the increase of tip-speed ratio, blade number decreases. Author studied conventional NACA airfoils and investigated coefficient of power vs. tip speed ratio relations depending on various numbers of blades. But, the design tip speed ratio suggested by Lysen sometimes provides an unstable region of the power generation. Thus, to avoid the phenomenon, the empirical relation established above has been chosen in this present study.

Table. 5.1 Relation between design tip speed ratio and number of blades [52]

Design Tip Speed Ratio, λ_d	Number of Blades, B
1	6-20
2	4-12
3	3-6
4	2-4
5-8	2-3
8-15	1-2

Further, author mentioned that for conventional blade airfoil for instance NACA 4418, the design tip speed ratio becomes slightly larger than that for the circular arc blade section to operate the wind turbine in the stable region.
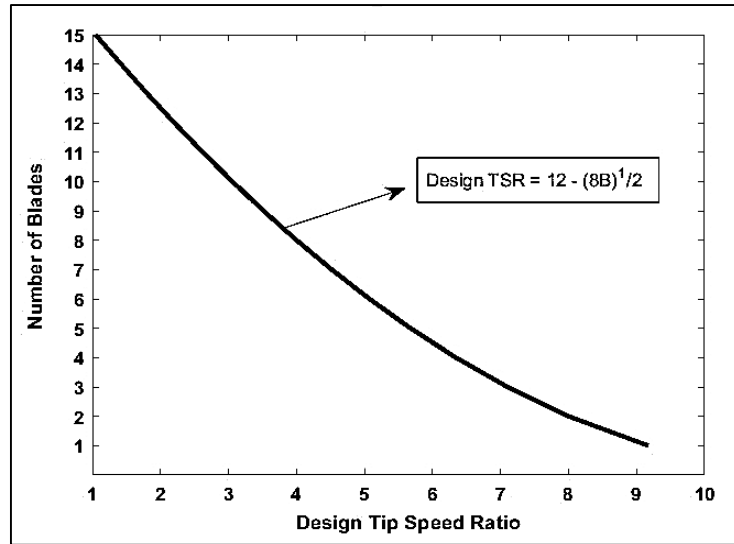
Fig. 5.2 Design tip speed ratio vs. number of blades

The following equations are used to determine the blade configurations:

Local tip speed ratio 　　　　　:　　$\lambda_r = \lambda_d \dfrac{r}{R}$

Angle of relative wind velocity 　:　　$\phi = \dfrac{2}{3}\tan^{-1}[\dfrac{1}{\lambda_r}]$

Twist angle 　　　　　　　　　:　　$\beta = \phi - \alpha$

Chord 　　　　　　　　　　　 :　　$C = \dfrac{8\pi r(1 - \cos\phi)}{BC_{Ld}}$

In the present research activity, the prototype is designed by choosing the design tip speed ratio from equation (5.1) for the number of blades 3 and design tip speed ratio is

chosen as 5. This will also be kept the same when winglets are incorporated at blades tip to make a comparative study between the experimental results as well as theoretical and computational results with and without winglets. Twist angle is a vital parameter while designing the turbine blades or aircraft's wing, as lift and drag coefficients widely depend on it. The twist angle may be taken as zero, linear or the optimum one. In this current research, the linear twist angle is selected. Constructing a blade with an optimum twist is very expensive and complicated, while the performance of the linear twist blade does not deviate much compared to that with the optimum twist blade [56]. Meanwhile, there is no justification for constructing the blade with zero-twist angle since it produces substantially lower power.

5.3 Blade Selection

The aerodynamic efficiency or the lift to drag ratio has a paramount impact on the effectiveness of a rotor that has been used in the wind energy conversion. Considering the fluctuations which are prominent in wind speed and, therefore, in the angle of attack, airfoils having a higher lift to drag ratio should be chosen for a relatively broad range of values. From this point of view, though the circular arc blade section is not quite perfect, due to its simplicity in construction, fabrication and cost encouraged us to select this as the blade section. Pandey et al. [14] carried out some experimental tests in wind turbines on circular arc steel plates. The camberness ratio varied from 0 to 14% to measure their lift and drag coefficients. The experimental analysis conducted at Reynolds number 2.23×10^5 and the angle of attack varied from -20° to 90°. For different camberness ratios (ratio between the maximum chambers of the blade section to the chord) ranging from 0.00 to 0.14, the lift to drag characteristics were studied. They found that for camberness ratios of 0.08 and 0.10, lift-drag features gave the most preferred results. Based on these results, the camberness ratio of 0.08 has been nominated for this present study. For the design and

analysis of wind turbines, lift and drag coefficient has been used from Pandey et al. [14].

The design lift coefficient, C_{Ld} is taken as $C_{Ld} = 0.9\ C_{Lmax}$ where, C_{Lmax} = maximum lift coefficient value in C_L vs. α graph shown in Fig. 5.3 and design angle of attack, α_d is found the corresponding value of C_{Ld}.
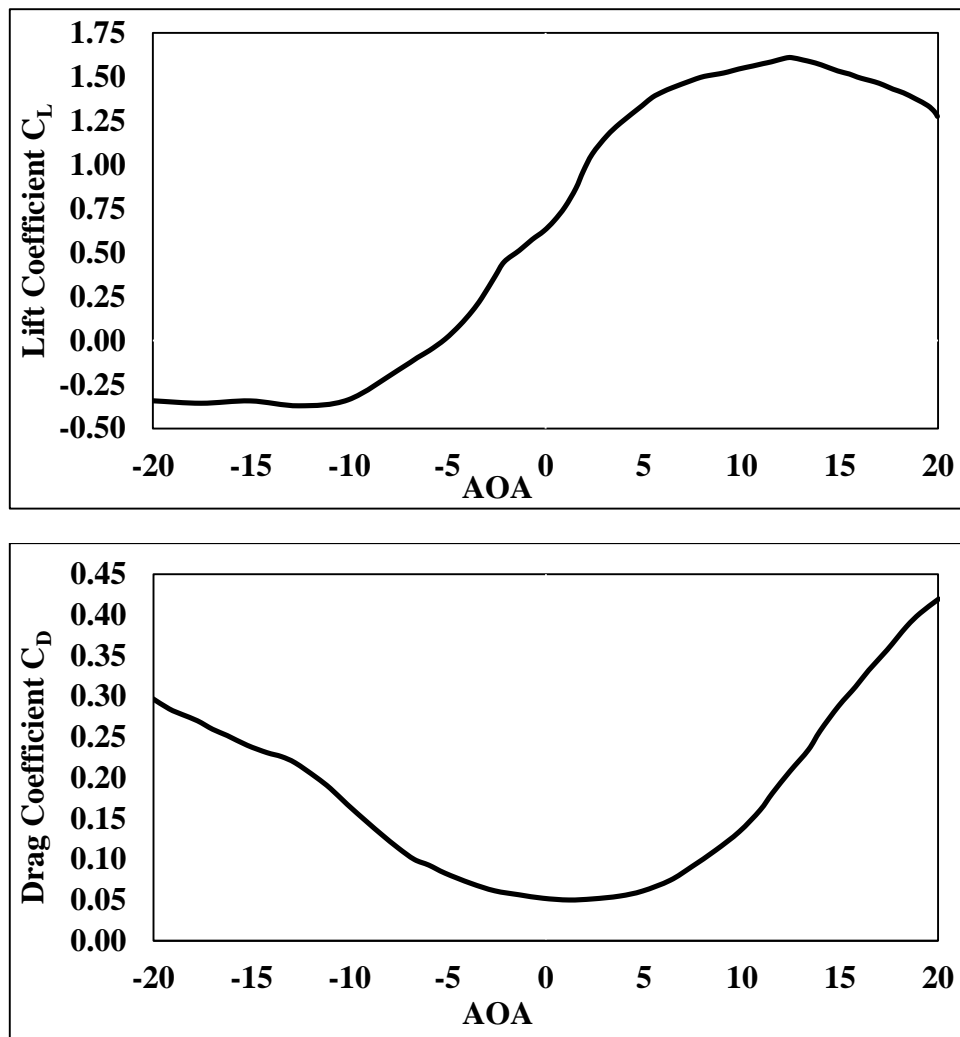
Fig. 5.3 Lift and drag coefficent graphs of circular arc blade section [14]

5.4 Design Procedures for Blade Configuration

Prior to the calculation of blade profile the following data should be available:

$$\text{Design tip speed ratio} \quad : \lambda_d$$

$$\text{The rotor radius} \quad\quad : R$$

$$\text{Design wind velocity} \quad : V_d$$

$$\text{Number of blades} \quad\quad : B$$

Calculation Steps:

a) A certain number of radial segments is chosen for which the blade chord and blade twists angles are to be calculated.

b) From the C_L versus α curve the value of C_{Lmox} is pointed out. Then the value of design lift coefficient $C_{Ld}=0.9C_{Lmax}$ is calculated. Corresponding to C_{Ld}, the value of the design angle of attack, α_d is obtained.

c) The number of blades B is selected corresponding to the chosen design tip speed ratio

d) A fixed value of hub and rotor radius ratio, r_{hub}/R is chosen

e) Calculation of local tip speed ratio λ_r for each radial segment is performed using the equation $\lambda_r = \lambda_d \dfrac{r}{R}$.

f) The flow angle ϕ determined using the equation $\phi = \dfrac{2}{3}\tan^{-1}[\dfrac{1}{\lambda_r}]$.

g) The value of blade twist calculated using the equation $\beta = \phi - \alpha_d$.

h) The chord of the blade C, for each radial segment is calculated using the equation $C = \dfrac{8\pi r(1-\cos\phi)}{BC_{LD}}$.

i) Finally, the value of camber 'f' is obtained from the equation $f/C = 0.08$.

The typical feature of the blade is shown in Fig. 5.4(a), which is a taper in shape. The root and tip chord length will mention in the next section. The cross-section of the blade in enlarged condition shown in Fig. 5.4(b) to mention the camber and chord length. Additionally, a cross section of NACA 4418 airfoil is shown in Fig. 5.4 (c) to compare with the CABS profile.

(a)

(b)

(c)
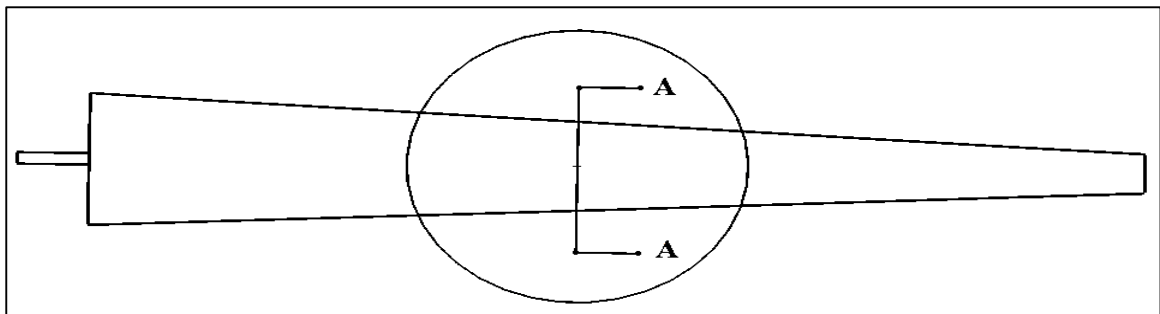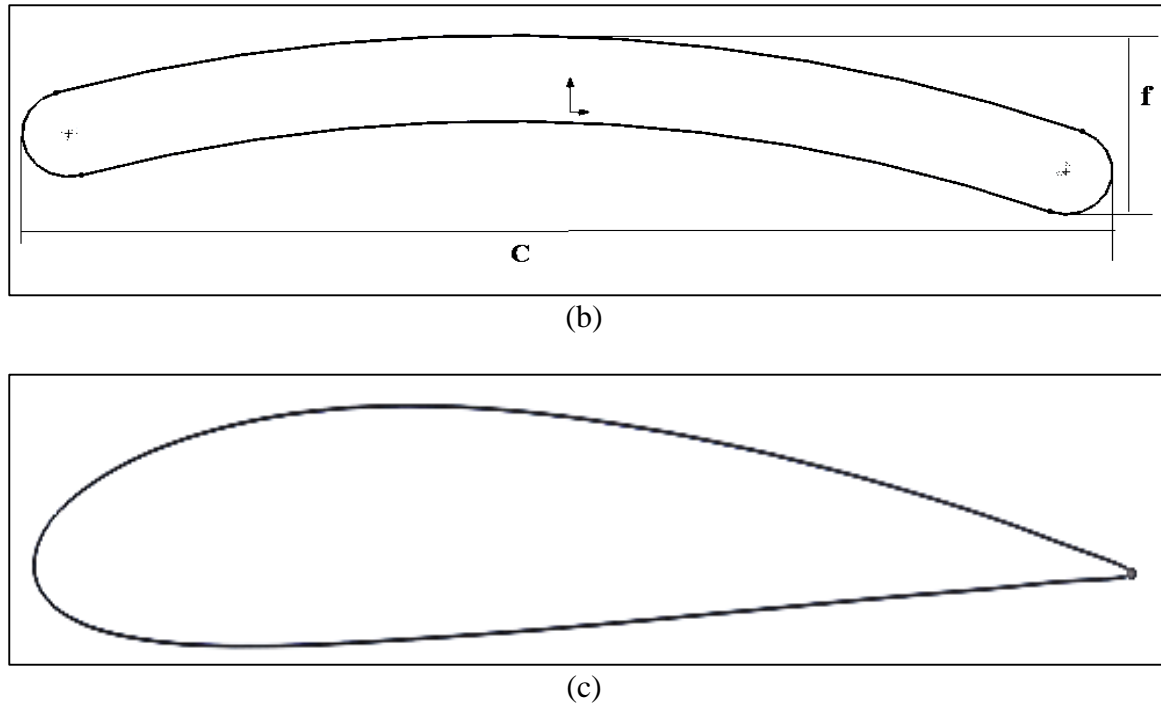
Fig. 5.4 (a) Typical features of the blade (b) Enlarged section A-A (c) NACA 4418 airfoil cross section

5.5 Derivations from the Ideal Blade form:

In an ideal blade profile, the blade twist angles and blade chord lengths vary in a non-linear way throughout the blade length. Hence, it is challenging to fabricate these types of blades and also suffer from structural integrity. To ameliorate these effects, it is suggested to linearize the blade profiles i.e., blade twist angles and blade chord. Despite having a small loss in power generation, it can overcome through better linearization.

In a linear blade, it is thought that the majority of the power of almost 75% is generated by the outermost part of the blade between r/R = 0.5 to r/R = 0.9. The blade swept area changes with the square of the radius, and the efficiency of the blades is less where the tip speed ratio λ_r is small. Meanwhile, at the tip of the blade, efficiency is also low due to the tip loss. Thus, it is advisable to linearize the blade twist angles and blade chord between r/R = 0.5 to r/R = 0.9, as mentioned by Jansen [57].

The equations for linearized chord and twist can be written as below:

$$C = C_1r + C_2 \qquad\qquad (5.2)$$

$$\beta = C_3r + C_4 \qquad\qquad (5.3)$$

Where, the terms C_1, C_2, C_3 and C_4 are the constants. From the ideal blade form, the values of C and β at r/R = 0.5 and r/R = 0.9 are calculated and then the values of these constants are determined. Thus, the final expressions for chord and twist of a linearized blade can be given by according to MandaI and Islam [58],

$$C = 2.5 (C_{90} - C_{50}) \text{ r/R} +2.25 C_{50} - 1.25 C_{90} \qquad\qquad (5.4)$$

$$\beta = 2.5 (\beta_{90} - \beta_{50}) \text{ r/R} +2.25 \beta_{50} - 1.25 \beta_{90} \qquad\qquad (5.5)$$

The ideal blade form is linearized using the equations (5.2), (5.3), (5.4), and (5.5), as shown in Table 5.2. Fig. 5.5 and Fig. 5.6 represent the distribution of blade chord and blade twist angles. From these figures, it is found that the changes in chords and twist angles are quite low at the outer half of the blade (r/R=0.5 to r/R-=1). However, a substantial amount of variations with the linear chord and twist angle distributions are found only at the smaller radius of the blade (up to r/R= 0.4). Figure 5.7 represents the turbine blades. The design parameters for the prototype wind turbine with number of blades 3 are as follows:

Blade airfoil type	: Circular arc with f/C = 0.08
Rotor radius	: 250mm
Root chord length	: 33mm
Tip chord length	: 8.4 mm
Root twist angle	: 7.4°
Tip twist angle	: -3.5°
Hub radius	: 30 mm (12% of rotor Radius)

Table. 5.2 Linearized blade chord and blade twist angle with local tip speed ratio.

Cross Section No.	Rotor radius, r (mm)	Design Tip speed ratio (λ_d)	Design AOA, α_d	Twist Angle, β (deg)	Chord length, C(mm)	Camberness ratio, f=0.08C
1	25	0.6	7	7.40	33.0	2.64
2	50	1.2	7	6.20	30.0	2.40
3	75	1.8	7	4.90	27.4	2.19
4	100	2.4	7	3.70	24.5	1.96
5	125	3.0	7	2.35	22.0	1.76
6	150	3.6	7	1.30	19.1	1.53
7	175	4.2	7	0	16.4	1.31
8	200	4.8	7	-1.30	13.7	1.10
9	225	5.4	7	-2.50	11.0	0.88
10	250	6.0	7	-3.50	8.4	0.67
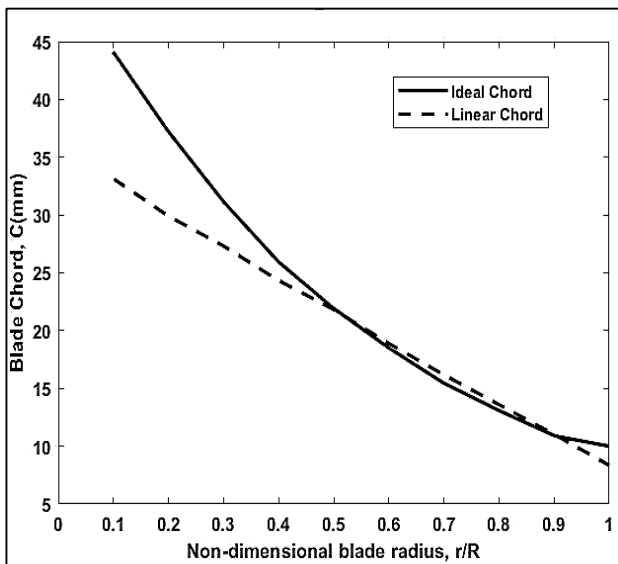
Fig. 5.5 Blade chord distribution
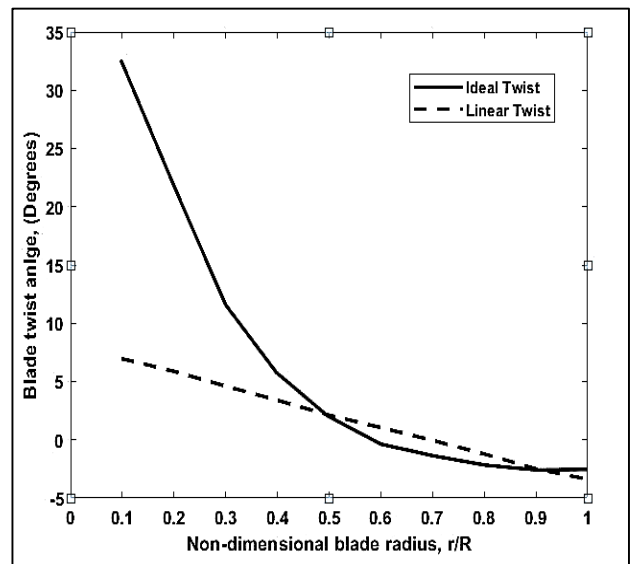
Fig. 5.6 Blade twist distribution
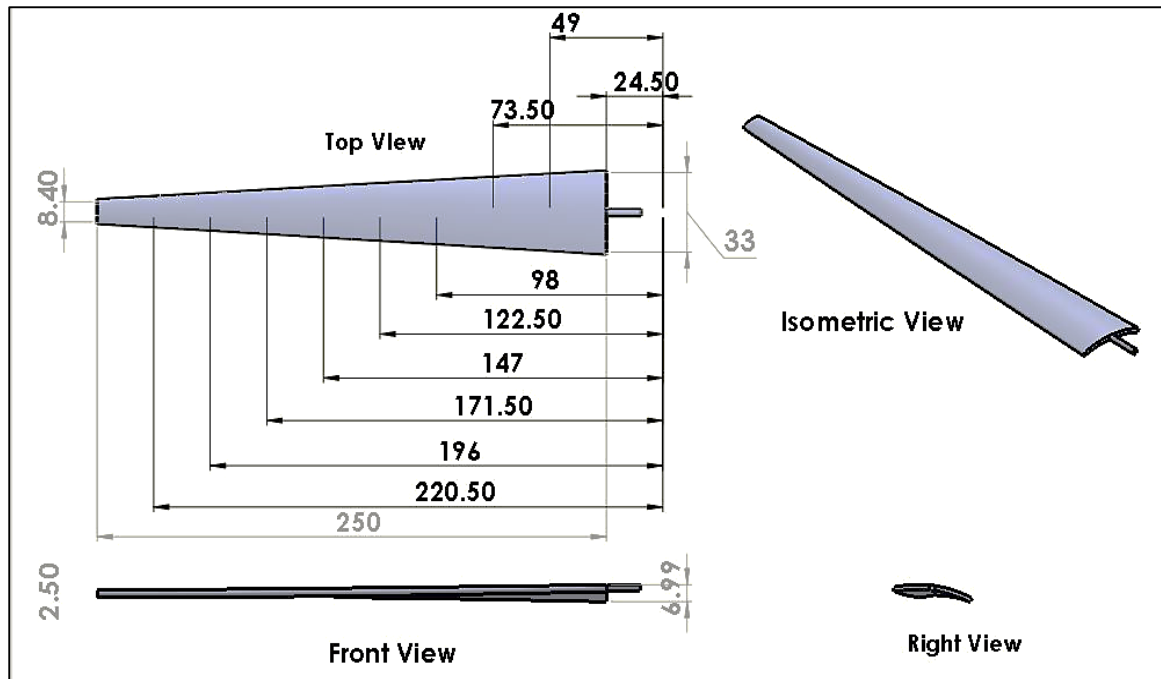
(a)

(b)

Fig. 5.7 Wind Turbine Blades (a) Different view with dimensions (b) After fabrication of the blades

5.6 Procedures of Performance Calculation

To calculate the performance characteristics of that particular design, the parameters which are required to be chosen beforehand:

     Design wind velocity   : V_d

     Chord of the blade   : C

$$\text{Rotor radius} \quad\quad\quad : R$$

$$\text{Number of blades} \quad\quad : B$$

$$\text{Design tip speed ratio} \quad : \lambda_d$$

The chronological process followed to calculate the performance characteristics of the wind turbine, are described below:

a) At first, the local solidity ratio σ_r, is determined from equation (3.40).

b) A certain number of radial segments are predicted for blade twist angles determination.

c) The value of λ_r, is obtained for each radial segment using equation (3.22).

d) From the C_L versus α graph the maximum value of C_L is determined for $f/C = 0.08$ and the design value of C_L is chosen as $C_{Ld} = 0.9\, C_{Lmax}$

e) In the design analysis the linear value of β is considered. To find the values of "a" and "a'", the following iteration process is performed.

    i. Initial values of λ, β and "a" are assumed as 2, 4° and 0.9 respectively.

    ii. λ_r is calculated.

    iii. The value of a' from equation (3.28) is calculated.

    iv. ϕ From equation (3.38) is calculated.

    v. α is obtained from equation (3.39).

    vi. Corresponding to α as obtained above, the values of C_L and C_D are determined by linear interpolation.

    vii. Finally "a" from equation (3.43) is found.

    viii. Using the value of "a", β is determined.

    ix. The above calculation procedure for each radial segment is repeated.

f) Calculation of C_p:

    i. Using the above iteration process from steps (i) to (vii) values of "a" and "a" for each radial segment are found.

ii.   The value of C_p is obtained by numerical integration from equation (3.61) using Simpson's rule.

5. 7 Design of Prototype Turbine:

For designing the prototype wind turbines for 3 blades the design tip speed ratios are chosen from equation 5.1, enlisted in table 5.3.

Table. 5.3 Design tip speed ratio for prototype turbine

B	λ_d
2	8
3	7
4	6
6	5

While designing the wind turbines, the outcomes i.e., power production capacity is generally presumed. In this case, the prototype is designed for power generation capability of 1KW, 2 KW, 3 KW, and 4KW at the design wind speed of 8m/s. Figure 5.8 represents a comparison between rotor diameters vs. wind velocity for different power production for three blade turbine. It can be observed that power production capacity increases with rotor diameter increases due to reason as power is directly proportional to the cube of the wind velocity.
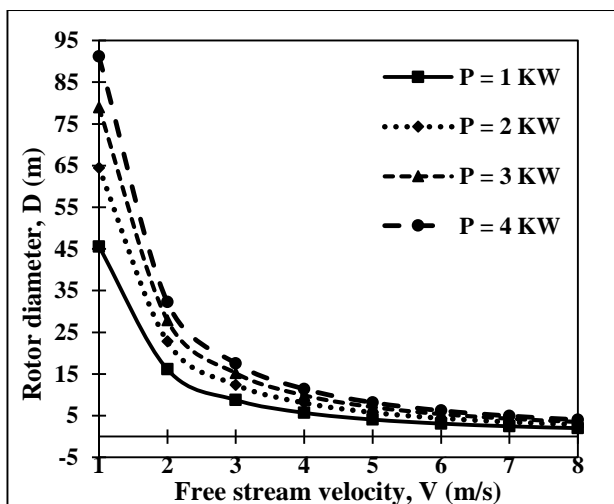
Fig. 5.8 Rotor diameter vs. Wind speed for B=3
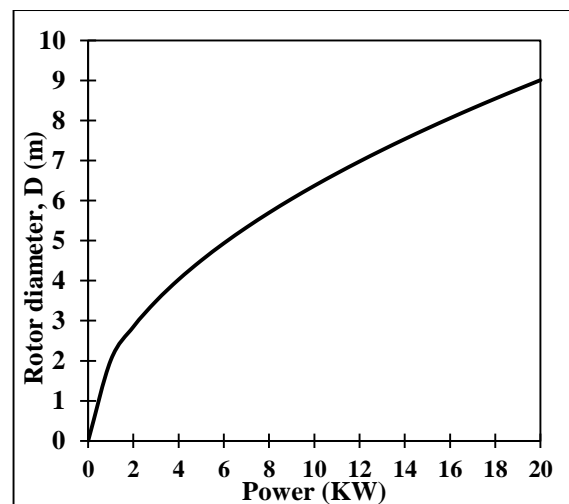
Fig. 5.9 Rotor diameter vs. Power output at design wind speed (8 m/s)

Figure 5.9 describes that as the rotor diameter increases the output power generation also increases at a design wind velocity 8m/s. Figure 5.10 illustrates the comparison of the rotor diameters with the circular arc blade profile and the conventional NACA 4418 blade profile at different wind velocities for producing 5kW when three blades are used. It can be seen that using a circular arc blade section (CABS) instead of the conventional NACA 4418 blade section, the rotor diameter increased appreciably for the same amount of power production.
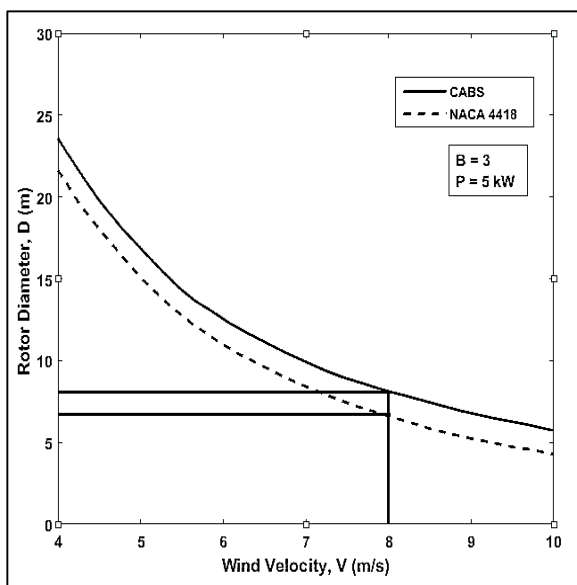
Fig. 5.10 Comparison of rotor diameter   **Fig. 5.11** Effect of winglets at the tip
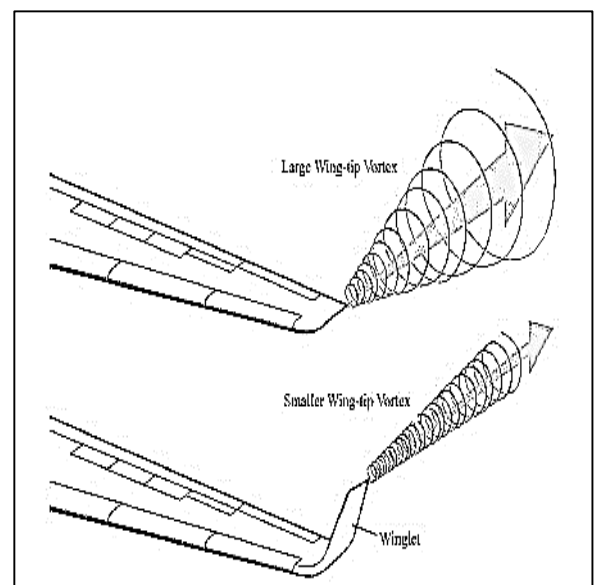
5.8 Design of Tip-vanes (Winglet)

5.8.1 Effect of winglets:

Winglets are incorporated at the tip of wind turbine blades or aircraft's wing to enhance the performance more exactly efficiency by reducing the tip vortices and downwash effect without increasing the plan form area (Fig. 5.11). This is done by moving the vortices from the pressure side of the surface, which reduces the induced drag, thus, in turn, increasing the lift production capability [59]. Additionally, winglets transform some of the waste energy to some sort of perceptible thrust.

Winglets are exclusively used in the aerodynamic industry due to its significant impact on induced drag. The attachment of winglets in the aircraft's wing yielded of almost 7% enhancement in cruising speed [60]. Since it has been shown that winglets are probably useful to enhance the aerodynamic performance of wind turbine rotors, it is essential to design and incorporate wind turbines to increase power production. The design parameters considered while designing a winglet are length, height, sweep angle, cant angle, curvature radius, toe angle and twist angle as shown in Fig. 5.12 [40].These parameters are influenced mainly by:

a) Chord Distribution

b) Planform shapes i.e. rectangular, tapered, and elliptical

c) Airfoil

d) Location i.e. pressure or suction side of wing or rotary wing like wind turbine blades.
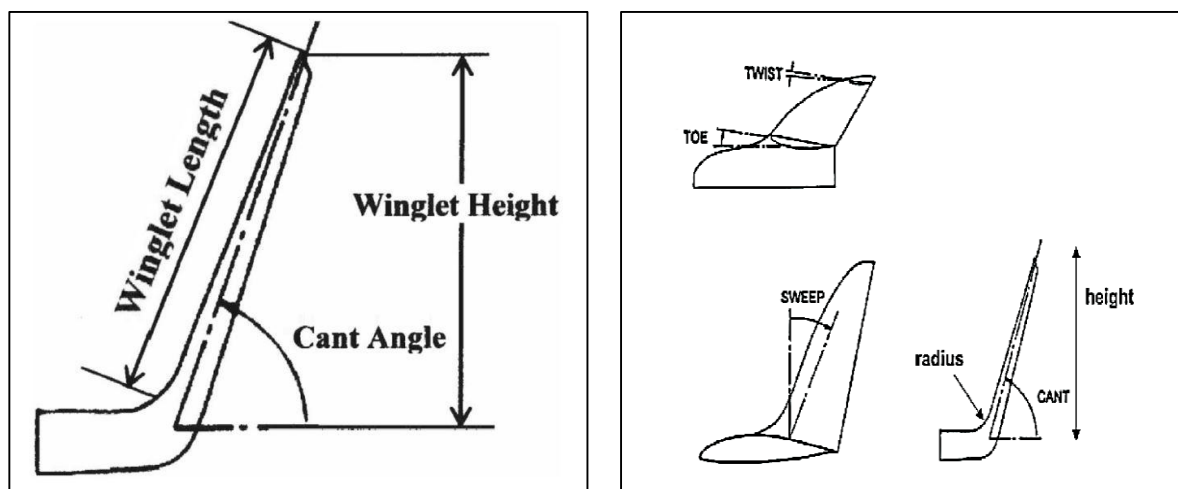
Fig. 5.12 Geometrical parameters of a winglet **[40]**

Location: Maughmer [23] mentioned that winglets' impact will be most effective if they are attached at the suction side of a wing by controlling the spanwise flow. This can also be incorporated in the pressure side, as observed by many researchers but may lead to contraction of the wake. In this study, both the effects of position namely upstream and downstream sides will be studied, while adding them with the wind turbine blades.

Chord Distribution: Elliptical lift distribution is paramount as it causes a constant downwash effect across the span of the wing. Thus, chord distribution is crucial while designing the winglet's loading capacity, and it needs to be elliptical. During the selection of chord distribution, it is required to look upon the span-wise loading distribution while interacting with the induced-velocity. This reduces tip losses, and increases the output power.

Height, root chord and tip chord: The selection of height, root chord, and tip chord is essential for the wetted-area and Reynolds number. Drag coefficients increase with decreasing Reynolds number (i.e. Chord length). However, a larger wetted area (dependent upon the chord distribution and height) increases the gross drag. Thus an optimal design needs to satisfy chord lengths and Reynolds number. Winglets, while under loaded with larger chords, led to some increase in wetted area and profile drag. By measuring the penalties of wetted area with the benefit of induced drag, winglet height is determined.

Twist, Sweep, and Toe Angle: After the finalization of chord distribution and winglet height, the load distribution is then tuned by span-wise sweep and twist. Sweep angle has a similar effect on load distribution as incorporating wash-in to the winglets. But, there is a problem if too much sweep angle is given, which causes cross flow instability and may lead to premature boundary layer transition.

After the selection of the winglet plan form, the toe angle has to be introduced. The toe angle controls the overall load distribution on the winglets, as it is the initial angle of attack at the root of the winglet. It is quite complicated for a particular toe angle that will work efficiently at all flow conditions regarding the wind machines. Meanwhile, when incorporating in one design point, it may perform in reverse at other operating conditions. Another critical design parameter is the twist angle and can be either positive or negative. Positive twist provides wash in, whereas a negative twist angle provides washout. Wash in

or out can be adjusted by varying the airfoil chord lengths. Washout decreases the angle of attack towards the winglet tip while washing in increases it. The combination of the twist and toe angle makes the setting angle. Figure 5.13 represents the setting of a particular section of a winglet is the rotation of the section concerning the tangent of the circle swept by the blade tip. This varies along with the winglet height based on the root toe and tip twist of the winglet. A positive toe angle increases the setting angle, while a positive twist decreases it.
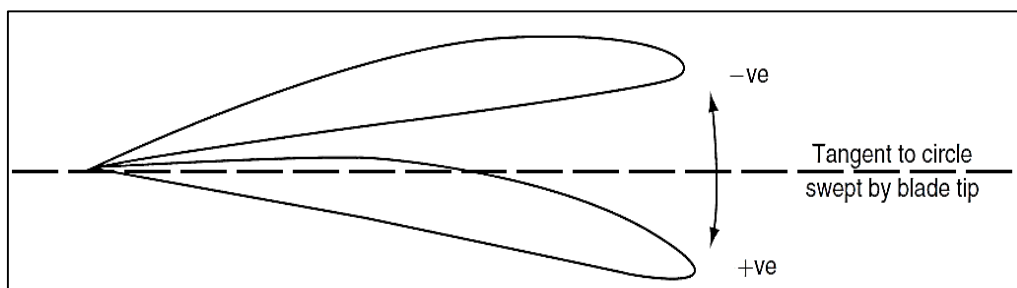
Fig. 5.13 Winglet setting [28]

5.8.2 Winglet design

There are numerous types of winglets; for instance, blended winglets, split winglets, fenced winglets, raked winglets, drooped winglets have been proposed and incorporated in the aircraft's wing. The overall influence of these winglet's geometrical parameters on different models has already been investigated. They concluded that most substantial settings are cant and sweep and the winglet height. Also, cant angle increases with the increase of winglet height [40], for this reason only two of the parameters are considered for this study. An admirable reduction can be gained while using large winglets with an additional profile drag and higher bending moment. Regarding the cant angles, higher angles may lead to rise aerodynamic interference and lead to more considerable wave drag. However, providing small bending moments and thus fewer weight penalties. In contrast, a low cant angle assists in more lift production.

Depending on theoretical observation and literature view the following parameters are considered:

a) Due to avoid the complexity of the manufacturing circular arc blade section (CABS) blade profile section is selected.

b) Winglet height is taken as 6% of rotor radius [41].

c) Sweep angle is given of about 2º

d) Cant angle is selected depending on some computational analysis, which discussed in the previous chapter.

e) Twist angle is selected depending on some computational analysis, which discussed in the previous chapter.

Cant and Twist angles are nominated as design parameters depending on the fabrication on the manufacturing process (Table 5.4).

<div align="center">Table 5.4 Design parameters of winglets</div>

Direction	Planform	Root Chord Ratio $(\dfrac{C_{Blade\,tip}}{C_{Winglet\,root}})$	Tip Chord (mm)	Cant (°)	Height (%R)	Twist (°)	Sweep (°)	Toe (°)	Blade Profile
Upstream	Rectangular with taper	1	3.4	55	6	0	2	0	CABS
Downstream	Rectangular with taper	1	3.4	55	6	0	2	0	CABS

It should be noted that winglet height will increase as the cant angle increases with two contradicting effects. Firstly, the performance of the turbine enhances due to the attachment of winglets. Secondly, an additional resisting drag force is there because of the higher length of winglets. Hence, it is sometimes challenging to investigate both the parameters (height and cant angle). Thus, the cant angle effect is considered for overall comparison,

and height is kept constant for both the configuration. Figure 5.14 and 5.15 show the turbine blades with downstream and upstream winglets respectively.
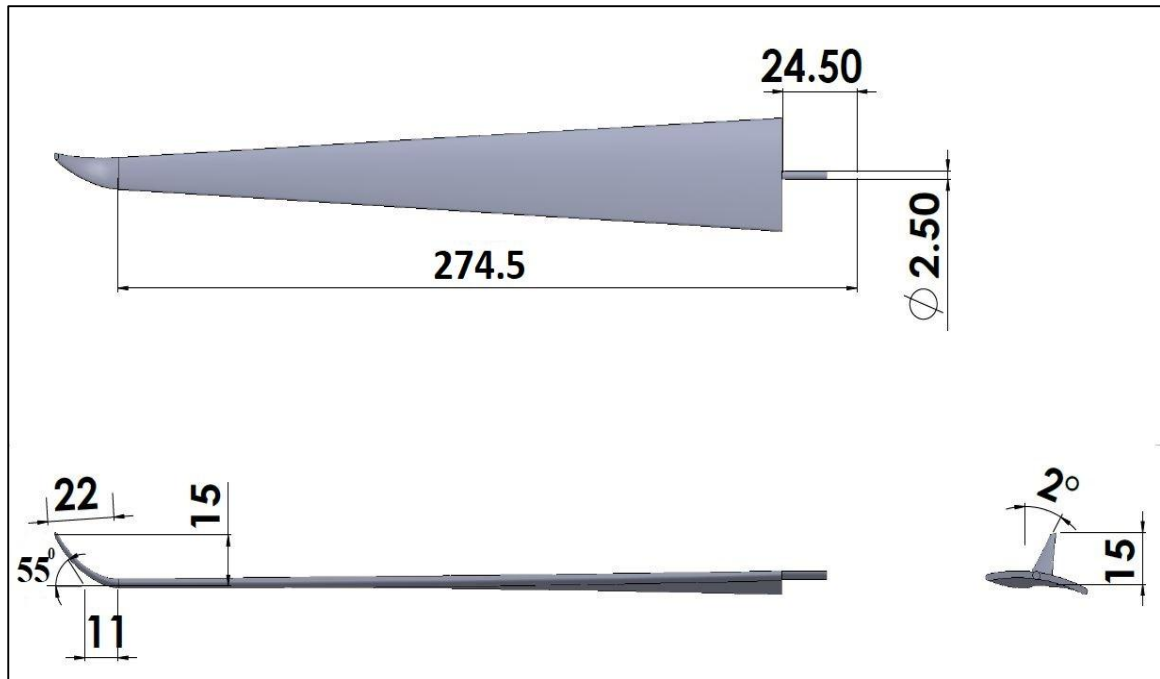
(a)
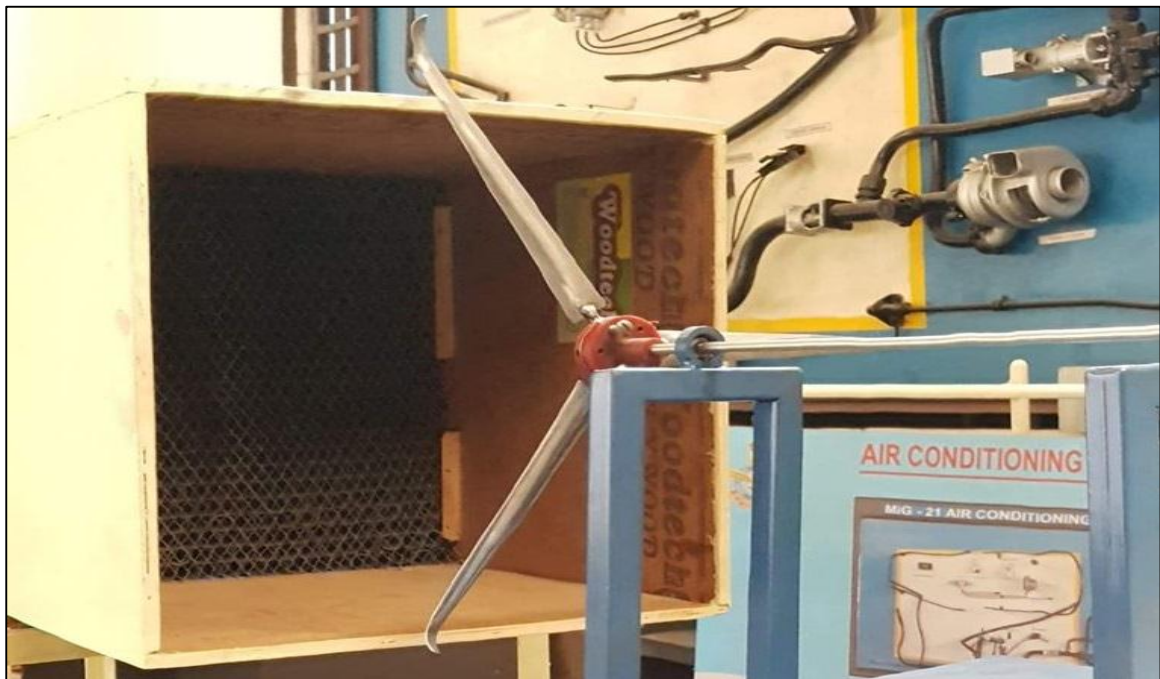
(b)

Fig. 5.14 Blade with winglet (Downstream) a) Different view with dimensions b) After fabrication of the blades.
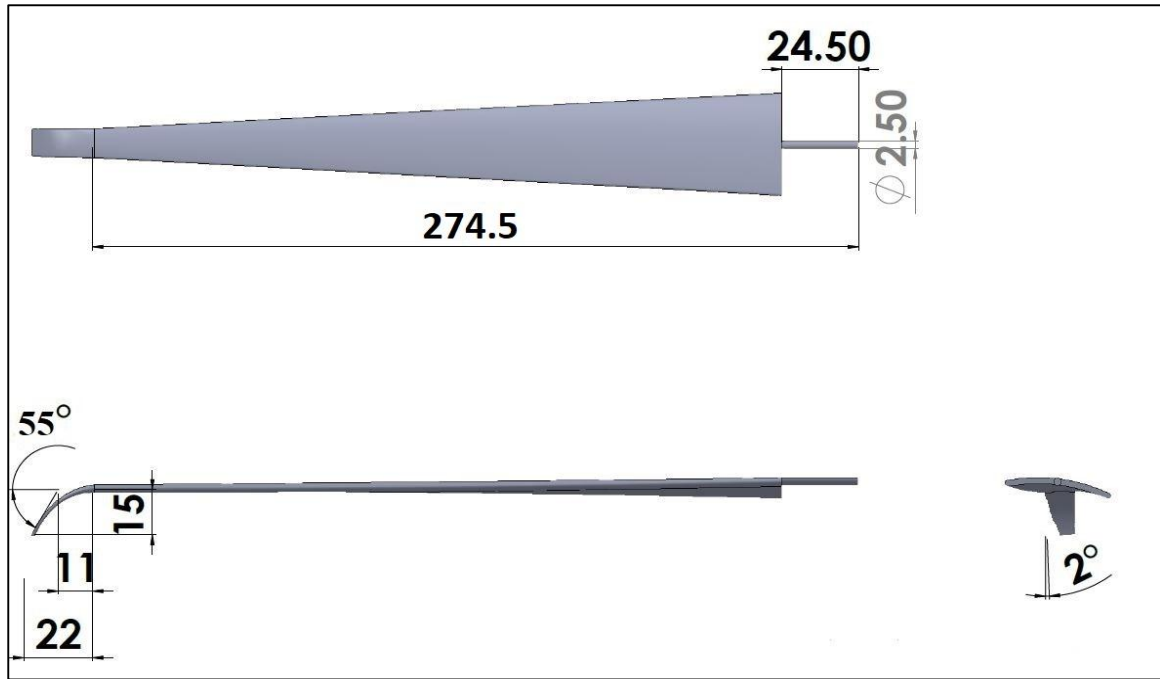
(a)

(b)

Fig. 5.15 Blade with winglet (Upstream) a) Different view with dimensions b) After fabrication of the blades

CHAPTER 6

EXPERIMENTAL SET-UP

6.1 General

The experimental set-up which is used to determine the performance characteristics of the wind turbine, is described in this section. The wind turbine model is tested by placing it at the discharge of the wind tunnel. As the model is placed at the downstream side, no blockage effect is there.

6.2 Wind tunnel

A low subsonic open type wind tunnel (Model AF1300s of TQ Equipment, U.K.) facility in the Aeronautical Engineering Department, MIST, is used for this experimental study. The maximum velocity of this wind tunnel is 36 m/s (M=0.1) and the CAD model of that wind tunnel is shown below in the Fig. 6.1 and pictorial view in Fig. 6.2.
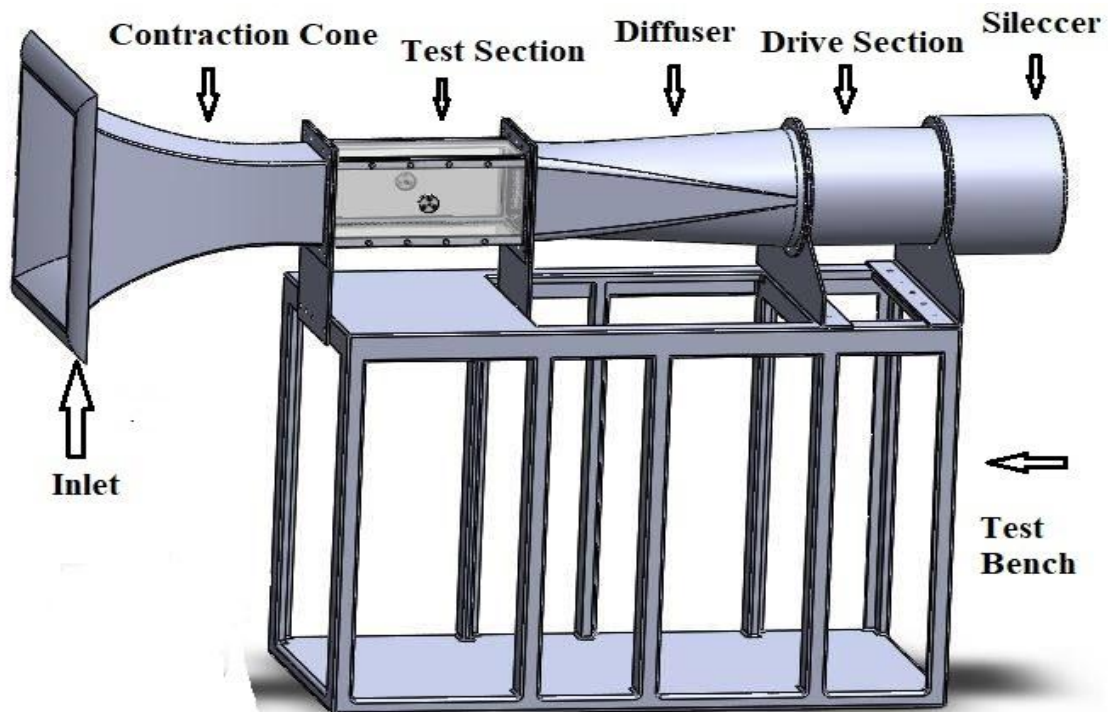
Fig. 6.1 CAD model of AF1300s subsonic wind tunnel

Fig. 6.2 Pictorial view of AF1300s subsonic wind tunnel

As shown in Fig. 6.1 the wind tunnel consists of contraction cone, test section, diffuser, drive section and the silencer. The length of converging and diverging sections of the wind tunnel are 890mm and 1070mm. These two sections are mainly used to control the undesired contraction and expansion losses and to reduce the possibility of flow separation. The test section of the wind turbine is 305mm x 305mm x 600mm. To generate the wind velocity, one axial fan is used. A silencer is there just after the drive section to reduce the noise level. To obtain uniform flow at the exit, a circular to square conversion section with flow straightener and finally a flow stabilizing section are attached at the discharge of the silencer as shown in Fig 6.5.

6.3 Experimental Set-up Description:

For the purpose to carry out the experimental study, a movable test bench is made to mount the turbine. The maximum allowable height of the test-bench is made equal to the height of the wind tunnel bottom, to avoid blockage of airflow due to the structure. A stainless steel shaft of 8mm diameter and length 737mm is made to mount the hub of the turbine, in which the blades are mounted. The height of the test bench is built, maintaining alignment with the wind tunnel central axis. The final test bench CAD model for this study

is shown below in Fig. 6.3 and the associated components after fabrication are shown in Fig. 6.4.
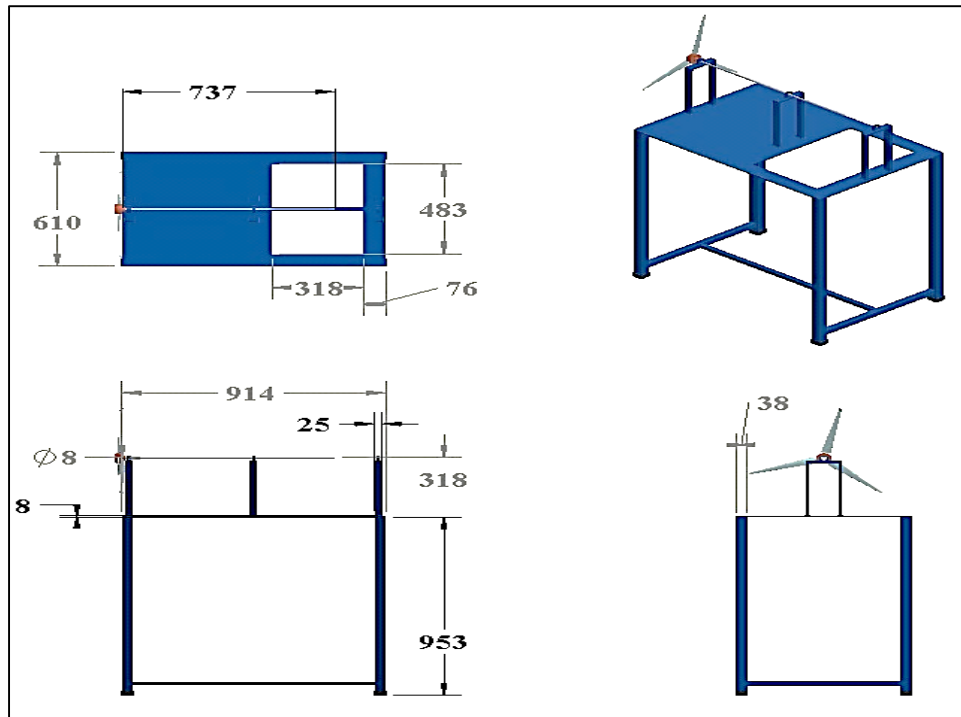
Fig. 6.3 CAD model of experimental test-bench (all dimensions are in 'mm')

The turbine is positioned at about half a rotor diameter from the exit of the wind tunnel with an outlet cross section of 490mm x 490mm. The flow velocity at the exit is controlled by controlling the speed of wind tunnel fan and the turbine is run at different desired flow speed during the experiment. During carrying out the experiment, alignment of the turbine axis is always ensured with that of the wind tunnel. The final assembly of the experimental set-up with the wind tunnel shown in Fig. 6.5.
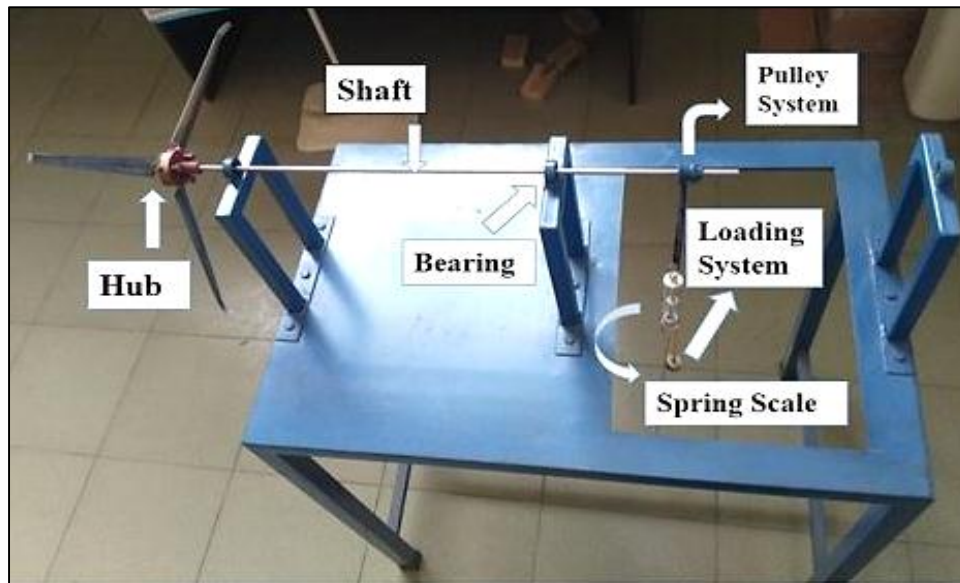
Fig. 6.4 Picture of the components of the experimental test-bench

Free flow velocity is measured by using a digital anemometer with an accuracy of ±5% as shown in Fig. 6.6. At first, the flow velocity is measured without placing the model turbine at different sections and different downstream locations form the exit, and is found to be uniform with ±5% variations. The model turbine is placed at half the rotor diameter downstream from the wind tunnel exit end. For recording the speed or the RPM of wind turbine blades at different loadings, a non-contact digital tachometer is used, as shown in the fig. 6.7. The hub of the model wind turbine is designed with zero coning angle and with the provision of changing blade-pitching angle as required for the present study. The construction materials of the hub is Nylon.

Before the beginning of the experimental study, a spring scale has been calibrated by adding weights at the free end of the springs and observe the deflection of the nob, as shown in Fig. 6.4. The spring scale is fixed at one end of the pulley system. At another end of the pulley system, a facility of slotted weight with holder is there to allow loads for observing the defection in the spring scale.
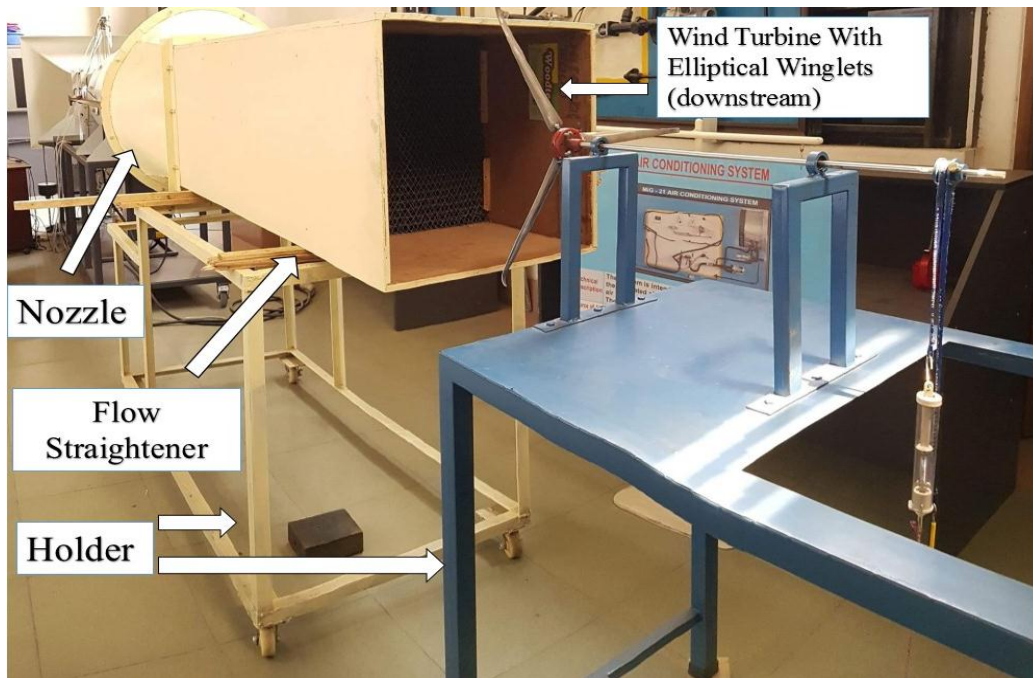
Fig. 6.5 Picture of the wind tunnel facility and experimental model

Fig. 6.6 Photograph of digital anemometer

Fig. 6.7 Digital tachometer (Model: DT-2234B)

6.4 Experimental Procedures

The experimental procedures is described below in short:

a) The wind velocity is measured at different distances from the exit of the wind tunnel without the model turbine.

b) The friction of the belt over the pulley is determined by dry friction method.

c) The wind turbine rotor model with three blades is mounted on the structural frame so that the center of the rotor hub coincides with the central axis of the wind tunnel.

d) At first, the blades are arranged for a zero pitching angle.

e) The digital anemometer measure the wind speed behind the rotor.

f) The spring scale attachment and the loading system are placed in the proper position. It may be noted here that the calibration curve is initially obtained as provided in Appendix-B, from where the force is determined, which converted to torque.

g) The speed of the model wind turbine shaft is measured using a non-contact digital tachometer at different loadings.

h) Differential force is calculated from the spring deflection and applied load.

i) From the distributions, using numerical computation, the non-dimensional torque coefficient, power coefficient are determined.

j) Output powers are obtained from the above readings. The total available power is equal to the summation of the output power and the loss of power due to friction.

k) The experimental values of the power coefficients are calculated from the total available power ratio to the available theoretical power.

l) By changing blade the pitch angle, the above experimental steps from (d) to (i) are repeated to take readings for different pitching angles.

m) Experimental steps from (c) to (k) are repeated for model wind turbine rotors with winglets both in the upstream and downstream direction.

To sum up, the overall research methodology could be shown in flowchart (Fig. 6.8) below:
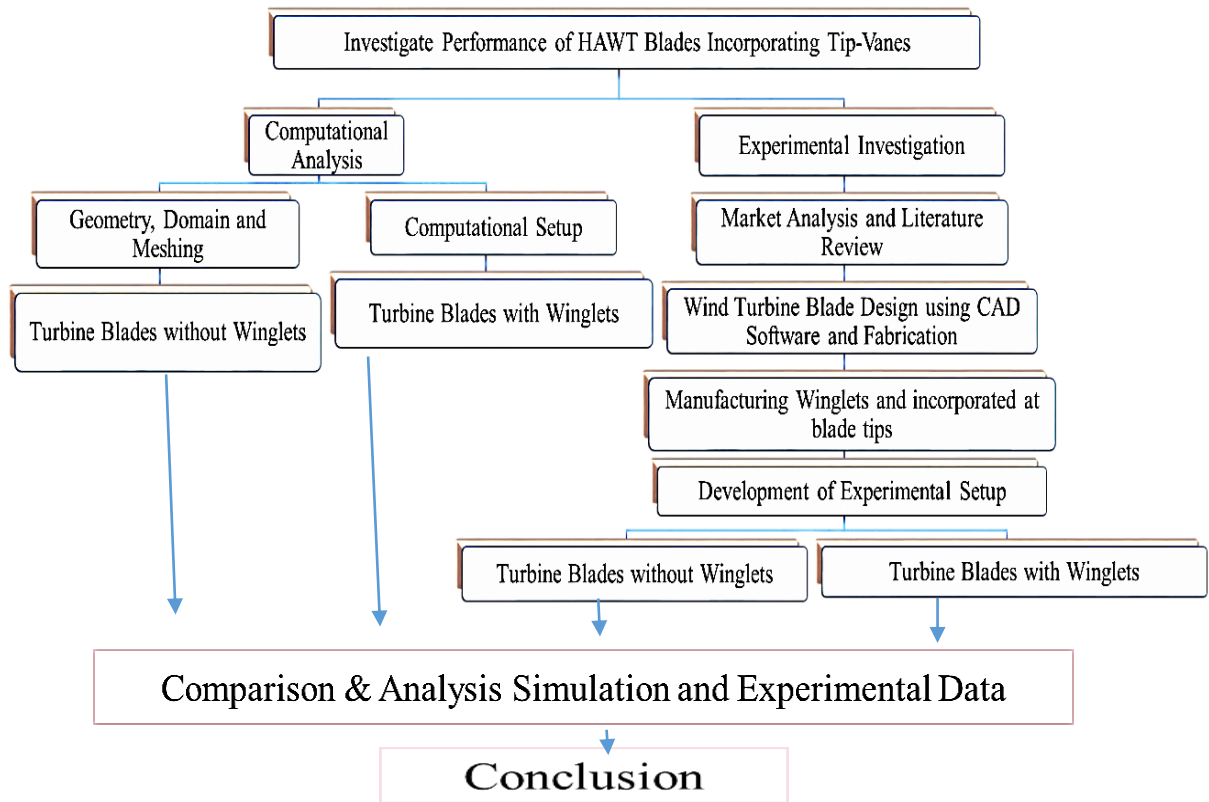
Fig. 6.8 Flow diagram of overall research methodology

CHAPTER 7

RESULTS AND DISCUSSION

7.1 General

Experimental results of the power coefficients, torque coefficients, and thrust coefficients for horizontal axis wind turbines with a circular arc blade profile with and without winglets for different blade pitching angles are presented for the design wind speed 8m/s in this chapter. These experimental results regarding without winglets are then compared with the calculated values using strip theory and, finally, compared for both with and without winglets results with the computational results.

7.2 CFD Validation with Experimental Results

A computational analysis is done to validate the experimental results, as presented in this study, which has been used as a benchmark case to validate the computational results. The experimental data for without winglets are gathered for a particular pitch angle. A comparison between computational and experimental results is then performed before the present study, which is plotted in the Fig. 7.1. Based on these numerical simulations, different design parameters for upstream and downstream winglets are chosen for further research. The graph showed the power coefficient vs. tip-speed ratio from the wind turbine. The power coefficient C_p is defined as:

$$C_P = \frac{P}{\frac{1}{2}\rho A V_\infty^3} \tag{7.1}$$

Tip-speed ratio varies from 1 to 8 for both the experimental and computational investigations. The computational results are slightly higher than that of the experiment due to some operating losses during the experimental analysis and also for the blades' surface

roughness. It is observable that the power coefficient increased to reach a peak at the design tip-speed ratio (TSR=5), and then they decreases dramatically as with the enhancement of the tip-speed ratio. Figure 7.2 represented the error in between the experimental and computational results in terms of the power coefficient for three different cases. The computational power coefficient is within an error of ± (6-7) % from the experimental power coefficient.
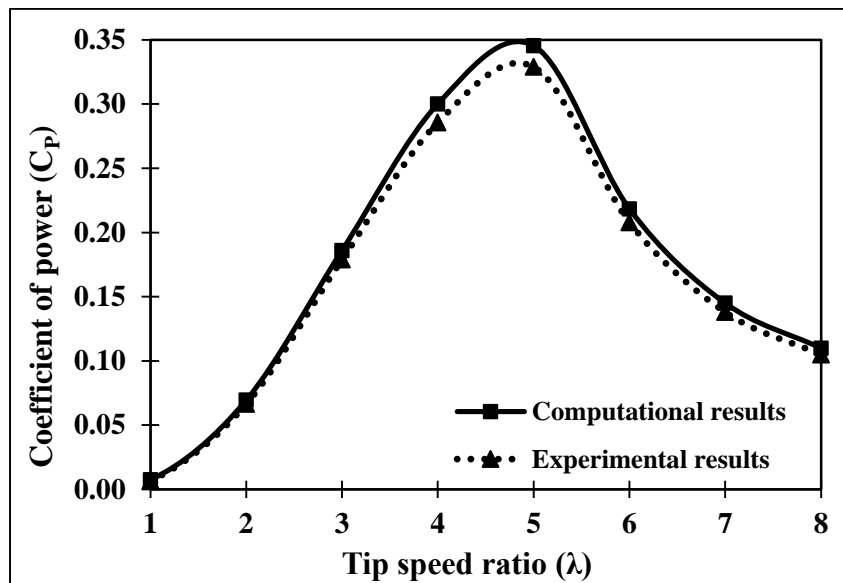
Fig. 7.1 Comparison of power coefficient of the turbine blades without winglets at $\phi_P = 0°$
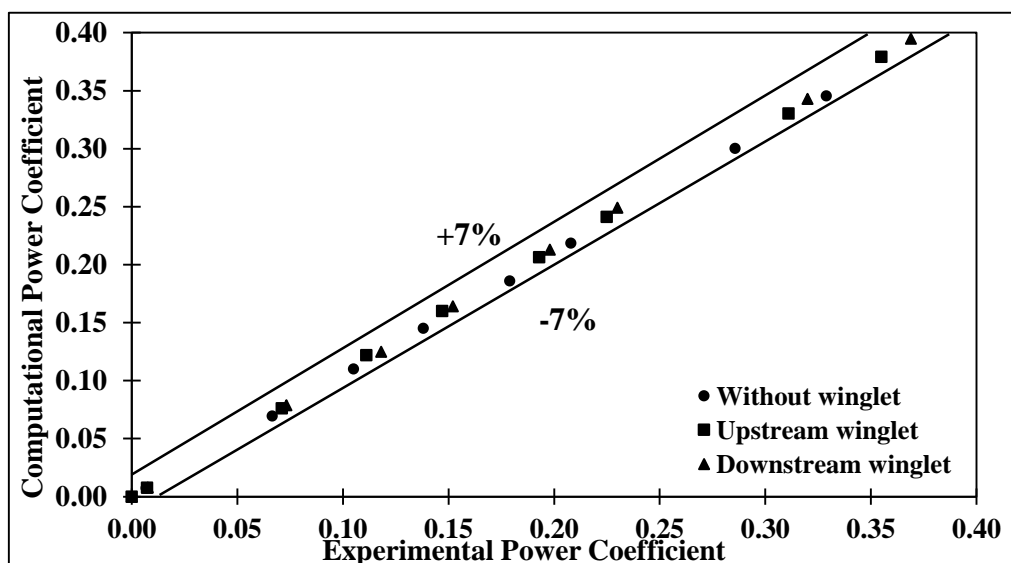
Fig. 7.2 Error of the computational predictions w.r.t. experimental results of wind turbine.

7.3 Experimental Uncertainty

Experimental uncertainty analysis of the power coefficient is carried out depending on each measurement parameter through the combination of systematic error and precision error [61]. Each parameter has some degree of measurement uncertainty. Around 3.92% of the power coefficient uncertainties are measured at the design TSR and zero pitch angle, while seven samples of parameters are selected for estimating that error. Appendix A provides the details of measurement uncertainty.

7.4 Experimental Results

For the experimental investigation, all the three cases, namely blade without winglets (base model), upstream winglets and downstream winglets, are studied by varying tip-speed ratios. In this section, a comparison between the calculated and experimental results of HAWT's power coefficient with a circular arc blade section (CABS) is recorded. The calculated results have been achieved by using the strip theory. For determining the power coefficient, three identical blades having a camberness ratio of 0.08 are used. As the blades are equal in size, the solidity ratio is 0.16, meaning that the model has high speed with low torque. The blade pitching angles are chosen as $0°$, $2°$, $4°$, and $6°$ for each of the prototype models.

7.4.1 Comparison between experimental and strip theory results without winglets

Figure 7.3 (a-d) describe a comparison between the calculated results from the strip theory and experimental results. Strip theory failed to predict the HAWT's performance characteristics adequately, and deviated substantially as the blade pitching angles increased. At design tip-speed ratio (TSR=5), around 6.69% deviation of power coefficient for pitch angle $0º$ is found for experimental results from calculated results. And around 8.81%, 10.01% and 18% deviation for pitch angles $2º$, $4º$ and $6º$ respectively. Using the

momentum theory, the flow velocity through the rotor, i.e., the induced velocity, cannot always be predicted accurately. In terms of the momentum theory, the induced velocity should never be less than half the wind velocity; otherwise, in the wake region, reverse flow occurs. But in reality, the phenomenon is different, and the induced velocity is often below half the wind velocity. And the velocity in the wake region in the downstream side of the wind turbine never occurs in the reverse direction.
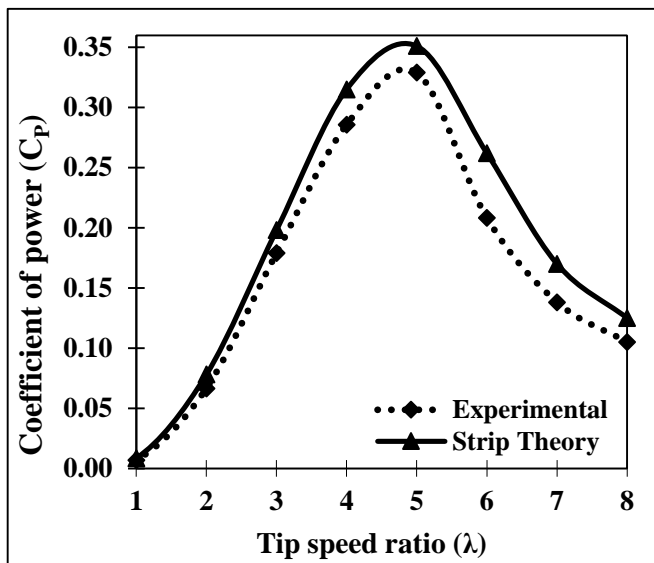
(a) $\phi_P = 0°$
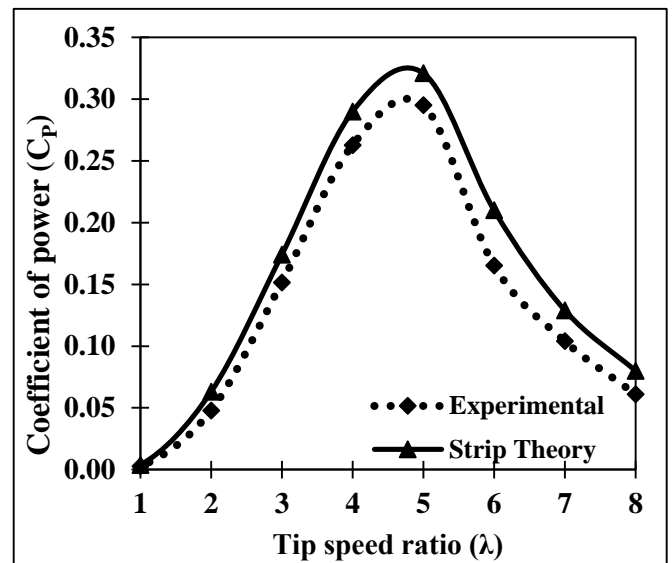
(b) $\phi_P = 2°$
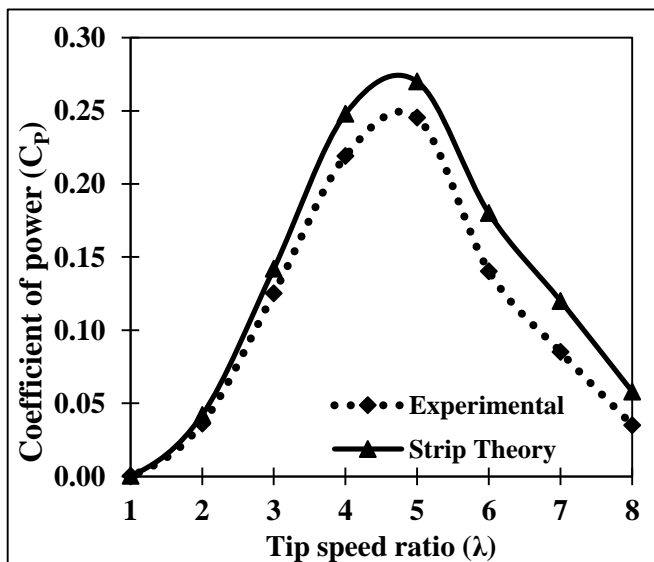
(c) $\phi_P = 4°$
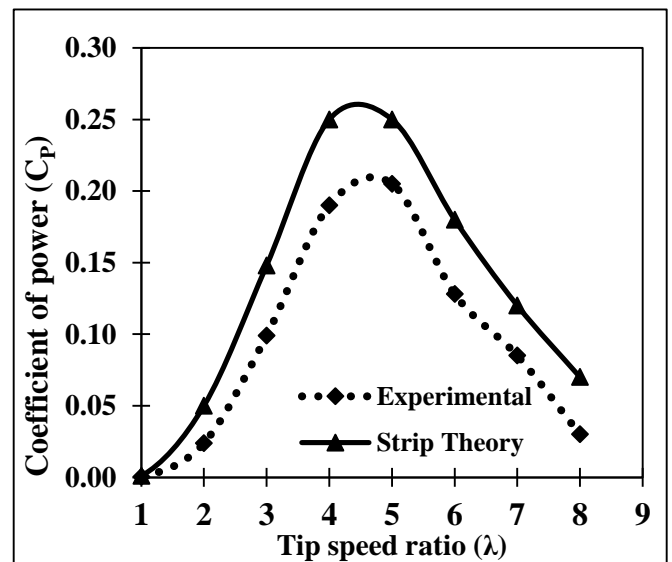
(d) $\phi_P = 6°$

Fig. 7.3 Power coefficient vs. Tip-speed Ratio for different pitch angles

Additionally, the strip theory gives the linear variation consisting of the free stream velocity, induced velocity through the rotor, and the wake velocity. But in reality, the flow velocity pattern is of the exponential form. Furthermore, strip theory hardly counter the blade tip-losses, though blade length is finite. Hence, the lift and drag coefficients of the circular arc blade section enhanced with the increase of tip-speed ratio; thus, an increment on the power coefficient up to the design tip-speed ratio and then fell dramatically.

7.4.2 Effect and comparison of winglets position in power coefficient

In this section, the effects of winglet configurations and their positions, i.e., pressure and suction side, are described.

Figure 7.4 shows the comparison between the power coefficient values vs. tip-speed ratio for different configurations at **pitch angle 0°**. Power coefficient is increased with the increase of the tip-speed ratio up to the design tip-speed ratio (TSR =5) and maximum amount of power coefficient at TSR = 5 is 0.329 for the base model (without winglet), 0.355 for upstream winglet and 0.369 for downstream winglet. Thus, using a circular arc blade section profile, an increase in power coefficient of 7.9% for upstream winglets and around 12.1% for downstream winglets is obtained when compared to using no winglets for the design tip speed ratio (TSR =5). Table 7.1 represents C_P values for different tip-speed ratios, and Table 7.2 represents the average increase in power coefficient in percentage, which can be found in the appendix B. It can be said that there is an increment of an average of 7.7% and 11.33% in power production capability, while using upstream and downstream winglets, respectively.
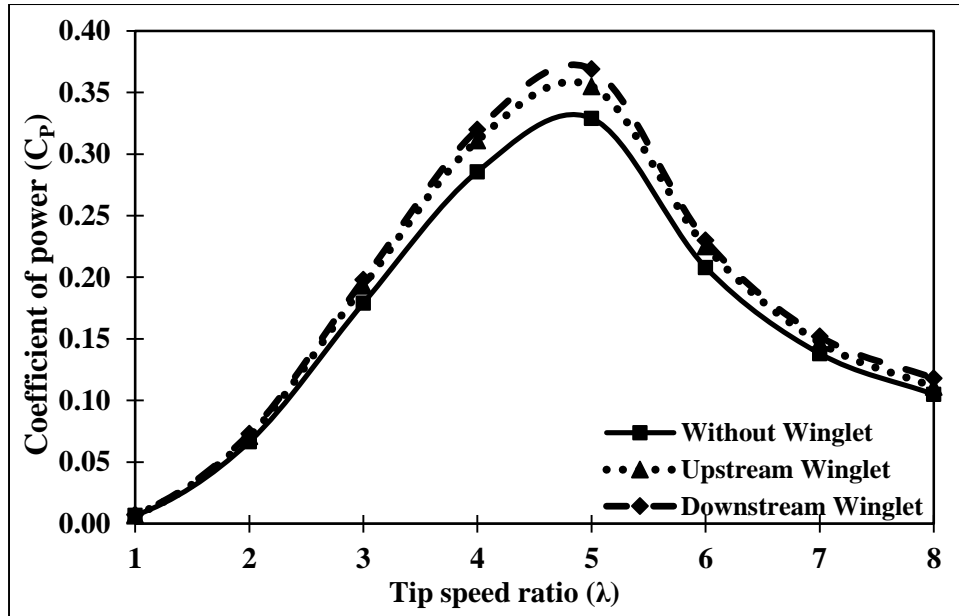
Fig. 7.4 Comparison of experimental results of winglets position in power coefficient for

$$\phi_P = 0^\circ$$

Figure 7.5 shows that the power coefficient values at **pitch angle 2°**. With an increase in the tip speed ratio, the power coefficient increases up to the design tip-speed ratio (TSR =5) and maximum amount of power coefficient at TSR = 5 is 0.295 for base model (without winglet), 0.319 for upstream winglet and 0.329 for downstream winglet. Thus, using a circular arc blade section profile, an increase in power coefficient of 8.13% for upstream winglets and around 11.53% for downstream winglets is obtained when compared to using no winglets for the design tip speed ratio (TSR=5).

Table 7.3 represents C_P values for different tip-speed ratios, and table 7.4 represents the average increase of power coefficient in percentage. It is apparent that there is increment of an average of 8.58% and 11.73% in power production capability, while using upstream and downstream winglets, respectively.
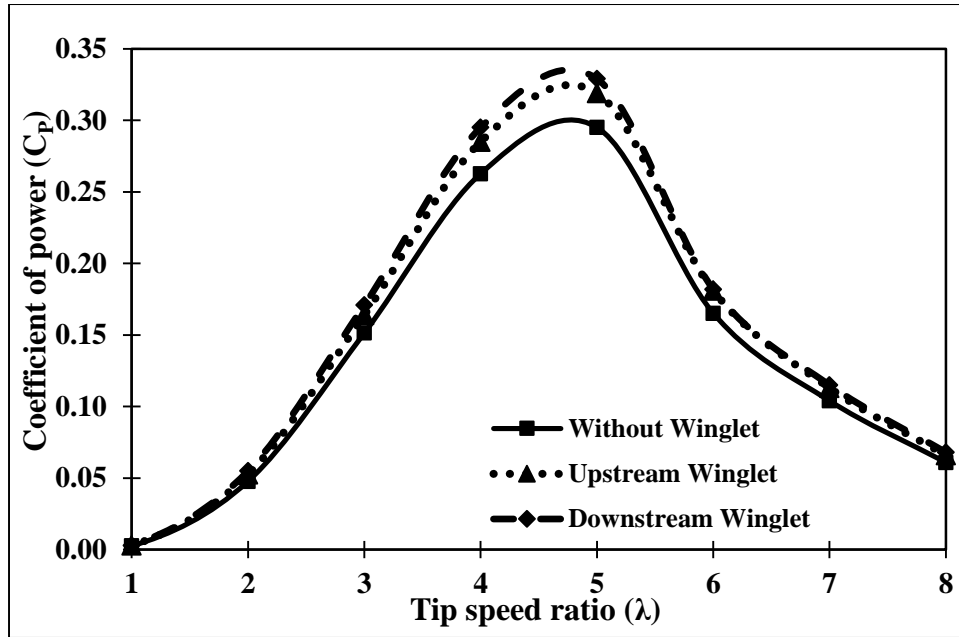
Fig. 7.5 Comparison of experimental results of winglets position in power coefficient for

$$\phi_P = 2°$$

Figure 7.6 shows that the power coefficient values at **pitch angle 4°**. With an increase in the tip speed ratio, the power coefficient increases up to the design tip-speed ratio (TSR =5) and maximum amount of power coefficient at TSR = 5 is 0.2453 for base model (without winglet), 0.265 for upstream winglet and 0.275 for downstream winglet. Thus, using a circular arc blade section profile, an increase in power coefficient of 8.03% for upstream winglets and around 12.11% for downstream winglets is obtained when compared to using no winglets for the design tip speed ratio (TSR=5).

Table 7.5 represents C_P values for different tip-speed ratios, and Table 7.6 represents the average increase of power coefficient in percentage. It can be said that is an increment of an average of 9.85% and 12.70% in power production capability, while using upstream and downstream winglets, respectively.
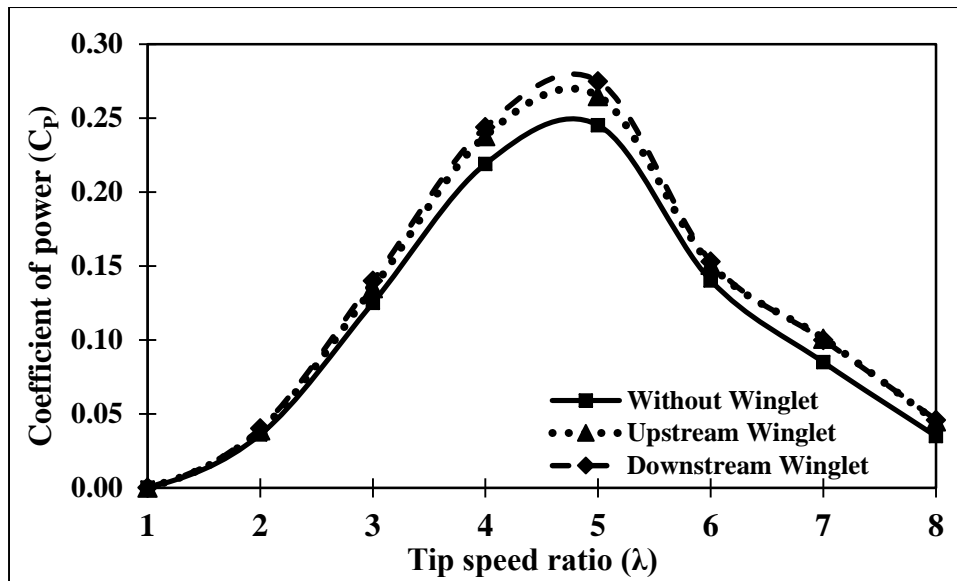
Fig. 7.6 Comparison of experimental results of winglets position in power coefficient for
$\phi_P = 4°$

Figure 7.7 shows that the power coefficient values at **pitch angle 6°**. With an increase in the tip speed ratio, the power coefficient increases up to the design tip-speed ratio (TSR =5) and maximum amount of power coefficient at TSR = 5 is 0.205 for base model (without winglet), 0.225 for upstream winglet and 0.231 for downstream winglet. Thus, using a circular arc blade section profile, an increase in power coefficient of 9.76% for upstream winglets and around 12.67% for downstream winglets is obtained when compared to using no winglets for the design tip speed ratio (TSR=5).

Table 7.7 represents C_P values for different tip-speed ratios, and Table 7.8 represents the average increase of power coefficient in percentage. It can be said that there is an increment of an average of 11.94% and 13.01% in power production capability, while using upstream and downstream winglets, respectively.

In all cases, it is evident that blades with downstream winglets provided better performance than blades with upstream winglets. Furthermore, the tip vortices move further away from the downstream side and that is the reason for the better performance.
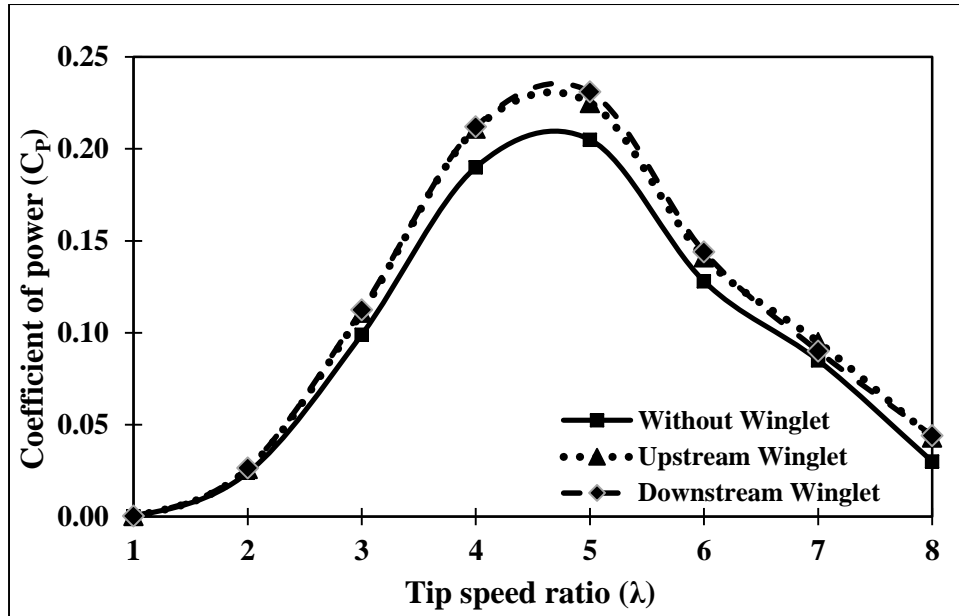
Fig. 7.7 Comparison of experimental results of winglets position in power coefficient for
$$\phi_P = 6°$$

7.4.3 Torque coefficient distribution for different pitch angles

When the air molecules impart on the wind turbine blades, the resultant forces divided into two components, namely, axial force and tangential force. This tangential force is the primary reason for torque generation. A comparison between torque coefficient vs. tip-speed ratio and how they affect extracting energy from wind has been discussed in this section. From Fig. 7.8 to Fig. 7.10, the effects of pitch angles 0°, 2°, 4°, 6° have been described for three different cases. It is evident that the maximum amount of torque produced for pitch angle is zero and then decreases substantially as the pitch angle increases in all other cases.

As pitch angles increase and torque coefficient decreases leading to higher tip speeds at the outer portion of the blade. Due to the high tip speeds, an additional drag imposed on the blades, thus reducing the power generation, as we observed in the above section.

Regarding the blades having **no winglets** (base model), the maximum value of the torque coefficient is around 0.0714 for $\phi_P = 0°$ at TSR=4 (Table 7.9), and then, there are significant drop of about 0.0657, 0.0548 and 0.0475 in the torque coefficient for $\phi_P = 2°$, 4°, 6° (Table 7.9) respectively. A similar trend found for the other tip-speed ratios too. An average of around 17.16%, 33.14%, 43.79% reduction is faced from the results of $\phi_P = 0°$ to pitching angles = 2°, 4°, 6° respectively (Table 7.10).
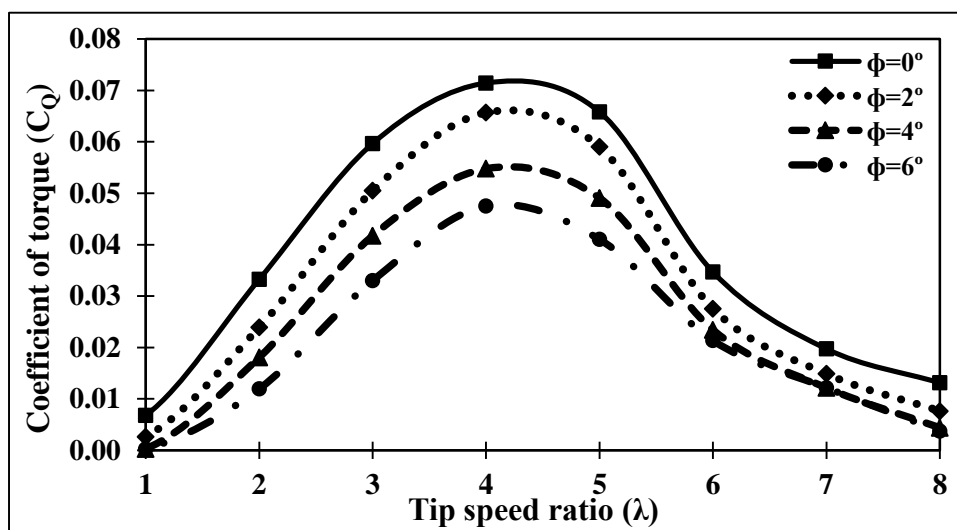
Fig. 7.8 Comparison of experimental results of torque coefficient at different pitch angles for without winglets

Regarding the blades having **upstream winglets**, the maximum value of the torque coefficient is around 0.0778 for $\phi_P = 0°$ at TSR=4 (Table 7.11), and then, there are significant drop of about 0.0713, 0.0595 and 0.0528 at TSR=4 in the torque coefficient for $\phi_P = 2°$, 4°, 6° respectively. A similar trend found for the other tip-speed ratios too. An average of around 16.72%, 32.33%, 41.92% reduction faced from the results of $\phi_P = 0°$ for pitching angles = 2°, 4°, 6° respectively (Table 7.12).
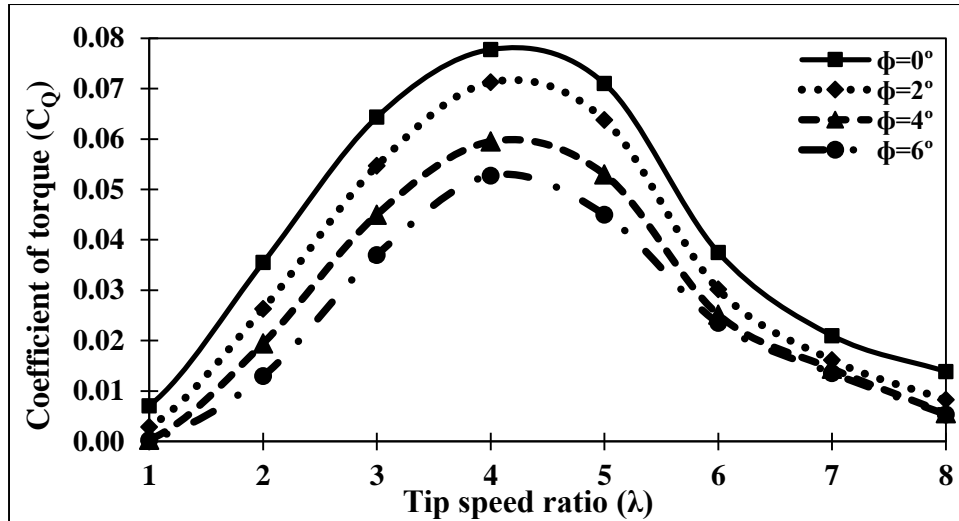
Fig. 7.9 Comparison of experimental results of torque coefficient at different pitch angles for upstream winglets

Regarding the blades having **downstream winglets**, the maximum value of the torque coefficient is around 0.08 for $\phi_P = 0°$ at TSR=4 (Table 7.13), and then, there are significant drop of about 0.0738, 0.0610 and 0.0530 at TSR=4 in the torque coefficient for $\phi_P = 2°$, 4°, 6° respectively. A similar trend found for the other tip-speed ratios too. An average of around 16.49%, 32.45%, 43.06% reduction faced from the results of $\phi_P = 0°$ for pitching angles $\phi_P = 2°$, 4°, 6° respectively (Table 7.14).

Fig. 7.10 Comparison of experimental results of torque coefficient at different pitch angles for downstream winglets

Regarding the blades in **Pitching angle** $\phi_P = 0^o$ shown in Fig. 7.11, the maximum

value of the torque coefficient is around 0.0714 for without winglets at TSR=4 (Table 7.15),

and then, there are significant rise of about 0.0778 and 0.08 at TSR=4 in the torque

coefficient for upstream and downstream winglets respectively. A similar trend found for

the other tip-speed ratios too. An average of around 7.99% and 11.24% increment found

for upstream and downstream winglets in terms of without winglets respectively (Table

7.16).
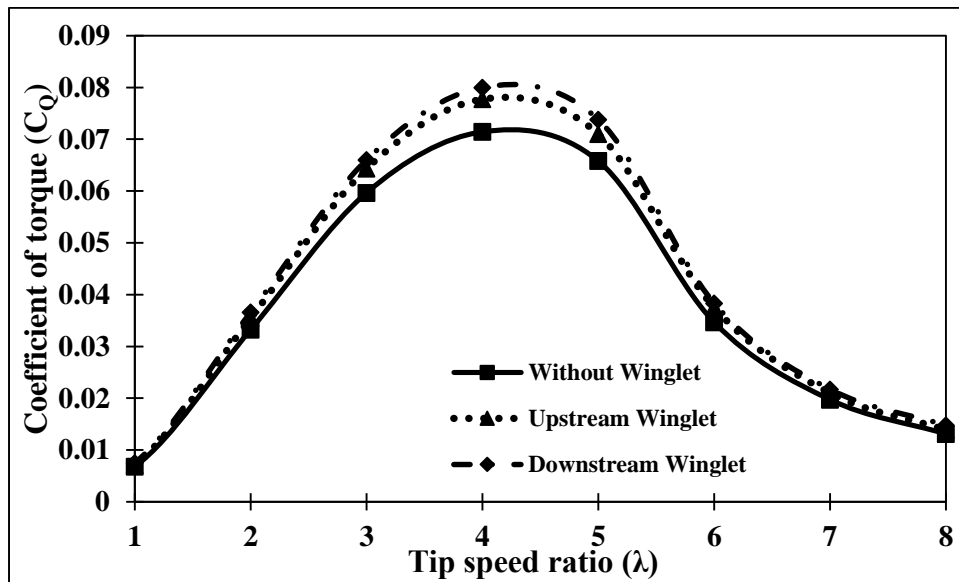
Fig. 7.11 Comparison of experimental results of torque coefficient for different winglets

at $\phi_P = 0^o$

Regarding the blades in **Pitching angle** $\phi_P = 2^o$ shown in Fig. 7.12, the maximum

value of the torque coefficient is around 0.0657 for without winglets at TSR=4 (Table 7.17),

and then, there are significant rise of about 0.0713 and 0.0738 at TSR=4 in the torque

coefficient for upstream and downstream winglets respectively. A similar trend found for

the other tip-speed ratios too. An average of around 8.57% and 12.14% increment found

for upstream and downstream winglets in terms of without winglets respectively (Table

7.18).
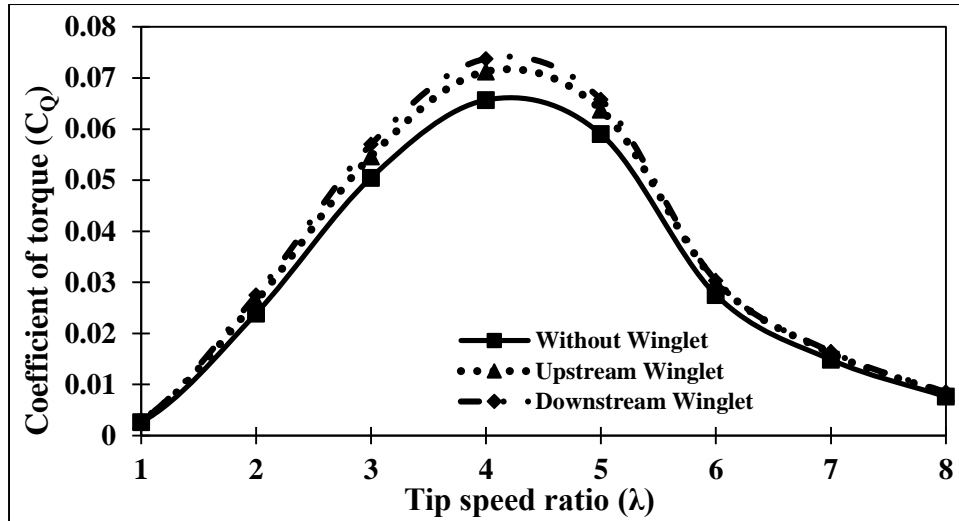
Fig. 7.12 Comparison of experimental results of torque coefficient for different winglets at $\phi_P = 2°$

Regarding the blades in **Pitching angle = 4°** shown in Fig. 7.13, the maximum value of the torque coefficient is around 0.0548 for without winglets at TSR=4 (Table 7.19), and then, there are significant rise of about 0.0595 and 0.0610 at TSR=4 in the torque coefficient for upstream and downstream winglets respectively. An average of around 9.39% and 12.39% increment found for upstream and downstream winglets in terms of without winglets respectively (Table 7.20).

Fig. 7.13 Comparison of experimental results of torque coefficient for different winglets at $\phi_P = 4°$

Regarding the prototype blades in **Pitching angle = 6º** shown in Fig. 7.14, the maximum value of the torque coefficient is around 0.0475 for without winglets at TSR=4 (Table 7.21), and then, there are significant rise of about 0.0528 and 0.0530 at TSR=4 in the torque coefficient for upstream and downstream winglets respectively. An average of around 11.58% and 12.63% increment found for upstream and downstream winglets in terms of without winglets respectively (Table 7.22).

Fig. 7.14 Comparison of experimental results of torque coefficient for different winglets at $\phi_P = 6º$

7.4.4 Effect of thrust coefficient with and without winglets

During the wind turbine model design, it is required to check structural integrity as there are numerous effects on blades, for instance, radially, aerodynamic effects, and thrust forces. Blades rotation and aerodynamic forces lead to radial loads and bending loads, respectively, while thrust loads have a significant impact on supporting tower. The thrust coefficient for the wind turbine can be calculated from the give equation below:

$$C_T = \frac{T}{\frac{1}{2}\rho A V_\infty^2}$$
(7.2)

The above equation can be used while the blade pitching angle is zero, hence directly impacting the air molecules on the blades. But in case of increasing the pitching angle at

the same free stream velocity, the projected area normal to the wind speed direction reduces. Thus, with the increment of the pitching angle, the thrust coefficient decreases significantly. The modified thrust coefficient equation can be written as below.

$$C_T = \frac{T}{\frac{1}{2}\rho A V_\infty^2 \cos\phi} \qquad (7.3)$$

Regarding the prototype blades having **no winglets** shown in Fig. 7.15, at lower tip-speed ratio the thrust coefficient variation for different pitching angles are almost negligible (up to TSR=5), but after that at higher tip-speed ratios variations are prominent. The maximum values of the thrust coefficient are obtained for $\phi_P = 0°$, and then, there are slight drop in the thrust coefficient for $\phi_P = 2°$, 4°, 6° respectively as shown in Table 7.23. An average of around 3.09%, 7.68%, 13.43% reduction faced from the results of $\phi_P = 0°$ to pitching angles $\phi_P = 2°$, 4°, 6° respectively (Table 7.24).
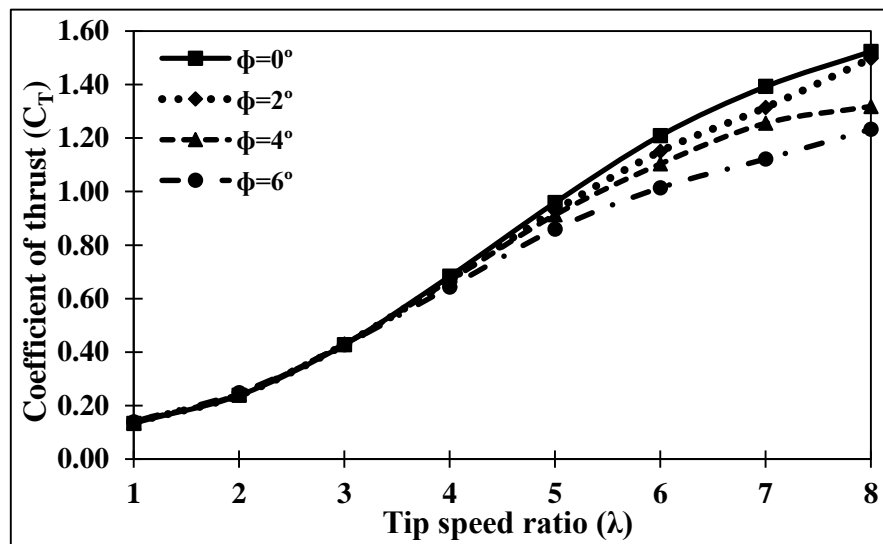
Fig. 7.15 Comparison of experimental results of thrust coefficient at different pitch angles for without winglets

Concerning the prototype blades having **Upstream winglets** shown in Fig. 7.16, at lower tip-speed ratio the thrust coefficient variation for different pitching angles are almost negligible (up to TSR=5), but after that at higher tip-speed ratios variations are prominent.

The maximum values of the thrust coefficient are obtained for $\phi_P = 0°$, and then, there are slight drop in the thrust coefficient for $\phi_P = 2°$, 4°, 6° respectively as shown in Table 7.25. An average of around 4.36%, 9.11%, 17.89% reduction faced from the results of $\phi_P = 0°$ to pitching angles = 2°, 4°, 6° respectively (Table 7.26).
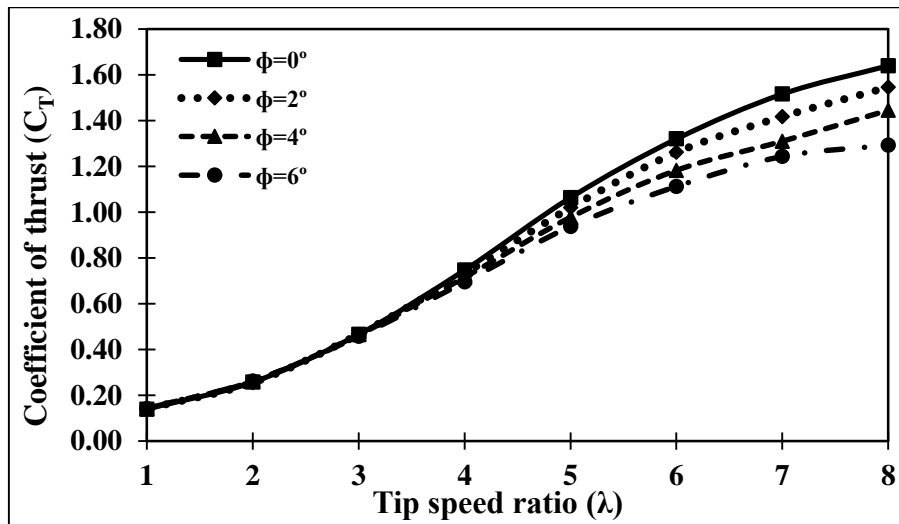
Fig. 7.16 Comparison of experimental results of thrust coefficient at different pitch angles for upstream winglets

Concerning the prototype blades having **Downstream winglets** shown in Fig. 7.17, at lower tip-speed ratio the thrust coefficient variation for different pitching angles are almost negligible (up to TSR=5), but after that at higher tip-speed ratios variations are prominent. The maximum values of the thrust coefficient are obtained for $\phi_P = 0°$, and then, there are slight drop in the thrust coefficient for $\phi_P = 2°$, 4°, 6° respectively as shown in Table 7.27. An average of around 6.66%, 10.61%, 16.56% reduction faced from the results of $\phi_P = 0°$ to pitching angles = 2°, 4°, 6° respectively (Table 7.28).
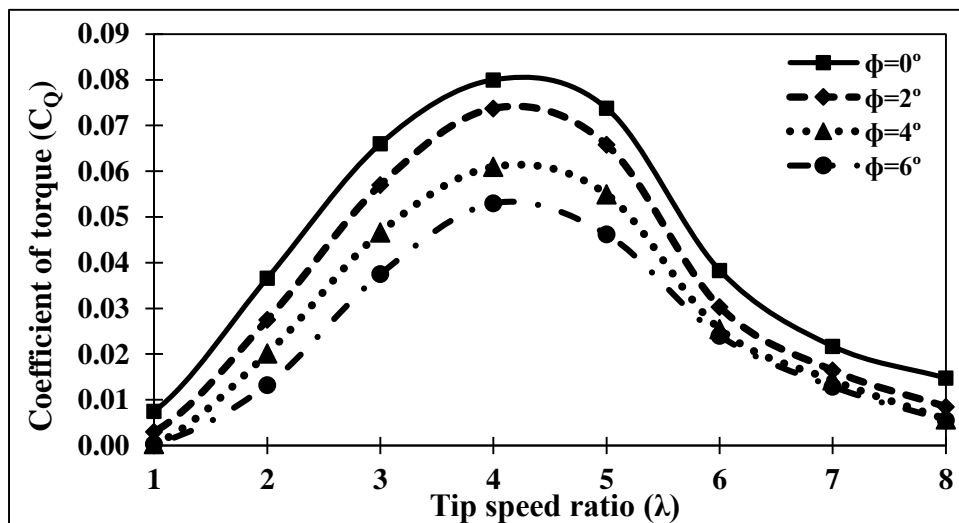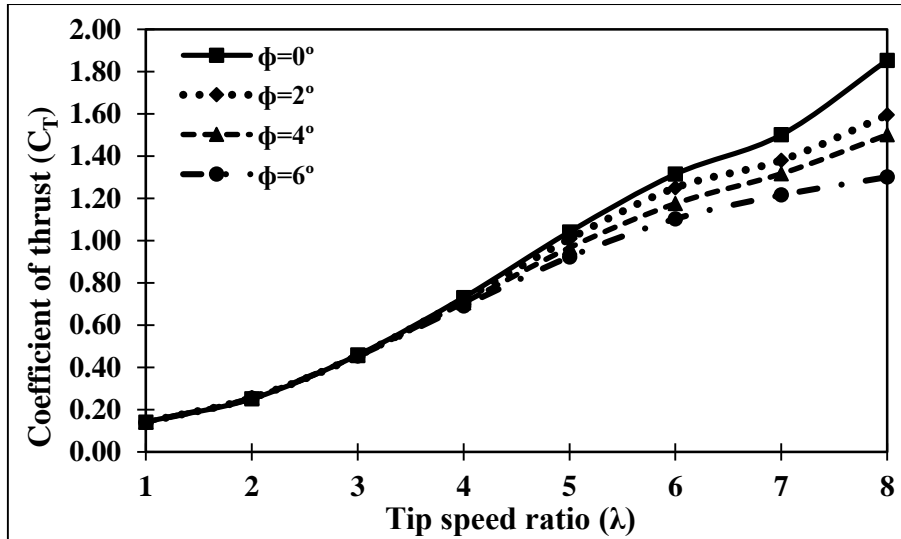
Fig. 7.17 Comparison of experimental results of thrust coefficient at different pitch angles for downstream winglets

Regarding the wind turbine blades in **Pitching angle** $\phi_P = 0^o$ shown in Fig. 7.18, at lower tip-speed ratio the thrust coefficient variation for different cases are almost negligible (up to TSR=3), but after that at higher tip-speed ratios variations are more considerable. The maximum value of the thrust coefficient is found for downstream winglets (Table 7.29), and then the least value of the thrust coefficient is found for having no winglets an average of around 8.95% and 10.98% increment found for upstream and downstream winglets in terms of without winglets respectively (Table 7.30).
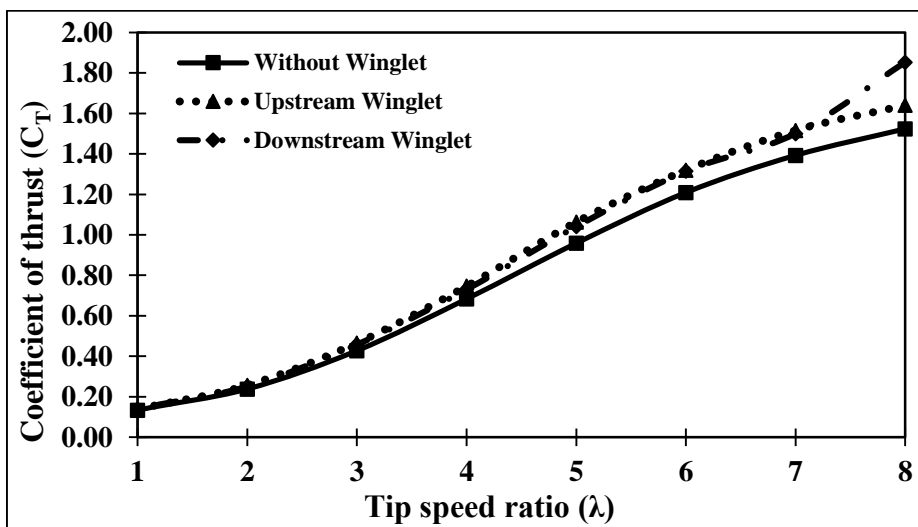
Fig. 7.18 Comparison of experimental results of thrust coefficient for different winglets at

$$\phi_P = 0^o$$

Regarding the wind turbine blades in **Pitching angle** $\phi_P = 2°$ shown in Fig. 7.19, at lower

tip-speed ratio the thrust coefficient variation for different cases are almost negligible (up

to TSR=3), but after that at higher tip-speed ratios variations are not so considerable. The

maximum value of the thrust coefficient is found for downstream winglets (Table 7.31),

and then the least value of the thrust coefficient is found for having no winglets. An average

of around 6.89% and 7.43% increment found for upstream and downstream winglets in

terms of without winglets respectively (Table 7.32).
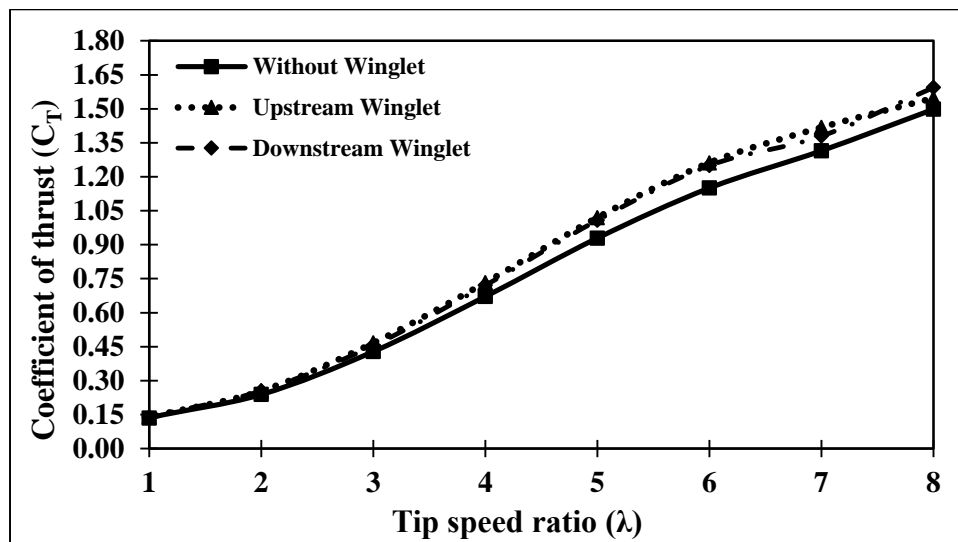
Fig. 7.19 Comparison of experimental results of thrust coefficient for different winglets at

$$\phi_P = 2°$$

Regarding the wind turbine blades in **Pitching angle** $\phi_P = 4°$ shown in Fig. 7.20,

at lower tip-speed ratio the thrust coefficient variation for different cases are almost

negligible (up to TSR=3), but after that at higher tip-speed ratios variations hardly

considerable. The maximum value of the thrust coefficient is achieved for downstream

winglets (Table 7.33), and then the least value of the thrust coefficient is found for having

no winglets. An average of around 7.16% and 7.45% increment found for upstream and

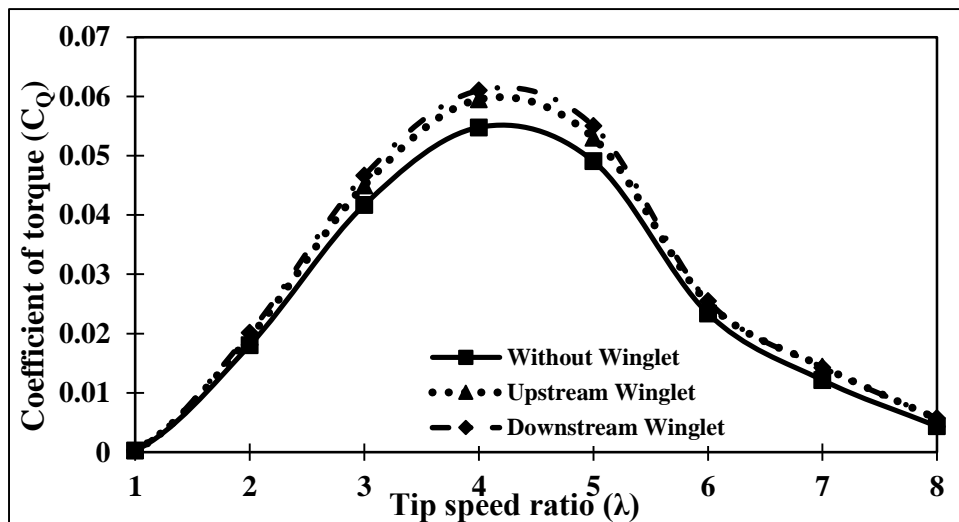downstream winglets in terms of without winglets respectively (Table 7.34).
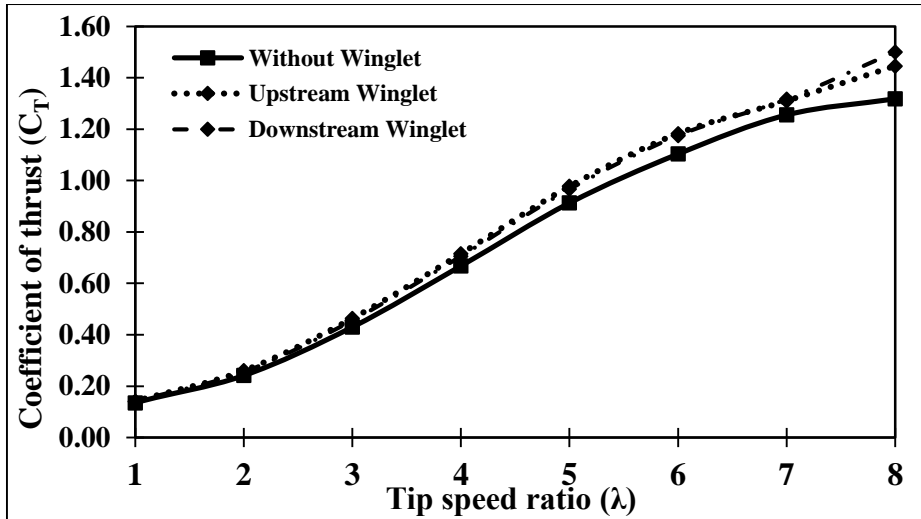
Fig. 7.20 Comparison of experimental results of thrust coefficient for different winglets at

$$\phi_P = 4^\circ$$

Regarding the wind turbine blades in **Pitching angle $\phi_P = 6^\circ$** shown in Fig. 7.21, at lower tip-speed ratio the thrust coefficient variation for different cases are almost negligible (up to TSR=3), but after that at higher tip-speed ratios variations are considerable. The maximum value of the thrust coefficient is found for downstream winglets (Table 7.35), and then the least value of the thrust coefficient is found for having no winglets. An average of around 6.97% and 8.00% increment found for upstream and downstream winglets in terms of without winglets respectively (Table 7.36).
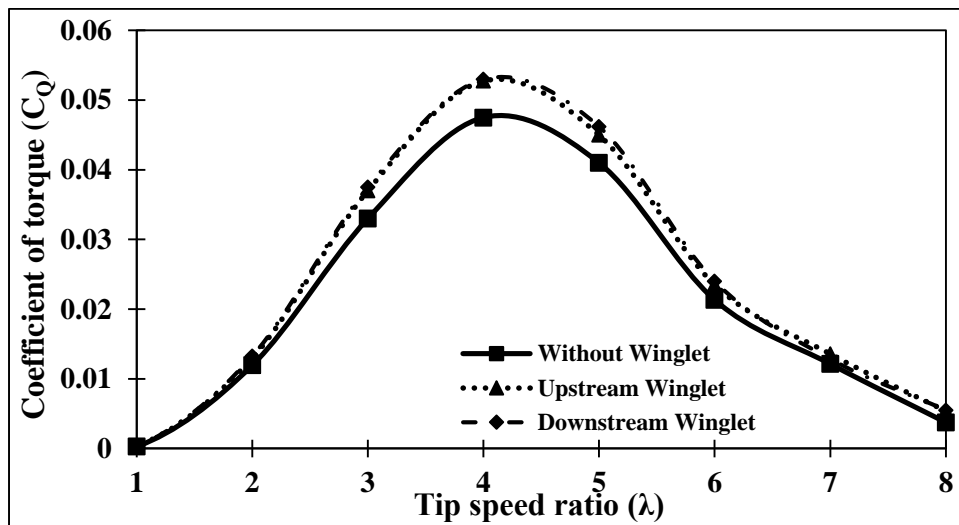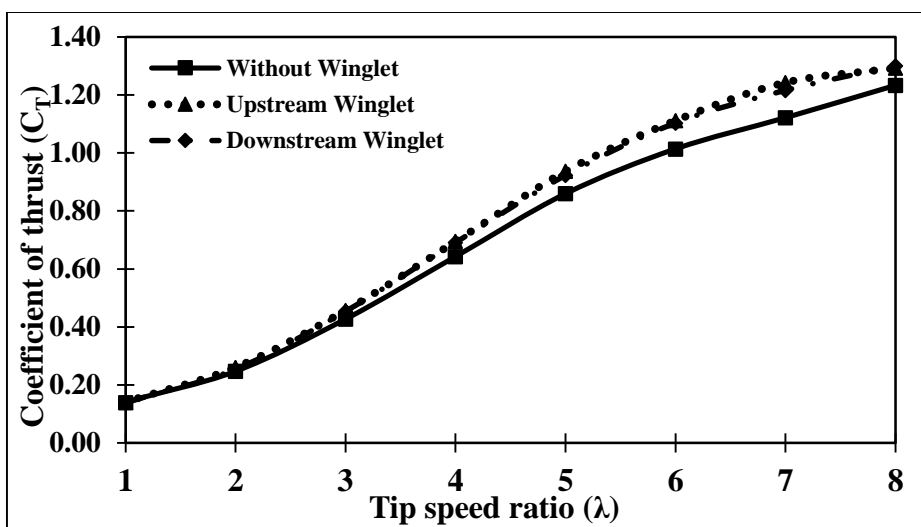

Fig. 7.21 Comparison of experimental results of thrust coefficient for different winglets at

$$\phi_P = 6^\circ$$

7.5 Computational Results

In this section, the computational results of all cases will be discussed at the design wind speed of 8m/s. A comparison between the experimental results with the computational results and the percentage of variation will be discussed. Additionally, changes in pressure coefficients, along with the blade length and the compensation of the tip-vortex by the winglets, are also mentioned.

7.5.1 Comparison between experimental and computational results with and without elliptical winglets

From Fig. 7.22 to Fig. 7.25 comparison between experimental and computational results for with and without winglets at different tip-speed ratios and pitch angles are represented. Table 7.37 showed the values at different tip-speed ratios when the wind turbine blades are adjusted in the **Pitching angle $\phi_P = 0°$**. It can be said that, as the tip-speed ratio increases, the power coefficients are also increased until the design tip-speed ratio 5, which has the maximum value of C_P, and after TSR=5, the values drop substantially. The average values for each of the cases are also calculated. Tables 7.38 and 7.39 illustrate the percentage (%) of the increase of power coefficient C_P for incorporating the upstream and downstream winglets with respect to without winglets at three different TSR = 4, 5, 6 and $\phi_P = 0°$.

Regarding the experimental results, around 8.85%, 7.91%, and 8.18% increment is there while adding the winglets at the upstream side. Meanwhile, around 12.01%, 12.10%, and 10.58% increment is there while adding the winglets at the downstream side.

In the case of computational results, around 10.03%, 9.79%, and 10.35% increment is there while adding the winglets at the upstream side. In contrast, about 14.30%, 14.36%, and 14.06% increment is there while adding the winglets at the downstream side.

From each of the cases, it can be concluded that the attachment of downstream winglets are better than upstream winglets, and computational results are considerably higher than experimental results. This is due to the manufacturing difficulties and roughness in the blade surfaces, which are negligible in the computational analysis.
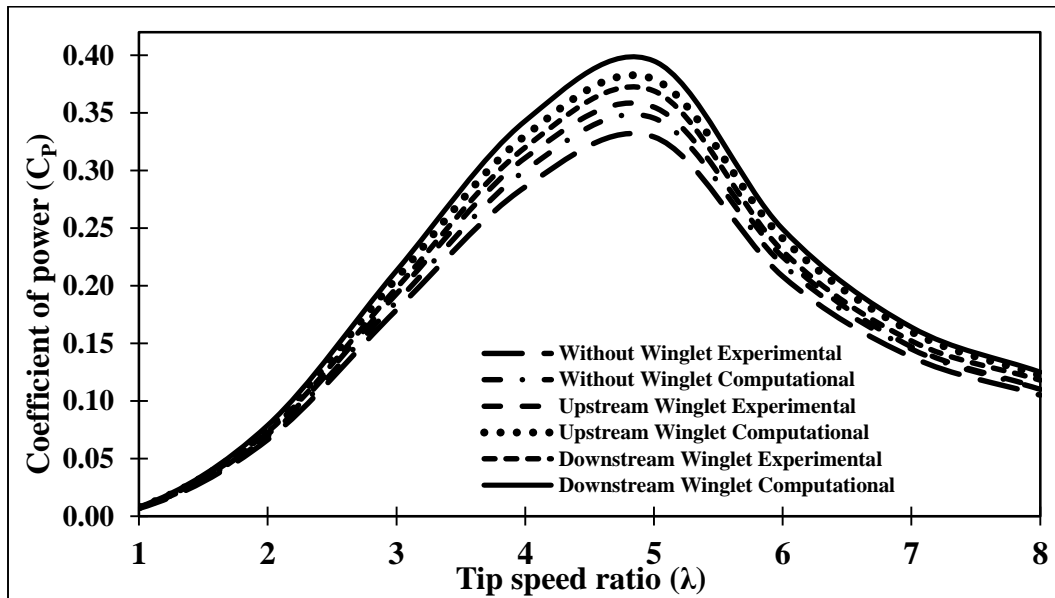
Fig. 7.22 Power coefficient at different tip-speed ratios at $\phi_P = 0°$

Table 7.40 showed the values at different tip-speed ratios when the wind turbine blades are adjusted in the **Pitching angle $\phi_P = 2°$**. It can be said that, as the tip-speed ratio increases, the power coefficients are also increased until the design tip-speed ratio 5, which has the maximum value of C_P, and after TSR=5, the values drop substantially. The average values for each of the cases are also calculated. Tables 7.41 and 7.42 illustrate the percentage (%) of the increase of power coefficient C_P for incorporating the upstream and downstream winglets with respect to without winglets at three different TSR =4, 5, 6 and $\phi_P = 0°$.

Regarding the experimental results, around 8.49%, 8.14%, and 9.56% increment is there while adding the winglets at the upstream side. Meanwhile, around 12.30%, 11.53%, and 10.17% increment is there while adding the winglets at the downstream side.

In the case of computational results, around 10.51%, 10.31%, and 11.24% increment is there while adding the winglets at the upstream side. In contrast, about 14.46%, 14.13%, and 14.70% increment is there while adding the winglets at the downstream side. From each of the cases, it can be observed that the attachment of downstream winglets is better than upstream winglets.
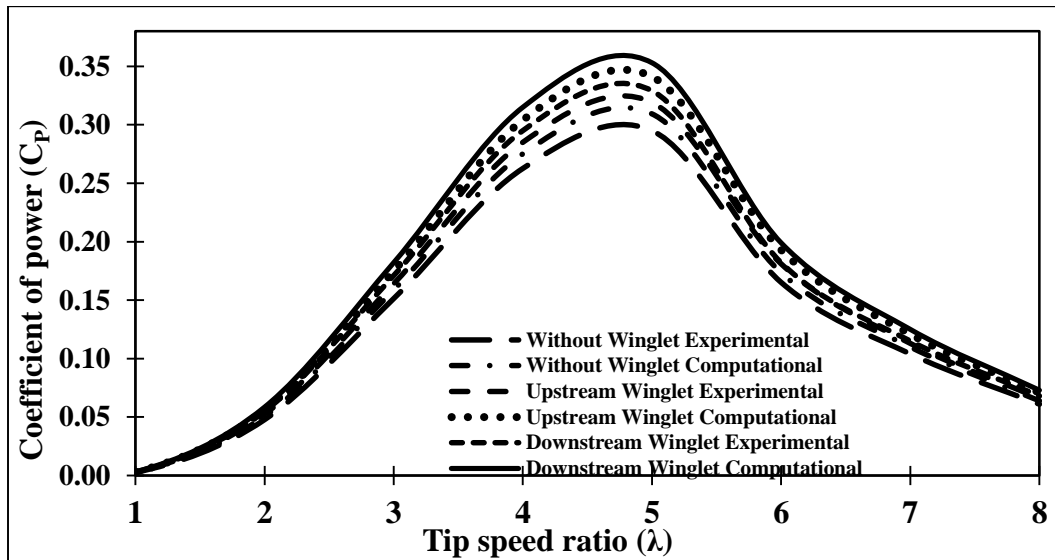
Fig. 7.23 Power coefficient at different tip-speed ratios at $\phi_P = 2^\circ$

Table 7.43 showed the values at different tip-speed ratios when the wind turbine blades are adjusted in the **Pitching angle $\phi_P = 4^\circ$**. It can be said that, as the tip-speed ratio increases, the power coefficients are also increased until the design tip-speed ratio 5, which has the maximum value of C_P, and after TSR=5, the values drop substantially. The average values for each of the cases are also calculated. Tables 7.44 and 7.45 illustrate the percentage (%) of the increase of power coefficient C_P for incorporating the upstream and downstream winglets with respect to without winglets at three different TSR = 4, 5, 6 and $\phi_P = 0^\circ$.

Regarding the experimental results, around 8.63%, 8.03%, and 7.63% increment is there while adding the winglets at the upstream side. Meanwhile, around 11.37%, 12.11%, and 09.05% increment is there while adding the winglets at the downstream side. In the case of computational results, around 10.43%, 10.29%, and 10.66% increment is there while adding the winglets at the upstream side. In contrast, about 14.35%, 14.56%, and 12.39% increment is there while adding the winglets at the downstream side. From each of the cases, it can mentioned that the attachment of downstream winglets is better than upstream winglets.
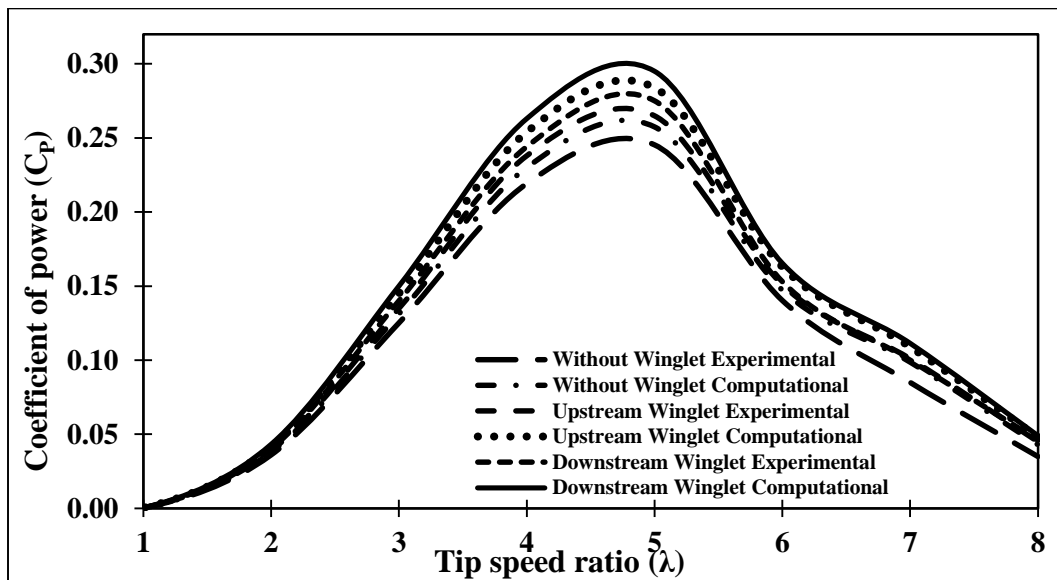
Fig. 7.24 Power Coefficient at different tip-speed ratios at $\phi_P = 4°$

Table 7.46 described the values at different tip-speed ratios when the wind turbine blades are adjusted in the **Pitching angle** $\phi_P = 6°$. It can be said that, as the tip-speed ratio increases, the power coefficients are also increased until the design tip-speed ratio 5, which has the maximum value of C_P, and after TSR=5, the values decrees substantially. The average values for each of the cases are also calculated. Tables 7.47 and 7.48 illustrate the percentage (%) of the increase of power coefficient C_P for incorporating the upstream and

downstream winglets with respect to without winglets at three different TSR = 4, 5, 6 and

$\phi_P = 0°$.

Regarding the experimental results, around 11.05%, 9.76%, and 10.66% increment is there while adding the winglets at the upstream side. Meanwhile, around 11.58%, 12.68%, and 12.50% increment is there while adding the winglets at the downstream side. In the case of computational results, around 11.88%, 10.39%, and 10.30% increment is there while adding the winglets at the upstream side. In contrast, about 14.57%, 14.55%, and 13.22% increment is there while adding the winglets at the downstream side. From each of the cases, it can be concluded that the attachment of downstream winglets is better than upstream winglets.
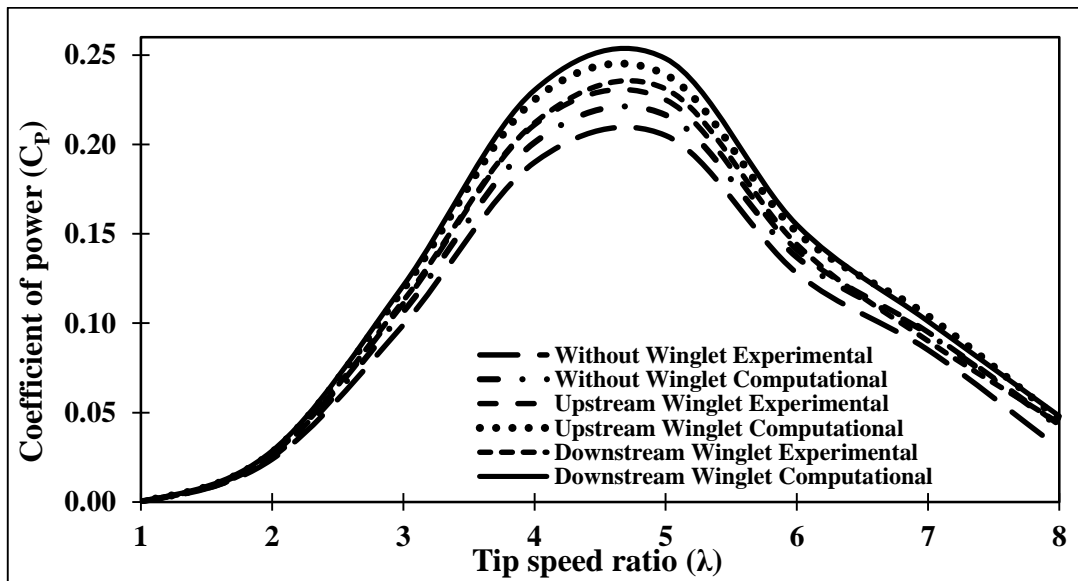
Fig. 7.25 Power coefficient at different tip-speed ratios at $\phi_P = 6°$

7.5.2 Pressure Coefficient Distribution

Fig. 7.26 illustrated the pressure coefficient distribution along the blade chord length at three different span-wise sections (i.e., r/R = 50%, 75%, and 95%). As mentioned earlier, the three cases are taken for the analysis: wind turbine blade without winglets, blade

with downstream winglets, and blade with upstream winglets. The equation use for determining the pressure co-efficient [62]

$$C_{Pr} = \frac{P - P_\infty}{\frac{1}{2}\rho(U_\infty^2 + (\omega r)^2)}$$

(7.4)

It is found that there is little change in the pressure distribution on the pressure side, for all cases, as winglets attach at the blade tip. Regarding the suction side, the pressure coefficient remained almost steady near the blade rotor hub (say, for r/R = 50%, 75%) for all the two cases. Meanwhile, close to the blade tip (r/R = 95% section), the pressure distribution on the suction side reduces due to the incorporation of winglets. Furthermore, the amount of reduction faced in downstream winglets is far more than the turbine without winglets. Overall, near the leading edge, r/R=95%, the pressure difference between suction and pressure surface is ΔC_{pr}=15 for the wind turbine with downstream winglets, and ΔC_{pr} = 6 is in the case of without winglets. So, it can be said that downstream winglets are more effective as the net pressure difference is more considerable in that case.

(a) Without winglet   (b) Downstream winglet
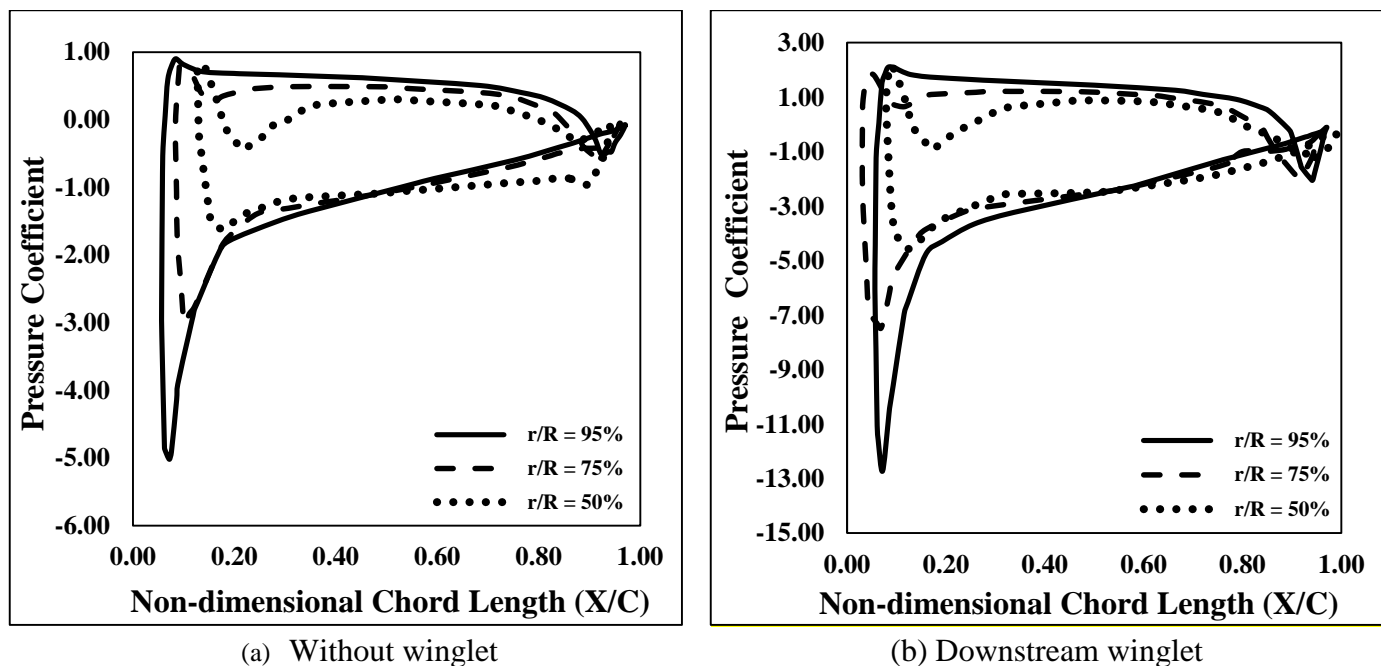
Fig. 26 Coefficient of pressure distributions on the three span-wise sections at design TSR and ϕ_P =0°

7.5.3 Pressure and velocity contours

The Fig. 27 showed the static pressure and velocity contours of the turbine model with and without winglets at TSR = 5 and = 0°. . It is evident that, by incorporating winglets at the blade tip, the maximum static pressure near the leading edge increased from (862.56 pa) for the baseline rotor to (1170.77 Pa) for the wind turbine with the downstream winglets.

(a) Pressure contours   (a) Velocity contours

(b) Pressure contours   (b) Velocity contours
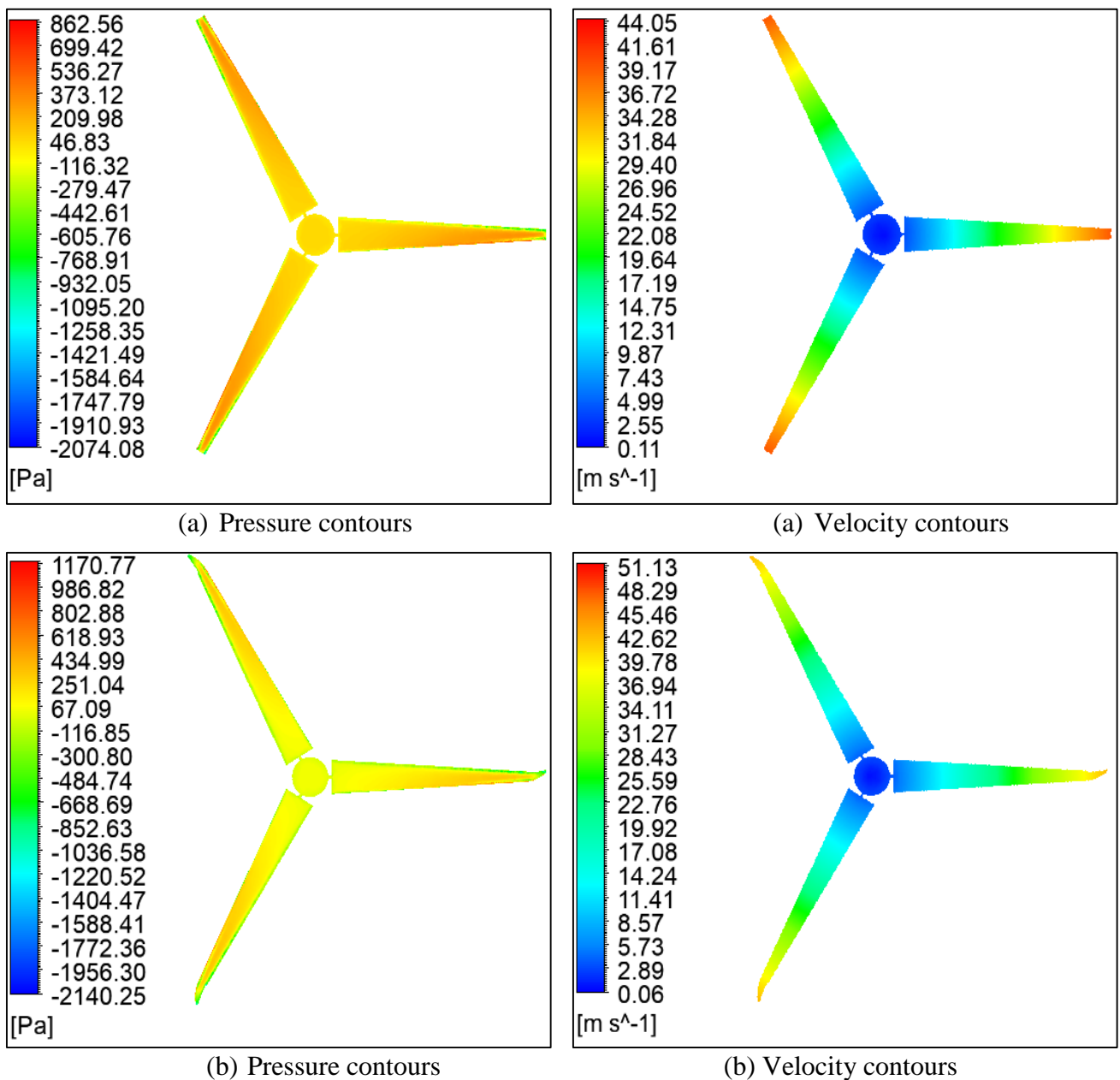
Fig. 27 Wind turbine model having a) Without winglets b) Downstream winglets

Furthermore, the pressure at the center part near the tip of the blades without winglets is less than that pressure at the exact location for the blades with downstream winglets. This phenomenon is helpful for smoother flow over the blades while winglets are incorporated. The maximum velocity increases from (44.05 m/s) for the baseline rotor to (51.13 m/s) at the blade tip for the wind turbine with the downstream winglets. This means blades with downstream winglets rotate faster than the baseline rotor.

7.5.4 Blade tip-vortices and sectional flow streamlines

As described earlier, the primary reason for the decrement of the generation of lift and power is that the vortices created at the blades' tip. For that reason, winglets are attached at the blades' tip to overcome the downwash effects of those vortices. As shown in fig. 7.28(a), vortices have created at the blade's tip, while there are no winglets. The cause for that is the higher pressure side flow moves to the lower pressure side in a circular fashion, which creates a circular flow-pattern named vortex.
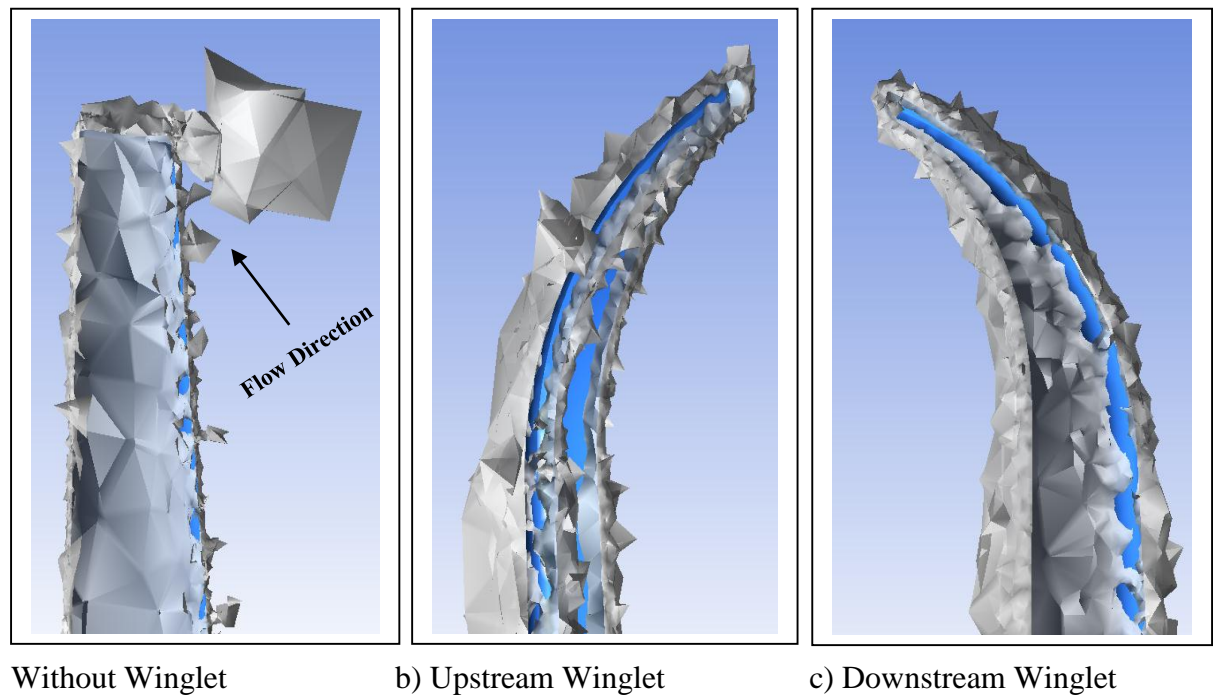
Without Winglet   b) Upstream Winglet   c) Downstream Winglet

Fig. 7.28 Comparison of vortices at the blade tip region between baseline blade Without Winglet and modified configurations at design TSR and $\phi_P = 0°$

95

Turning to the fig. 7.29(b) and 7.29(c), they represented that by adding the winglets, there is a reduction in tip vortices as the lift-induced drag decreased. Furthermore, the compensation occurred more by the downstream winglets than the upstream winglets.

Fig. 7.29 to 7.31 showed the cross-sectional flow and surface wall streamlines at design TSR and = 0º on wind turbine blades and the influences of two different position winglets on them. Considering the span-wise direction and three locations i.e., r/R= 50%, 75%, 95% are selected to analyze the flow behavior. It can be mentioned that for the first two locations, there is no significant change in flow behavior for those three configurations. Meanwhile, at r/R =95% for blades without winglets, flow particles are detached and separated due to the eddies' creation at the tip. However, for the other two configurations, flow particles are attached due to winglets' introduction.
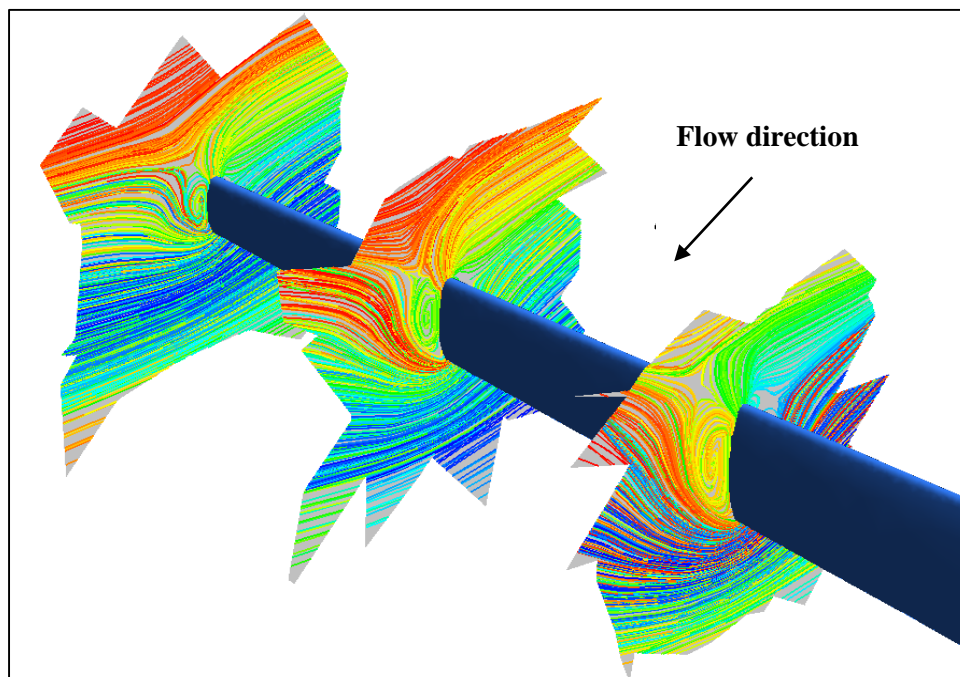
Fig. 7.29 Sectional Flow Streamlines at design TSR and $\phi_P = 0º$ (Without Winglets)
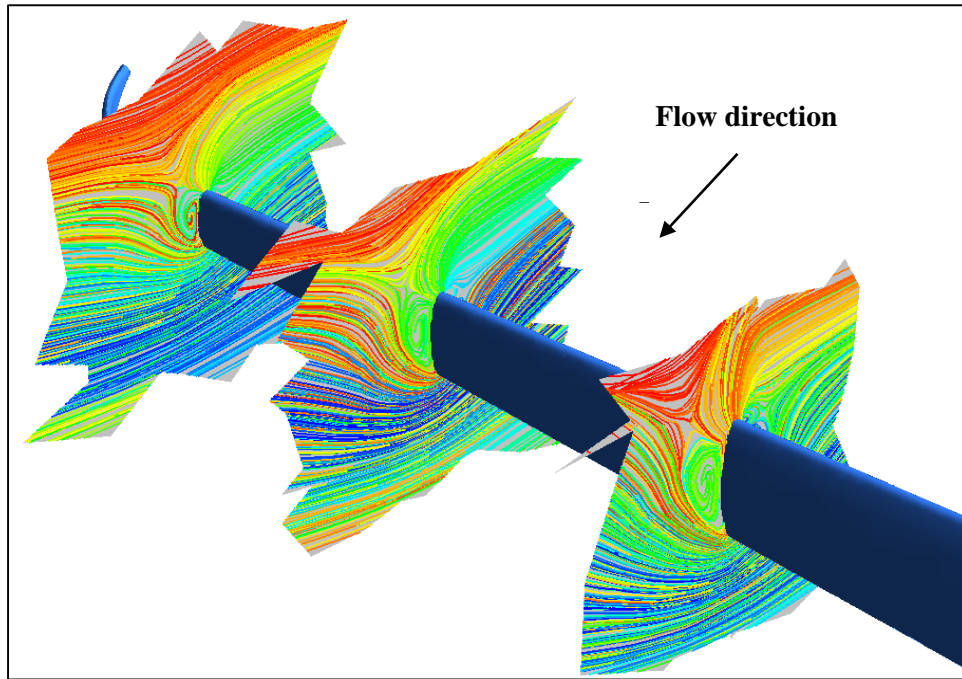
Fig. 7.30 Sectional Flow Streamlines at design TSR and $\phi_P = 0°$ (Upstream Winglets)
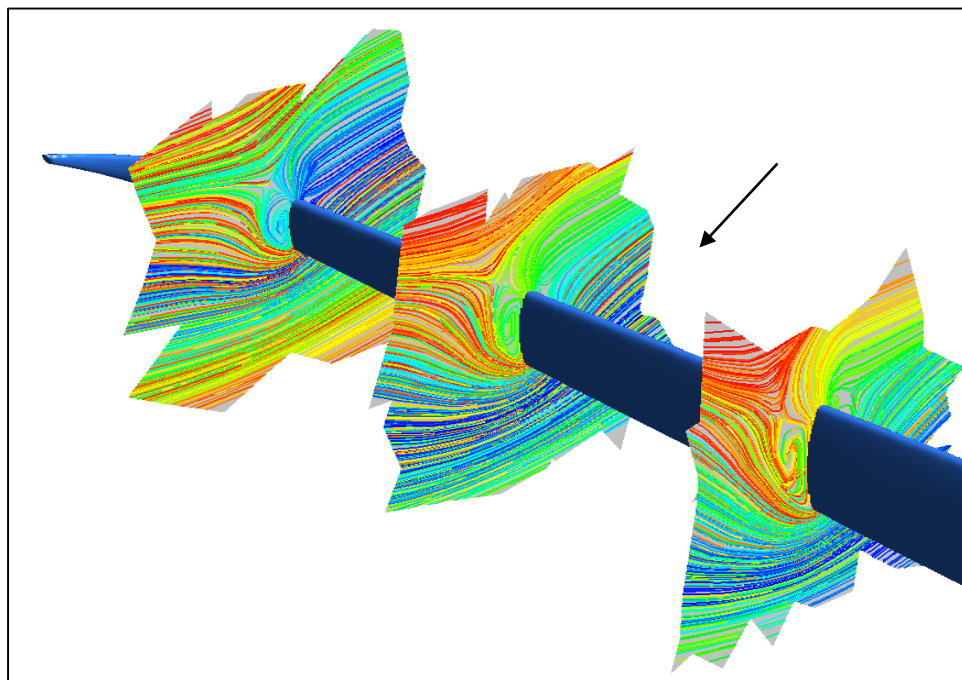
Fig. 7.31 Sectional Flow Streamlines at design TSR and $\phi_P = 0°$ (Downstream Winglets)

CHAPTER 8

CONCLUSIONS AND RECOMMENDATIONS

8.1 Concluding Remarks

This present study demonstrates a small-scale horizontal axis wind turbine with a circular arc blade section designed with a blade element momentum theory with a 0.5m rotor diameter and design wind velocity of 8 m/s. The twist angle and chord length along each section of the blade linearized to provide the blade taper and twist angle. Winglets are designed and incorporated both on the upstream and downstream side to observe the wind turbine effects. The performance characteristics of Horizontal Axis Wind Turbines having Circular Arc Blade Section, the following conclusions are drawn:

a) Both Power and Thrust coefficient are increased while adding winglets, having Circular Arc Blade Section (CABS) profiles in wind turbine blades.

b) Both Power and Thrust coefficient are enhanced concerning downstream winglets than the upstream winglets for the same winglet height and cant angle.

c) Regarding the experimental results, the maximum increment of the coefficient of power is from (0.329) for the base model to (0.355), increased by 7.91%) for upstream winglets and (0.369, increased by 12.1%) for downstream winglets at the design TSR and zero pitch angle.

d) Regarding the computational results, the maximum increment of the coefficient of power is from (0.3454) for the base model to (0.3792, increased by 9.79 %) for upstream winglets and (0.3950, increased by 14.36 %) for downstream winglets at the design TSR and zero pitch angle.

e) Blades having winglets, the maximum increment of the coefficient of thrust is from (0.9587) for the base model to (1.0636, increased by 10.94%) for upstream winglets

and (1.0408, increased by 8.6%) for downstream winglets at the design TSR and zero pitch angle.

f) The coefficient of pressure at the outer portion of the blade (r/R=95%) of the suction side drops while winglets are attached, leading to the pressure difference increment. Thus, HAWT producing considerably more torque in the span-wise direction while winglets are added at the blades' tip. Additionally, this phenomenon is more substantial regarding the downstream winglets.

Thus, It is clear that downstream winglets are much effective than the upstream winglets while added in the blade tip with CABS profile.

8.2 Recommendations for Future Work

While designing the Tip-vanes (winglets) to analyze the impact on HAWT blades having CABS, some of the points should be taken into consideration for further investigation. It is recommended that:

a) Winglets play a paramount role in the performance of wind turbines and also influences the aerodynamic characteristics. Further optimization is required of the winglets to observe the effects of the toe and twist angles.

b) Wake velocity may be evaluated at the downstream of the rotor model having CABS at different pitch angles. The effects wake on the turbine model when it installs at the rear of the first model.

c) Winglets with different designs and shapes (i.e., Fusion Split types) can be utilized to analyze further HAWT having CABS.

d) Experimental investigation may be performed with a relatively larger scale of wind turbine having winglets at the blades tip.

e) Experiments can be conducted by minimizing the manufacturing defects and the blades' surface roughness so that results are more similar to the computational results.

REFERENCES

[1] J. F. Manwell, J. G. McGowan and A. L. Rogers, *Wind Energy Explained: Theory, Design and Application*, 2nd ed. West Sussex: John Wiley & Sons, 2009.

[2] GEWC, *"Global Wind Energy Council"*, Global Wind Energy Council, 2018, P 21

[3] O. Martin, Hansen L., *Aerodynamics of Wind Turbines, 2nd ed.,* Earthscan USA, p. 181 (2008).

[4] P. Fleming and S. Probert, "The evolution of wind-turbines: An historical review", *Applied Energy*, vol. 18, no. 3, pp. 163-177, 1984. Available: 10.1016/0306-2619(84)90007-2.

[5] Pasqualetti M., Righter R. and Gipe P., *Encyclopedia of Energy*. Texas, 2004.

[6] Musgrove P., *"Wind power"*, Cambridge: Cambridge University Press, 2010.

[7] W. Rankine, *Transactions*, Institute of Naval Architects. Vol. 6, P 13, 1865.

[8] E. Golding, *The generation of electricity by wind power*. Spon: London, 1978.

[9] A. Mandal and Q. Islam, *Aerodynamics and Design of Wind Turbines*, 1st ed. Dhaka: Publication cum Information Office, DAERS, Bangladesh University of Engineering and Technology, Dhaka, Bangladesh, 2001.

[10] Wilson R. and Lissaman P., "Applied aerodynamics of wind power machines", *Ph.D. Thesis*, Oregon State University, 1974.

[11] Walker S., "Performance and optimum design analysis/ computation for propeller type wind turbines", *Ph.D. thesis*, Oregon State University, 1976.

[12] Hirch, C., Derdelinckx, R., Islam M., "A Theoretical Investigation of the Design of a Horizontal Axis Wind Turbine", *Proceedings of the European Wind Energy Conference*, Hamburg, 1984, pp. 124-129, 1984

[13] A. Mandal and M. Islam, "Application of Cascade Theory for the Aerodynamic Performance of a Horizontal Axis Wind Turbine", *Journal of the Institution of engineers*, vol. 69, no. 1, pp. 18-21, 1998.

[14] M. PandeyPandey, K. Pandey and T. Ojha, "Aerodynamic Characteristics of Cambered Steel Plates in Relation to Their Use in Wind Energy Conversion Systems", *Journal of Wind Engineering*, vol. 12, no. 2, pp. 90-104, 1988.

[15] A. Bruining and W. Timmer, "Airfoil characteristics of rotating wind turbine blades", *Journal of Wind Engineering and Industrial Aerodynamics*, vol. 39, no. 1-3, pp. 35-39, 1992. Available: 10.1016/0167-6105(92)90530-n.

[16] M. Islam, A. Islam, S. Islam and M. Razzaque, "Application of Wind Energy for Irrigation in Bangladesh", *Journal of Agricultural Mechanization in Asia, Africa and Latin America*, vol. 26, no. 2, 1995.

[17] M. Serra and M. Schoor, "Aeroelastic Tailoring of a Horizontal Axis Wind Turbine", Journal of Wind Engineering, vol. 19, no. 4, pp. 193-207, 1995

[18] A. Saifullah, M. Karim and M. Karim, "Wind Energy Potential in Bangladesh", American Journal of Engineering Research (AJER), vol. 5, no. 7, pp. 85-94, 2016.

[19] C. Leclerc, C. Masson, I. Ammara and I. Paraschivoiu, "Turbulence Modeling of the Flow Around Horizontal Axis Wind Turbines", *Journal of Wind Engineering*, vol. 23, no. 5, p. 279, 1999.

[20] A. Mesquita and A. Alves, "An Improved Approach for Performance Prediction of HAWT Using the Strip Theory*", Wind Engineering*, vol. 24, no. 6, pp. 417-430, 2000. Available: 10.1260/030952400320769802.

[21] Hosney A. B. "An Experimental Investigation and the Design Analysis of a HAWT with Circular Arc Blade Section," *Ph.D thesis*, Bangladesh University of Engineering and Technology, Dhaka, November 2002.

[22] W. Shen, R. Mikkelsen, J. Sørensen and C. Bak, "Tip loss corrections for wind turbine computations", *Wind Energy*, vol. 8, no. 4, pp. 457-475, 2005. Available: 10.1002/we.153.

[23] M. Maughmer, "Design of Winglets for High-Performance Sailplanes", *Journal of Aircraft*, vol. 40, no. 6, pp. 1099-1106, 2003. Available: 10.2514/2.7220.

[24] J. Johansen and N. Sørensen, "Aerodynamic investigation of winglets on wind turbine blades using CFD", *DTU Research Database*, 2006.

[25] J. Wang, R. Jia and K. Wu, "Numerical simulation on effect of pressure distribution of wind turbine blade with a tip vane", *Journal of Thermal Science*, vol. 16, no. 3, pp. 203-207, 2007. Available: 10.1007/s11630-007-0203-2.

[26] J. Manwell, J. McGowan and A. Rogers, *Wind energy explained.* Chichester: John Wiley & Sons, 2010.

[27] W. Shen, R. Mikkelsen, J. Sørensen and C. Bak, "Tip loss corrections for wind turbine computations", *Wind Energy*, vol. 8, no. 4, pp. 457-475, 2005. Available: 10.1002/we.153.

[28] D. Gertz, D. Johnson and N. Swytink-Binnema, "An Evaluation Testbed for Wind Turbine Blade Tip Designs — Winglet Results", *Wind Engineering*, vol. 36, no. 4, pp. 389-410, 2012. Available: 10.1260/0309-524x.36.4.389.

[29] Alsultan A., "Computational and experimental study on innovative horizontal Axis wind turbine blade designs", *MSc. Thesis.*, University of Wisconsin-Milwaukee, 2015.

[30] P. Saravanan, K. Parammasivam, S. Rajan, "Experimental Investigation on Small Horizontal Axis Wind Turbine Rotor Using Winglets", *Journal of Applied Science and Engineering*, vol. 16, no. 2, 2013. Available: https://doi.org/10.6180/jase.2013.16.2.07

[31] M. Elfarra, N. Sezer Uzol and İ. Akmandor, "Investigations on Blade Tip Tilting for Hawt Rotor Blades Using CFD", *International Journal of Green Energy*, vol. 12, no. 2, pp. 125-138, 2014. Available: 10.1080/15435075.2014.889007.

[32] M. Ariffudin, F. Mohd Zawawi, H. Mohamed Kamar and N. Kamsah, "Effectiveness of Blade Tip on Low Speed Horizontal Axis Wind Turbine Performance", *Jurnal Teknologi*, vol. 78, no. 8-4, 2016. Available: 10.11113/jt.v78.9582.

[33] Y. Ostovan and O. Uzol, "Experimental Study on the Effects of Winglets on the Performance of Two Interacting Horizontal Axis Model Wind Turbines", *Journal of Physics: Conference Series*, vol. 753, p. 022015, 2016. Available: 10.1088/1742-6596/753/2/022015.

[34] B. Zhu, X. Sun, Y. Wang and D. Huang, "Performance characteristics of a horizontal axis turbine with fusion winglet", *Energy*, vol. 120, pp. 431-440, 2017. Available: 10.1016/j.energy.2016.11.094.

[35] A. Farhan, A. Hassanpour, A. Burns and Y. Motlagh, "Numerical study of effect of winglet planform and airfoil on a horizontal axis wind turbine performance", *Renewable Energy*, vol. 131, pp. 1255-1273, 2019. Available: 10.1016/j.renene.2018.08.017.

[36] Y. Ostovan, M. Akpolat and O. Uzol, "Experimental Investigation of the Effects of Winglets on the Tip Vortex Behavior of a Model Horizontal Axis Wind Turbine Using Particle Image Velocimetry", *Journal of Solar Energy Engineering,* vol. 141, no. 1, 2018. Available: 10.1115/1.4041154.

[37] F. Zahle, N. Sørensen, M. McWilliam and A. Barlas, "Computational fluid dynamics-based surrogate optimization of a wind turbine blade tip extension for maximising energy production", *Journal of Physics: Conference Series,* vol. 1037, p. 042013, 2018. Available: 10.1088/1742-6596/1037/4/042013.

[38] H. Parra Peñuela, W. Gómez Rivera and H. Cerón, "Aerodynamic evaluation with cfd of tip devices in blade for wind turbine", *Bistua Revista De La Facultad De Ciencias Basicas*, vol. 17, no. 3, p. 70, 2019. Available: 10.24054/01204211.v3.n3.2019.3567.

[39] M. Ansari, M. Nobari and E. Amani, "Determination of pitch angles and wind speeds ranges to improve wind turbine performance when using blade tip plates", *Renewable Energy*, vol. 140, pp. 957-969, 2019. Available: 10.1016/j.renene.2019.03.119.

[40] M. Khalafallah, A. Ahmed and M. Emam, "The effect of using winglets to enhance the performance of swept blades of a horizontal axis wind turbine", *Advances in Mechanical Engineering*, vol. 11, no. 9, 2019. Available: 10.1177/1687814019878312.

[41] M. Khaled, M. Ibrahim, H. Abdel Hamed and A. AbdelGwad, "Investigation of a small Horizontal–Axis wind turbine performance with and without winglet", *Energy*, vol. 187, p. 115921, 2019. Available: 10.1016/j.energy.2019.115921.

[42] Motsamai O. and Muiruri P., "Three-dimensional effects of trailing edge flap and winglet integrated on up-scale wind turbine blade", *IOP Conference Series: Earth and Environmental Science*, vol. 354, p. 012083, 2019. Available: 10.1088/1755-1315/354/1/012083.

[43] T. Zhang et al., "Winglet design for vertical axis wind turbines based on a design of experiment and CFD approach", *Energy Conversion and Management*, vol. 195, pp. 712-726, 2019. Available: 10.1016/j.enconman.2019.05.055.

[44] M. Mourad, I. Shahin, S. Ayad, O. Abdellatif and T. Mekhail, "Effect of winglet geometry on horizontal axis wind turbine performance", *Engineering Reports*, vol. 2, no. 1, 2020. Available: 10.1002/eng2.12101.

[45] https://sreda.portal.gov.bd/site/page/0e65b027-0289-448c-aec7-2e58c83cfcc2/

[46] M. Washim Akram, M. Arman Arefin and A. Nusrat, "Prospect of green power generation as a solution to energy crisis in Bangladesh", *Energy Systems*, 2021. Available: 10.1007/s12667-020-00421-9.

[47] M. Masud, M. Nuruzzaman, R. Ahamed, A. Ananno and A. Tomal, "Renewable energy in Bangladesh: current situation and future prospect", *International Journal of Sustainable Energy*, vol. 39, no. 2, pp. 132-175, 2019. Available: 10.1080/14786451.2019.1659270.

[48] J. Leishman, "Challenges in modelling the unsteady aerodynamics of wind turbines", *Wind Energy*, vol. 5, no. 2-3, pp. 85-132, 2002. Available: 10.1002/we.62.

[49] Q. Islam, "A Theoretical Investigation of the Design of HA WT", *PhD thesis*, Vrije Universiteit Brussel, Belgium, 1986.

[50] J. Manwell, J. McGowan and A. Rogers, *Wind energy explained.* Chichester: John Wiley & Sons, 2011.

[51] E. Golding, *The generation of electricity by wind power*. Spon: London, 1978.

[52] E. Lysen, H. Bos and E. Cordes, "*Savonius Rotors for Water Pumping*", Consultancy Services Wind Energy Developing Countries, 1978.

[53] Wilson R. and Lissaman P., "Applied aerodynamics of wind power machines", *Ph.D. Thesis*, Oregon State University, 1974.

[54] R. Wilson and S. Walker, "Performance Analysis Program for Propeller Type Wind Turbines", *M.Sc. Engg. Thesis*, Oregon State University, 1981.

[55] Jonathan R. "Delaunay refinement mesh generation", *PhD thesis,* Carnegie-Mellon Univ Pittsburgh Pa School of Computer Science, 1997.

[56] A. Mandal and Q. Islam, "*Effect of Blade Shapes on the Performance of a Horizontal Axis Wind Turbine*", Mechanical Engineering Resolution Bulletin, Department of Mechanical Engineering, BUET, Vol. 10, 1987.

[57] W. Jansen, *Horizontal-axis fast running wind turbines for developing countries*. Amersfoort, Netherlands: Steering Committee for Wind energy in Developing Countries, 1976.

[58] A. Mandal and Q. Islam, *Aerodynamics and Design of Wind Turbines*, 1st ed. Dhaka: Publication cum Information Office, DAERS, Bangladesh University of Engineering and Technology, Dhaka, Bangladesh, 2001.

[59] Queirolo C. and Andrés M., "Impact of Morphing Winglets on Aircraft Performance", *M.Sc. Engg. Thesis*, Delft University of Technology, 2018.

[60] NTRS - NASA Technical Reports Server, "*A design approach and selected wind tunnel results at high subsonic speeds for wing-tip mounted winglets*", 1976.

[61] A. Wheeler, *Introduction to Engineering Experimentation*, 2nd ed. 2004, p. 200.

[62] A. Farhan, A. Hassanpour, A. Burns and Y. Motlagh, "Numerical study of effect of winglet planform and airfoil on a horizontal axis wind turbine performance", *Renewable Energy*, vol. 131, pp. 1255-1273, 2019. Available: 10.1016/j.renene.2018.08.017.

APENDICES

Appendix A

The level of uncertainty can be obtained using the following equation

$$\delta R = \sqrt{(\delta x_1 \frac{\partial R}{\partial x_1})^2 + (\delta x_2 \frac{\partial R}{\partial x_2})^2 + \ldots\ldots + (x_n \frac{\partial R}{\partial x_n})^2} \qquad \text{A.1}$$

Coefficient of power equation in simplified form:

$$C_P = \frac{(F_1 - F_2)R \frac{2\pi r}{60}}{\frac{1}{2}\rho \pi r^2 V_\infty^3}$$

A.2

Thus, the uncertainty of the Power Coefficient depends on $\delta_{Cp} = f(F_1, F_2, R, N, \rho, r, V_\infty)$

Considering, design TSR for checking the uncertainty and the possibilities of deviation of each parameter given below:

$$\delta F_1 = \pm 0.4N, \delta F_2 = \pm 0.01N, \delta R = \pm 0.001m, \delta N = \pm 13 RPM, \delta \rho = \pm 0.02 \frac{kg}{m^3}, \delta r = \pm 0.01m,$$

$$\delta V_\infty = \pm 0.5 m/s$$

The uncertainty equation becomes:

$$\delta_{Cp} = \sqrt{(\delta F_1 \frac{\partial C_P}{\partial F_1})^2 + (\delta F_2 \frac{\partial C_P}{\partial F_2})^2 + (\delta R \frac{\partial C_P}{\partial R})^2 + (\delta N \frac{\partial C_P}{\partial N})^2 + (\delta \rho \frac{\partial C_P}{\partial \rho})^2 + (\delta r \frac{\partial C_P}{\partial r})^2 + (\delta V_\infty \frac{\partial C_P}{\partial V_\infty})^2} \quad \text{A.3}$$

$$\delta_{Cp} = \pm 0.0129$$

Experimental Uncertainty at design TSR= 0.329 ± 0.0129   A.4

$$\text{Percentage of error} = \frac{0.0129}{0.329} * 100\% \qquad \text{A.5}$$

$$= 3.92\%$$
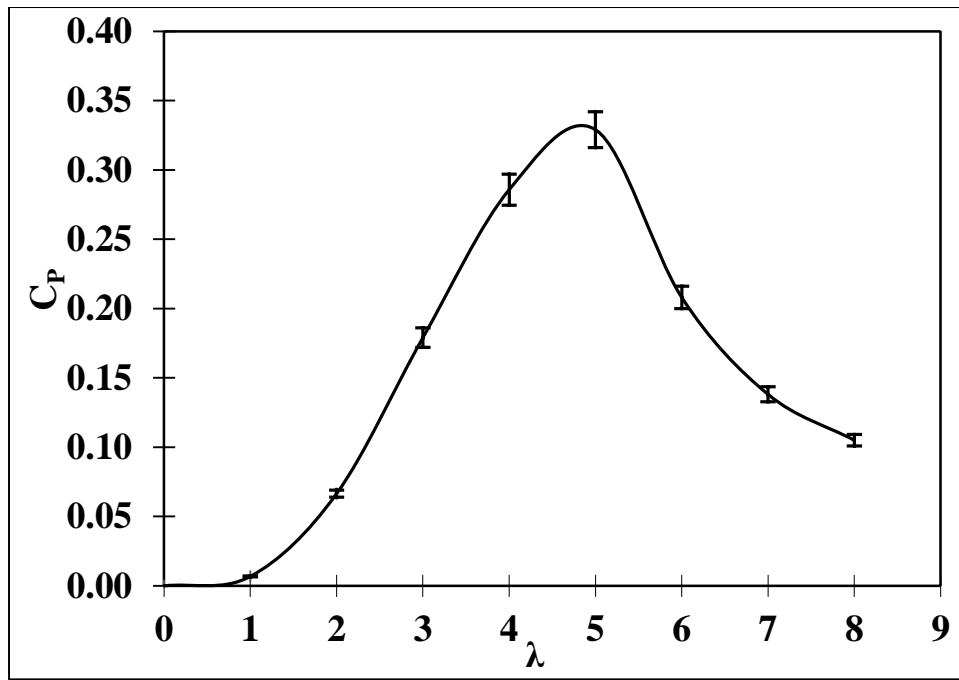
Fig. 8.1 Power Coefficient at different tip-speed ratios at design TSR with uncertainties

Appendix B

Table 7.1 Experimental C_p values of wind turbine model at $\phi_P = 0°$

Tip-Speed Ratio, λ	Pressure Coefficient, C_P		
	Without Winglet	**Upstream Winglet**	**Downstream Winglet**
0	0.0000	0.0000	0.0000
1	0.0068	0.0072	0.0075
2	0.0665	0.0710	0.0732
3	0.1790	0.1930	0.1980
4	0.2857	0.3110	0.3200
5	0.3290	0.3550	0.3690
6	0.2080	0.2250	0.2300
7	0.1381	0.1470	0.1520
8	0.1050	0.1110	0.1180
Average	**0.1465**	**0.1578**	**0.1631**

Table 7.2 Average values and percentage of increase of C_P at $\phi_P = 0°$

Case	Average C_P	Increase (%)
Without Winglet	0.1465	**0.00**
Upstream Winglet	0.1578	**7.7**
Downstream Winglet	0.1631	**11.33**

Table 7.3 Experimental C_p values of wind turbine model at $\phi_p = 2°$

Tip-Speed Ratio, λ	Pressure Coefficient, C_P		
	Without Winglet	**Upstream Winglet**	**Downstream Winglet**
0	0.0000	0.0000	0.0000
1	0.0026	0.0029	0.0030
2	0.0478	0.0526	0.0550
3	0.1514	0.1640	0.1710
4	0.2627	0.2850	0.2950
5	0.2950	0.3190	0.3290
6	0.1652	0.1810	0.1820
7	0.1040	0.1130	0.1150
8	0.0610	0.0660	0.0680
Average	**0.1211**	**0.1315**	**0.1353**

Table 7.4 Average values and percentage of increase of C_P at $\phi_P = 2^\circ$

Case	Average C_P	Increase (%)
Without Winglet	0.1211	**0.00**
Upstream Winglet	0.1315	**8.58**
Downstream Winglet	0.1353	**11.73**

Table. 7.5 Experimental C_p values of wind turbine model at $\phi_P = 4^\circ$

Tip-Speed Ratio, λ	Pressure Coefficient, C_P		
	Without Winglet	**Upstream Winglet**	**Downstream Winglet**
0	0.0000	0.0000	0.0000
1	0.0003	0.0003	0.0003
2	0.0361	0.0389	0.0403
3	0.1251	0.1350	0.1400
4	0.2191	0.2380	0.2440
5	0.2453	0.2650	0.2750
6	0.1403	0.1510	0.1530
7	0.0850	0.1010	0.1000
8	0.0350	0.0450	0.0460
Average	**0.0985**	**0.1082**	**0.1110**

Table 7.6 Average values and percentage of increase of C_P at $\phi_P = 4^\circ$

Case	Average C_P	**Increase (%)**
Without Winglet	0.0985	**0.00**
Upstream Winglet	0.1082	**9.85**
Downstream Winglet	0.1110	**12.70**

Table 7.7 Experimental C_p values of wind turbine model at $\phi_P = 6^\circ$

Tip-Speed Ratio, λ	Pressure Coefficient, C_P		
	Without Winglet	**Upstream Winglet**	**Downstream Winglet**
0	0.0000	0.0000	0.0000
1	0.0003	0.0003	0.0003
2	0.0239	0.0259	0.0265
3	0.0990	0.1110	0.1125
4	0.1900	0.2110	0.2120
5	0.2050	0.2250	0.2310
6	0.1280	0.1410	0.1440
7	0.0850	0.0950	0.0900
8	0.0300	0.0430	0.0440
Average	**0.0846**	**0.0947**	**0.0956**

Table 7.8 Average values and percentage of increase of C_P at $\phi_P = 6°$

Case	Average C_P	**Increase** (%)
Without Winglet	0.0846	**0.00**
Upstream Winglet	0.0947	**11.94**
Downstream Winglet	0.0956	**13.01**

Table 7.9 Experimental C_Q values of wind turbine model (without winglets)

Tip-Speed Ratio, λ	**Torque Coefficient, C_Q**			
	$\phi_P = 0°$	$\phi_P = 2°$	$\phi_P = 4°$	$\phi_P = 6°$
0	0.0000	0.0000	0.0000	0.0000
1	0.0068	0.0026	0.0003	0.0003
2	0.0333	0.0239	0.0181	0.0120
3	0.0597	0.0505	0.0417	0.0330
4	0.0714	0.0657	0.0548	0.0475
5	0.0658	0.0590	0.0491	0.0410
6	0.0347	0.0275	0.0234	0.0213
7	0.0197	0.0149	0.0121	0.0121
8	0.0131	0.0076	0.0044	0.0038
Average	**0.0338**	**0.0280**	**0.0226**	**0.0190**

Table 7.10 Average values and percentage of decrease of C_Q (without winglets)

Case	Average C_Q	**Decrease (%)**
$\phi_P = 0°$	0.0338	**0.00**
$\phi_P = 2°$	0.0280	**17.16**
$\phi_P = 4°$	0.0226	**33.14**
$\phi_P = 6°$	0.0190	**43.79**

Table 7.11 Experimental C_Q values of wind turbine model (Upstream winglets)

Tip-Speed Ratio, λ	**Torque Coefficient, C_Q**			
	$\phi_P = 0°$	$\phi_P = 2°$	$\phi_P = 4°$	$\phi_P = 6°$
0	0.0000	0.0000	0.0000	0.0000
1	0.0071	0.0029	0.0003	0.0003
2	0.0355	0.0263	0.0195	0.0130
3	0.0643	0.0547	0.0450	0.0370
4	0.0778	0.0713	0.0595	0.0528

5	0.0710	0.0638	0.0530	0.0450
6	0.0375	0.0302	0.0252	0.0235
7	0.0210	0.0161	0.0144	0.0136
8	0.0139	0.0083	0.0056	0.0054
Average	**0.0365**	**0.0304**	**0.0247**	**0.0212**

Table 7.12 Average values and percentage of decrease of C_Q (Upstream winglets)

Case	Average C_Q	**Decrease (%)**
$\phi_P = 0°$	0.0365	**0.00**
$\phi_P = 2°$	0.0304	**16.72**
$\phi_P = 4°$	0.0247	**32.33**
$\phi_P = 6°$	0.0212	**41.92**

Table 7.13 Experimental C_Q values of wind turbine model (Downstream winglets)

	Torque Coefficient, C_Q			
Tip-Speed Ratio, λ	$\phi_P = 0°$	$\phi_P = 2°$	$\phi_P = 4°$	$\phi_P = 6°$
0	0.0000	0.0000	0.0000	0.0000
1	0.0075	0.0030	0.0003	0.0003
2	0.0366	0.0275	0.0202	0.0133
3	0.0660	0.0570	0.0467	0.0375
4	0.0800	0.0738	0.0610	0.0530
5	0.0738	0.0658	0.0550	0.0462
6	0.0383	0.0303	0.0255	0.0240
7	0.0217	0.0164	0.0143	0.0129
8	0.0148	0.0085	0.0058	0.0055
Average	**0.0376**	**0.0314**	**0.0254**	**0.0214**

Table 7.14 Average values and percentage of decrease of C_Q (Downstream winglets)

Case	Average C_Q	**Decrease (%)**
$\phi_P = 0°$	0.0376	**0.00**
$\phi_P = 2°$	0.0314	**16.49**
$\phi_P = 4°$	0.0254	**32.45**
$\phi_P = 6°$	0.0214	**43.06**

Table 7.15 Experimental C_Q values of wind turbine model at $\phi_P = 0°$

Tip-Speed Ratio, λ	Torque Coefficient, C_Q		
	Without Winglet	Upstream Winglet	Downstream Winglet
0	0.0000	0.0000	0.0000
1	0.0068	0.0071	0.0075
2	0.0333	0.0355	0.0366
3	0.0597	0.0643	0.0660
4	0.0714	0.0778	0.0800
5	0.0658	0.0710	0.0738
6	0.0347	0.0375	0.0383
7	0.0197	0.0210	0.0217
8	0.0131	0.0139	0.0148
Average	**0.0338**	**0.0365**	**0.0376**

Table 7.16 Average values and percentage of increase of C_Q at $\phi_P = 0°$

Case	Average C_Q	Increase (%)
Without Winglet	0.0338	**0.00**
Upstream Winglet	0.0365	**7.99**
Downstream Winglet	0.0376	**11.24**

Table 7.17 Experimental C_Q values of wind turbine model at $\phi_P = 2°$

Tip-Speed Ratio, λ	Torque Coefficient, C_Q		
	Without Winglet	Upstream Winglet	Downstream Winglet
0	0.0000	0.0000	0.0000
1	0.0026	0.0029	0.0030
2	0.0239	0.0263	0.0275
3	0.0505	0.0547	0.0570
4	0.0657	0.0713	0.0738
5	0.0590	0.0638	0.0658
6	0.0275	0.0302	0.0303
7	0.0149	0.0161	0.0164
8	0.0076	0.0083	0.0085
Average	**0.0280**	**0.0304**	**0.0314**

Table 7.18 Average values and percentage of increase of C_Q at $\phi_P = 2°$

Case	Average C_Q	Increase (%)
Without Winglet	0.0280	**0.00**
Upstream Winglet	0.0304	**8.57**
Downstream Winglet	0.0314	**12.14**

Table 7.19 Experimental C_Q values of wind turbine model at $\phi_P = 4°$

Tip-Speed Ratio, λ	Torque Coefficient, C_Q		
	Without Winglet	**Upstream Winglet**	**Downstream Winglet**
0	0.0000	0.0000	0.0000
1	0.0003	0.0003	0.0003
2	0.0181	0.0195	0.0202
3	0.0417	0.0450	0.0467
4	0.0548	0.0595	0.0610
5	0.0491	0.0530	0.0550
6	0.0234	0.0252	0.0255
7	0.0121	0.0144	0.0143
8	0.0044	0.0056	0.0058
Average	**0.0226**	**0.0247**	**0.0254**

Table 7.20 Average values and percentage of increase of C_Q at $\phi_P = 4°$

Case	Average C_Q	Increase (%)
Without Winglet	.0226	**0.00**
Upstream Winglet	.0247	**9.29**
Downstream Winglet	.0254	**12.39**

Table 7.21 Experimental C_Q values of wind turbine model at $\phi_P = 6°$

Tip-Speed Ratio, λ	Torque Coefficient, C_Q		
	Without Winglet	**Upstream Winglet**	**Downstream Winglet**
0	0.0000	0.0000	0.0000
1	0.0003	0.0003	0.0003
2	0.0120	0.0130	0.0133
3	0.0330	0.0370	0.0375
4	0.0475	0.0528	0.0530
5	0.0410	0.0450	0.0462
6	0.0213	0.0235	0.0240
7	0.0121	0.0136	0.0129
8	0.0038	0.0054	0.0055
Average	**0.0190**	**0.0212**	**0.0214**

Table 7.22 Average values and percentage of increase of C_Q at $\phi_P = 6°$

Case	Average C_Q	Increase (%)
Without Winglet	0.0190	**0.00**
Upstream Winglet	0.0212	**11.58**
Downstream Winglet	0.0214	**12.63**

Table 7.23 Experimental C_T values of wind turbine model (Without winglets)

Tip-Speed Ratio, λ	Thrust Coefficient, C_T			
	$\phi_P = 0°$	$\phi_P = 2°$	$\phi_P = 4°$	$\phi_P = 6°$
0	0.0000	0.0000	0.0000	0.0000
1	0.1333	0.1349	0.1350	0.1388
2	0.2383	0.2386	0.2413	0.2473
3	0.4278	0.4280	0.4298	0.4272
4	0.6833	0.6709	0.6677	0.6429
5	0.9587	0.9291	0.9127	0.8595
6	1.2091	1.1503	1.1032	1.0139
7	1.3926	1.3147	1.2551	1.1215
8	1.5236	1.4977	1.3179	1.2329
Average	**0.7296**	**0.7071**	**0.6736**	**0.6316**

Table 7.24 Average values and percentage of decrease of C_T (Without winglets)

Case	Average C_T	Decrease (%)
$\phi_P = 0°$	0.7296	**0.00**
$\phi_P = 2°$	0.7071	**3.09**
$\phi_P = 4°$	0.6736	**7.68**
$\phi_P = 6°$	0.6316	**13.43**

Table 7.25 Experimental C_T values of wind turbine model (Upstream winglets)

Tip-Speed Ratio, λ	Thrust Coefficient, C_T			
	$\phi_P = 0°$	$\phi_P = 2°$	$\phi_P = 4°$	$\phi_P = 6°$
0	0.0000	0.0000	0.0000	0.0000
1	0.1384	0.1390	0.1410	0.1406
2	0.2569	0.2547	0.2606	0.2611
3	0.4660	0.4661	0.4638	0.4574
4	0.7465	0.7324	0.7152	0.6951
5	1.0636	1.0196	0.9775	0.9371
6	1.3199	1.2614	1.1827	1.1119
7	1.5163	1.4173	1.3099	1.2429
8	1.6401	1.5463	1.4455	1.2927
Average	**0.7942**	**0.7596**	**0.7218**	**0.6821**

Table 7.26 Average values and percentage of decrease of C_T (Upstream winglets)

Case	Average C_T	Decrease (%)
$\phi_P = 0°$	0.7942	**0.00**
$\phi_P = 2°$	0.7596	**4.36**
$\phi_P = 4°$	0.7218	**9.11**
$\phi_P = 6°$	0.6521	**17.89**

Table 7.27 Experimental C_T values of wind turbine model (Downstream winglets)

Tip-Speed Ratio, λ	Thrust Coefficient, C_T			
	$\phi_P = 0°$	$\phi_P = 2°$	$\phi_P = 4°$	$\phi_P = 6°$
0	0.0000	0.0000	0.0000	0.0000
1	0.1399	0.1391	0.1399	0.1385
2	0.2507	0.2551	0.2551	0.2546
3	0.4579	0.4545	0.4559	0.4542
4	0.7304	0.7211	0.7055	0.6911
5	1.0408	1.0081	0.9664	0.9228
6	1.3142	1.2500	1.1750	1.1031
7	1.5004	1.3800	1.3165	1.2155
8	1.8531	1.5943	1.5004	1.3008
Average	**0.8097**	**0.7558**	**0.7238**	**0.6756**

Table 7.28 Average values and percentage of decrease of C_T (Downstream winglets)

Case	Average C_T	Decrease (%)
$\phi_P = 0°$	0.8097	**0.00**
$\phi_P = 2°$	0.7558	**6.66**
$\phi_P = 4°$	0.7238	**10.61**
$\phi_P = 6°$	0.6756	**16.56**

Table 7.29 Experimental C_T values of wind turbine model at $\phi_P = 0°$

Tip-Speed Ratio, λ	Thrust Coefficient, C_T		
	Without Winglet	Upstream Winglet	Downstream Winglet
0	0.0000	0.0000	0.0000
1	0.1333	0.1384	0.1399
2	0.2383	0.2569	0.2507
3	0.4278	0.4660	0.4579
4	0.6833	0.7465	0.7304
5	0.9587	1.0636	1.0408
6	1.2091	1.3199	1.3142
7	1.3926	1.5163	1.5004
8	1.5236	1.6401	1.8531
Average	**0.7296**	**0.7942**	**0.8097**

Table 7.30 Average values and percentage of increase of C_T at $\phi_P = 0°$

Case	Average C_T	Increase (%)
Without Winglet	0.7296	**0.00**
Upstream Winglet	0.7942	**8.85**
Downstream Winglet	0.8097	**10.98**

Table 7.31 Experimental C_T values of wind turbine model at $\phi_P = 2°$

Tip-Speed Ratio, λ	Thrust Coefficient, C_T		
	Without Winglet	Upstream Winglet	Downstream Winglet
0	0.0000	0.0000	0.0000
1	0.1349	0.1390	0.1391
2	0.2386	0.2547	0.2551
3	0.4280	0.4661	0.4545
4	0.6709	0.7324	0.7211
5	0.9291	1.0196	1.0081
6	1.1503	1.2614	1.2500
7	1.3147	1.4173	1.3800
8	1.4977	1.5463	1.5943
Average	**0.7071**	**0.7558**	**0.7596**

Table 7.32 Average values and percentage of increase of C_T at $\phi_P = 2°$

Case	Average C_T	Increase (%)
Without Winglet	0.7071	**0.00**
Upstream Winglet	0.7558	**6.89**
Downstream Winglet	0.7596	**7.43**

Table 7.33 Experimental C$_T$ values of wind turbine model at $\phi_P = 4°$

Tip-Speed Ratio, λ	Thrust Coefficient, C$_T$		
	Without Winglet	Upstream Winglet	Downstream Winglet
0	0.0000	0.0000	0.0000
1	0.1350	0.1410	0.1399
2	0.2413	0.2606	0.2551
3	0.4298	0.4638	0.4559
4	0.6677	0.7152	0.7055
5	0.9127	0.9775	0.9664
6	1.1032	1.1827	1.1750
7	1.2551	1.3099	1.3165
8	1.3179	1.4455	1.5004
Average	**0.6736**	**0.7218**	**0.7238**

Table 7.34 Average values and percentage of increase of C$_T$ at $\phi_P = 4°$

Case	Average C$_T$	Increase (%)
Without Winglet	0.6736	**0.00**
Upstream Winglet	0.7218	**7.16**
Downstream Winglet	0.7238	**7.45**

Table 7.35 Experimental C$_T$ values of wind turbine model at $\phi_P = 6°$

Tip-Speed Ratio, λ	Thrust Coefficient, C$_T$		
	Without Winglet	Upstream Winglet	Downstream Winglet
0	0.0000	0.0000	0.0000
1	0.1388	0.1406	0.1385
2	0.2473	0.2611	0.2546
3	0.4272	0.4574	0.4542
4	0.6429	0.6951	0.6911
5	0.8595	0.9371	0.9228
6	1.0139	1.1119	1.1031
7	1.1215	1.2429	1.2155
8	1.2329	1.2927	1.3008
Average	**0.6316**	**0.6756**	**0.6821**

Table 7.36 Average values and percentage of increase of C$_T$ at $\phi_P = 6°$

Case	Average C$_T$	Increase (%)
Without Winglet	0.6316	**0.00**
Upstream Winglet	0.6821	**6.97**
Downstream Winglet	0.6756	**8.00**

Table 7.37 Experimental and computational C_P values of wind turbine model at $\phi_P = 0°$

Tip-Speed Ratio, λ	Pressure Coefficient, (C_P)					
	Without Winglet Experimental	Without Winglet Computational	Upstream Winglet Experimental	Upstream Winglet Computational	Downstream Winglet Experimental	Downstream Winglet Computational
0	0.0000	0.0000	0.0000	0.0000	0.0000	0.0000
1	0.0068	0.0074	0.0072	0.0077	0.0075	0.0080
2	0.0665	0.0694	0.0710	0.0760	0.0732	0.0789
3	0.1790	0.1860	0.1930	0.2064	0.1980	0.2130
4	0.2857	0.3001	0.3110	0.3302	0.3200	0.3430
5	0.3290	0.3454	0.3550	0.3792	0.3690	0.3950
6	0.2080	0.2184	0.2250	0.2410	0.2300	0.2491
7	0.1381	0.1450	0.1470	0.1600	0.1520	0.1640
8	0.1050	0.1100	0.1110	0.1220	0.1180	0.1250
Avg.	0.1465	0.1535	0.1578	0.1692	0.1631	0.1751

Table 7.38 Percentage of increase of C_P (Experimental) at $\phi_P = 0°$

		Tip-Speed Ratio, λ		
		4	5	6
Pressure Coefficient, C_P	Without Winglet Experimental	0.2857	0.3290	0.2080
	Upstream Winglet Experimental	0.3110	0.3550	0.2250
	Downstream Winglet Experimental	0.3200	0.3690	0.2300
	% increase for Upstream Winglet	8.85	7.91	8.18
	% increase for Downstream Winglet	12.01	12.1	10.58

Table 7.39 Percentage of increase of C_P (Computational) at $\phi_P = 0°$

		Tip-Speed Ratio, λ		
		4	5	6
Pressure Coefficient, C_P	Without Winglet Computational	0.3001	0.3454	0.2184
	Upstream Winglet Computational	0.3302	0.3792	0.2410
	Downstream Winglet Computational	0.3430	0.3950	0.2491
	% increase for Upstream Winglet	10.03	9.79	10.35
	% increase for Downstream Winglet	14.30	14.36	14.06

Table 7.40 Experimental and computational C_p values of wind turbine model at $\phi_P = 2°$

| Tip-Speed Ratio, λ | Pressure Coefficient, (C_P) | | | | | |
	Without Winglet Experimental	Without Winglet Computational	Upstream Winglet Experimental	Upstream Winglet Computational	Downstream Winglet Experimental	Downstream Winglet Computational
0	0.0000	0.0000	0.0000	0.0000	0.0000	0.0000
1	0.0026	0.0027	0.0029	0.0031	0.0030	0.0032
2	0.0478	0.0509	0.0526	0.0564	0.0550	0.0585
3	0.1514	0.1589	0.1640	0.1750	0.1710	0.1821
4	0.2627	0.2752	0.2850	0.3041	0.2950	0.3150
5	0.2950	0.3093	0.3190	0.3412	0.3290	0.3530
6	0.1652	0.1735	0.1810	0.1930	0.1820	0.1990
7	0.1040	0.1100	0.1130	0.1210	0.1150	0.1250
8	0.0610	0.0640	0.0660	0.0710	0.0680	0.0730
Avg.	**0.1211**	**0.1272**	**0.1315**	**0.1405**	**0.1353**	**0.1454**

Table 7.41 Percentage of increase of C_P (Experimental) at $\phi_P = 2°$

| | | Tip-Speed Ratio, λ | | |
		4	5	6
Pressure Coefficient, C_P	Without Winglet Experimental	0.2627	0.2950	0.1652
	Upstream Winglet Experimental	0.2850	0.3190	0.1810
	Downstream Winglet Experimental	0.2950	0.3290	0.1820
	% increase for Upstream Winglet	**8.49**	**8.14**	**9.56**
	% increase for Downstream Winglet	**12.30**	**11.53**	**10.17**

Table 7.42 Percentage of increase of C_P (Computational) at $\phi_P = 2°$

| | | Tip-Speed Ratio, λ | | |
		4	5	6
Pressure Coefficient, C_P	Without Winglet Computational	0.2752	0.3093	0.1735
	Upstream Winglet Computational	0.3041	0.3412	0.1930
	Downstream Winglet Computational	0.3150	0.3530	0.1990
	% increase for Upstream Winglet	**10.51**	**10.31**	**11.24**
	% increase for Downstream Winglet	**14.46**	**14.13**	**14.70**

Table 7.43 Experimental and computational C_P values of wind turbine model at $\phi_P = 4°$

Tip-Speed Ratio, λ	Pressure Coefficient, (C_P)					
	Without Winglet Experimental	Without Winglet Computational	Upstream Winglet Experimental	Upstream Winglet Computational	Downstream Winglet Experimental	Downstream Winglet Computational
0	0.0000	0.0000	0.0000	0.0000	0.0000	0.0000
1	0.0003	0.0003	0.0003	0.0003	0.0003	0.0003
2	0.0361	0.0379	0.0389	0.0417	0.0403	0.0432
3	0.1251	0.1313	0.1350	0.1450	0.1400	0.1500
4	0.2191	0.2300	0.2380	0.2540	0.2440	0.2630
5	0.2453	0.2575	0.2650	0.2840	0.2750	0.2950
6	0.1403	0.1473	0.1510	0.1630	0.1530	0.1654
7	0.0850	0.0987	0.1010	0.1090	0.1000	0.1114
8	0.0350	0.0430	0.0450	0.0480	0.0460	0.0490
Avg.	**0.0985**	**0.1051**	**0.1082**	**0.1161**	**0.1110**	**0.1197**

Table 7.44 Percentage of increase of C_P (Experimental) at $\phi_P = 4°$

		Tip-Speed Ratio, λ		
		4	5	6
Pressure Coefficient, C_P	Without Winglet Experimental	0.2191	0.2453	0.1403
	Upstream Winglet Experimental	0.2380	0.2650	0.1510
	Downstream Winglet Experimental	0.2440	0.2750	0.1530
	% increase for Upstream Winglet	**8.63**	**8.03**	**7.63**
	% increase for Downstream Winglet	**11.37**	**12.11**	**9.05**

Pressure Table 7.45 Percentage of increase of C_P (Computational) at $\phi_P = 4°$

		Tip-Speed Ratio, λ		
		4	5	6
Pressure Coefficient, C_P	Without Winglet Computational	0.2300	0.2575	0.1473
	Upstream Winglet Computational	0.2540	0.2840	0.1630
	Downstream Winglet Computational	0.2630	0.2950	0.1654
	% increase for Upstream Winglet	**10.43**	**10.29**	**10.66**
	% increase for Downstream Winglet	**14.35**	**14.56**	**12.29**

Table 7.46 Experimental and computational C_p values of turbine model at $\phi_P = 6°$

Tip-Speed Ratio, λ	Without Winglet Experimental	Without Winglet Computational	Upstream Winglet Experimental	Upstream Winglet Computational	Downstream Winglet Experimental	Downstream Winglet Computational
0	0.0000	0.0000	0.0000	0.0000	0.0000	0.0000
1	0.0003	0.0003	0.0003	0.0003	0.0003	0.0003
2	0.0239	0.0251	0.0259	0.0277	0.0265	0.0285
3	0.0990	0.1064	0.1110	0.1190	0.1125	0.1210
4	0.1900	0.2011	0.2110	0.2250	0.2120	0.2304
5	0.2050	0.2165	0.2250	0.2390	0.2310	0.2480
6	0.1280	0.1369	0.1410	0.1510	0.1440	0.1550
7	0.0850	0.0940	0.0950	0.1040	0.0900	0.1010
8	0.0300	0.0419	0.0430	0.0461	0.0440	0.0480
Avg.	**0.0846**	**0.0914**	**0.0947**	**0.1013**	**0.0956**	**0.1036**

Table 7.47 Percentage of increase of C_P (Experimental) at $\phi_P = 6°$

		Tip-Speed Ratio, λ		
		4	**5**	**6**
Pressure Coefficient, C_P	**Without Winglet Experimental**	0.1900	0.2050	0.1280
	Upstream Winglet Experimental	0.2110	0.2250	0.1410
	Downstream Winglet Experimental	0.2120	0.2310	0.1440
	% increase for Upstream Winglet	**11.05**	**9.76**	**10.16**
	% increase for Downstream Winglet	**11.58**	**12.68**	**12.5**

Table 7.48 Percentage of increase of C_P (Computational) at $\phi_P = 6°$

		Tip-Speed Ratio, λ		
		4	**5**	**6**
Pressure Coefficient, C_P	**Without Winglet Computational**	0.2011	0.2165	0.1369
	Upstream Winglet Computational	0.2250	0.2390	0.1510
	Downstream Winglet Computational	0.2304	0.2480	0.1550
	% increase for Upstream Winglet	**11.88**	**10.39**	**10.30**
	% increase for Downstream Winglet	**14.57**	**14.55**	**13.22**